

Novel Experimental-Modeling Coupled Framework to Accelerate Therapeutic Development for Volumetric Muscle Loss Injuries

A Dissertation

Presented to

the faculty of the School of Engineering and Applied Science

University of Virginia

in partial fulfillment

of the requirements for the degree

Doctor of Philosophy

by

Amanda Meppelink Westman

May 2020

APPROVAL SHEET

This Dissertation
is submitted in partial fulfillment of the requirements
for the degree of
Doctor of Philosophy

Author Signature: *Amanda Westman*

This Dissertation has been read and approved by the examining committee:

Advisor: Silvia S. Blemker

Committee Member: Shayn S. Peirce

Committee Member: George J. Christ

Committee Member: Donald R. Griffin

Committee Member: Jason R. Kerrigan

Committee Member: _____

Accepted for the School of Engineering and Applied Science:



Craig H. Benson, School of Engineering and Applied Science

May 2020

**Novel experimental-modeling coupled framework to
accelerate therapeutic development for volumetric muscle loss
injuries**

By Amanda Meppelink Westman

Acknowledgements

Four years ago, I was an intense, driven, highly motivated, fast paced New Englander but I knew it was time to return to school to pursue my PhD and, personally, it was time for a change of pace. In my interview with Silvia, I expressed my desire to combine the fields of tissue engineering and computational modeling to improve the efficiency of *in vivo* studies. UVA was the perfect place to pursue this research and Charlottesville was the right place for me to live in this next chapter of life. I never would have imagined the impactful and life-changing journey graduate school would be. I am still an intense, driven researcher but my time at UVA has helped me grow as a scientist and as a person and Charlottesville has made me slow down and enjoy life. I am so thankful for this journey and I would not have been successful without a tremendous amount of support from mentors, colleagues, friends, and family.

First, I must acknowledge my mentors – Silvia Blemker and George Christ. I have taken an untraditional approach to graduate school and they have both supported me since day one. I am grateful that they agreed to co-mentorship and I have enjoyed the opportunity to learn from two great scientists simultaneously. When I got married during my second year and moved to Richmond, they were open to me working remotely and embraced my accelerated and aggressive timeline. Silvia and George brought different mentoring styles and points of view to my research. Both are highly motivated, passionate scientists and it was a privilege to work and learn from both.

I was also fortunate to work with other talented scientists here at UVA. Shayn Peirce-Cottler, Don Griffin, and Jason Kerrigan are all exceptional researchers who helped to guide my research through this dissertation. I am thankful for their time, guidance, and support during this journey.

I feel privileged to have the benefit of working with two labs during my time at UVA. To the members of the Multiscale Muscle Mechanophysiology Lab, thank you for your insight – especially with advice about presentations and posters. I am a better presenter and communicator because of your help. To the members of the Christ Lab, thank you for your patience and help with my studies. The last few months have been hectic and stressful, but you all have been supportive and made me laugh when things were overwhelming. Thank you, Julianna, for answering all my questions and your hospitality. I really appreciated not having to make the drive back to Richmond after long days in lab. I must give a special thank you to Sarah Dyer. I met Sarah during my first week of graduate school and she has helped me immensely over the years. She has been the biggest contributor to my research and helped me with *in situ* testing, explanting, animal care and so much more. Sarah's clam demeanor and great sense of humor brightened many stressful moments, and I am forever grateful for her friendship.

I am lucky to have the support of many long-distance friends and family. Kristin, Lauren, Sarah, and Kelly thank you for your phone calls, texts, and trips to visit each other. I am so thankful for your friendships in my life. It was not easy to move away from Boston, but I am extremely grateful for the network of friends that continuously supported me over these last few years. To the Allens, I am so grateful that our friendship has grown even more these years in VA. Our visits to see one another and frequent video chats have been a bright spot in this journey.

My mom and brother have been a constant source of support during this dissertation. The last few years have been challenging but I am so grateful that we have been able to laugh and find joy together. Thank you for your encouragement. Although my dad is not here to see this accomplishment, he really wanted one of his children to learn computer programming like him. For many reasons, I know he is proud of me, but I think he would be especially proud to know I can finally code in Java and a third of my dissertation was programming. I've also gained new family during grad school and I am especially grateful for the support of my mother-in-law, who was very encouraging during the stress of the last few months.

Last but certainly not least, I am beyond grateful for the support of my husband, Peter. He has without a doubt been the best part of this graduate school journey. We went on our first date about a month into grad school and I can't imagine completing this accomplishment without him as my partner. He has changed the direction of my life and helped me grow immensely as a person. Peter, thank you for your unwavering support, encouragement, and belief in me. You figuratively and literally picked me up when I didn't think I could do this. You made me breakfast in the morning, helped with dishes, cooked dinner, sent encouraging texts during long days in lab, helped me relax and find new hobbies, planned fun dates for us, listened to my struggles and frustration and were there to lift me up. I am so thankful that I get to do life with you and look forward to our next adventure together.

Abstract

Volumetric muscle loss (VML) injuries, where a loss of skeletal muscle results in functional impairment, can result from traumas and combat-related extremity wounds and are challenging to repair for there is a simultaneous loss of resident cells and structures responsible for muscle regeneration. Current preclinical therapeutics for these injuries fail to completely restore functional muscle tissue, and there is a need to better understand the functional and cellular mechanisms of regeneration in VML injuries in order to improve therapeutic design. We hypothesize that a novel experiment-modeling coupled framework will elucidate the mechanisms of VML injuries and serve as a guide to improve the design of therapeutics and experiments prior to expensive *in vivo* testing.

My dissertation developed two computational models to investigate the functional and cellular mechanisms of regeneration in VML injuries. First, I developed a finite-element (FE) model of *in situ* testing in the rat latissimus dorsi that provided new biomechanical insights regarding the relationship between VML injury location and corresponding force deficits in the rat LD muscle. The FE model can also be used to inform experimental design, such as injury location, injury size, and treatment effect on force production. Then I shifted focus to better understand cellular mechanisms of VML injuries and built an agent-based model (ABM). The model predicted tissue regeneration following VML injury using the autonomous behaviors of different agents in the model, including fibroblasts, satellite stem cells (SSCs), macrophages, and extracellular matrix. We simulated the tissue response of unrepaired VML injuries and acellular and cellular treatments. The ABM was also extended to identify new strategies for VML injury treatments and found that it was a combination of factors which impaired the

regeneration of new muscle fibers within the VML defect. Finally, the ABM was used to guide the design of a novel therapeutic and both computational models informed the experimental design. The ABM predicted that the addition of exogenous IL-10 to VML injuries would improve muscle regeneration, as indicated by the increased presence of fully differentiated SSCs, and this outcome was validated *in vivo*.

This body of work demonstrates the utility of computational models to inform functional and cellular mechanisms of VML injury regeneration and aid in therapeutic and experimental design. Experimental testing of new therapeutics is a resource-intensive and time-consuming process; however, we have demonstrated that computational tools offer a more cost-effective method to predict the effect of new therapeutics prior to *in vivo* testing. Moving forward, the experimental-modeling coupled framework has the ability to accelerate the development of more efficacious regenerative therapeutics to the clinic, and eventually, to guide injury specific treatment options for patients.

Contents

Acknowledgements	iii
Abstract	v
Chapter 1: Introduction	1
1.1 Overview	2
1.2 Background	5
Chapter 2: A coupled framework of in situ and in silico analysis reveals the role of lateral force transmission in force production in volumetric muscle loss injuries	13
2.1 Abstract	14
2.2 Introduction	15
2.3 Methods	17
2.4 Results	24
2.5 Discussion	31
Chapter 3: Agent-based model provides insight into the mechanisms behind failed regeneration following volumetric muscle loss injury	36
3.1 Abstract	37
3.2 Introduction	38
3.3 Methods	41
3.4 Results	57
3.5 Discussion	68
Chapter 4: Experimental-modeling coupled framework informs design of novel therapeutic for volumetric muscle loss injuries	73
4.1 Abstract	74
4.2 Introduction	75
4.3 Methods	77
4.4 Results	87
4.5 Discussion	96

Chapter 5: Conclusions	102
5.1 Summary	103
5.2 Contributions	104
5.3 Future applications	107
5.4 Final remarks	113
Appendix A: Perturbations of M1 and M2 macrophages regional distributions	114
Appendix B: Perturbations of decellularized ECM structure	116
Appendix C: Parameterization of SSC differentiation max chance	118
Appendix D: FE model predictions of circular injury	119
References	122

List of Figures, Tables, and Equations

Figures

Figure 1-1. Skeletal muscle regeneration overview.	8
Figure 1-2. Constitutive model of skeletal muscle.	11
Figure 2-1. Three-dimensional finite element model of the rat latissimus dorsi (LD).	18
Figure 2-2. Five different injury finite element models.	20
Figure 2-3. Force predictions of injury finite element models.	24
Figure 2-4. Experimental <i>in situ</i> force compared to finite element predictions.	26
Figure 2-5. Non-end-to-end and end-to-end fibers percentage and force contributions.	29
Figure 2-6. Along-fiber stretch distribution of Model I and Model V.	30
Figure 2-7. Relationship between lateral and longitudinal force transmission.	33
Figure 3-1. Histology of rat LD 7 days after VML injury.	39
Figure 3-2. ABM simulates muscle regeneration for 28 days following VML injury.	42
Figure 3-3. Flowchart of ABM rules, logic flow, and agent actions.	45
Figure 3-4. ABM of VML injury regeneration without repair.	58
Figure 3-5. ABM predictions of treated VML injuries.	61
Figure 3-6. ABM predictions limiting the number of M1 macrophages.	63
Figure 3-7. ABM predictions limiting the number of fibroblasts.	64
Figure 3-8. ABM predictions limiting growth factors produced by fibroblasts.	65
Figure 3-9. ABM prediction of combination of treatments.	67
Figure 4-1. Coupled framework of <i>in silico</i> and <i>in situ</i> methods.	76
Figure 4-2. Example of experimental regional cell count method.	86
Figure 4-3. Dose sensitivity analysis of exogenous growth factors using ABM.	88
Figure 4-4. Optimization of growth factor delivery using ABM.	88
Figure 4-5. Myotube count comparison of ABM predictions and <i>in vivo</i> data.	89
Figure 4-6. <i>In vivo</i> serum levels of IL-10.	90
Figure 4-7. Comparison of ABM predictions and <i>in vivo</i> data for unrepaired VML injuries.	91
Figure 4-8. Histology of rat LD muscle with unrepaired and treated VML injury.	92
Figure 4-9. Comparison of ABM predictions and <i>in vivo</i> data for decell ECM treatment.	93
Figure 4-10. ABM refinement of cellular regional distributions.	95
Figure 4-11. ABM refinement of myotubes and comparison with <i>in vivo</i> data.	96

Figure 5-1. ABM simulation of IL-10 in combination with cell-seeded decellularized ECM.	110
Figure A-1. ABM predictions of varied macrophage distributions.	115
Figure B-1. ABM predictions of varied decellularized ECM structure.	117
Figure C-1. Parameterization of SSC differentiation max chance in ABM.	118
Figure D-1. Finite element model simulations with circular injury.	121

Tables

Table 2-1. Material parameters for the LD muscle model.	19
Table 2-2. Animal weight and LD muscle weights.	21
Table 2-3. Normalized fiber lengths and active forces for Model I and Model V.	31
Table 3-1. Fibroblast agent behaviors.	48
Table 3-2. SSC agent behaviors.	49
Table 3-3. Unknown ABM probability parameters.	54
Table 4-1. Tuned ABM parameters.	81
Table 4-2. Animal weight and LD muscle weights.	84

Equations

Eqn 1. Cell behavior signal.	46
Eqn 2. Cell behavior probability.	46
Eqn 3. Genetic algorithm objective function.	51
Eqn 4. ODE for neutrophils.	52
Eqn 5. ODE for M1 macrophages.	52
Eqn 6. ODE for M2 macrophages.	52

Chapter 1

Introduction

“What is a weekend?” – Dowager Countess

Downton Abbey

1.1 Overview

Volumetric muscle loss (VML) injuries, where a loss of skeletal muscle results in functional impairment, can result from traumas and combat-related extremity wounds. In recent military conflicts, most injuries have been to extremities and a recent study found that in servicemembers who have been medically retired, VML injuries contribute to greater than 90% of muscular conditions that lead to long-term disability [1]. Current clinical treatments for VML injuries are limited to physical therapy and functional free muscle transfer, in which a healthy muscle from the patient is transplanted to the injury site to restore motor function and joint movement. However, this treatment requires sufficient healthy muscle to restore the defect, which is challenging in many combat-related extremities injuries; and functional free muscle transfer is associated with poor engraftment and donor site morbidity [2]. VML injuries contribute significantly to long-term disability of servicemembers [1], and there is a need for new therapeutics to restore the tissue and function in VML injuries.

Regenerative medicine is a promising alternative treatment for VML injuries that has focused primarily on two methods: implantations of acellular extracellular matrix (ECM) scaffolds alone, and ECM scaffolds seeded with a potentially myogenic cell source. *In vivo* VML injury rodent studies utilizing acellular ECM treatments have shown minimal fiber generation and extensive fibrosis filling the defect [3–7]. There is functional improvement in these treated injuries compared to unrepaired injuries which is believed to be a result of scaffold mediated functional fibrosis [4]. Cell seeded ECM therapeutics have shown improved functional recovery and regeneration via histological and molecular analyses compared to acellular treatments [3,6–9]. Although regions of muscle regeneration are seen closest to the remaining muscle,

there are limits to the injury size that can be repaired since there is minimal new fiber generation in the middle of the defects [6]. The biomechanical mechanisms responsible for function and the cellular mechanisms of tissue regeneration following VML injuries needs to be better understood to aid in the development of more effective therapeutics. This is an ideal opportunity to use computational models to determine the mechanisms of force production and unravel the complex cellular mechanisms in VML injuries that may be difficult to elucidate with only experimental tools.

We hypothesize that a novel experimental-modeling coupled framework will improve the efficiency and efficacy of therapeutics for VML injuries. Computational models, consisting of finite-element (FE) biomechanical models and agent-based cellular models (ABM), will help to understand mechanisms of these injuries as well as guide the design of therapeutics and improve experimental design prior to expensive *in vivo* testing.

In Chapter 2, we built and validated a biomechanical FE model to inform the effect of injury location on *in situ* force production. We created FE models of five distinct rat latissimus dorsi (LD) VML injuries and validated the predicted force deficit experimentally in two of these injuries. The coupled framework of *in situ* and *in silico* methods provided new biomechanical insights regarding the relationship between VML injury location and corresponding force deficits in the rat LD muscle. In the future, the FE model can be used to optimize experimental variables – such as injury location and size – and better design experiments prior to *in vivo* testing.

In Chapter 3, we developed an ABM that predicts tissue regeneration following VML injury to elucidate the cellular mechanisms contributing to failed muscle regeneration in these

injuries. Few studies have examined the cellular mechanisms and inflammatory response in VML injuries [10,11]; however, the use of an ABM provides a way to synthesize and integrate data in order to systematically predict how cellular mechanisms impact tissue repair. The ABM is focused on the autonomous behaviors of fibroblasts and SSCs and incorporates ECM agent behaviors as well as inflammatory agents through a series of ordinary differential equations. The ABM was first tuned to replicate cell population dynamics of unrepaired VML injuries and then was validated by simulating the treatment of VML injuries. Lastly, the ABM was extended to identify new strategies for muscle regeneration following VML injury and found that it was a combination of factors which impaired the regeneration of new muscle fibers within the VML defect. The ABM provides a predictive tool to optimize the design of new therapeutics and experimental variables to improve the efficacy of novel regenerative therapeutics for VML injuries.

In Chapter 4, we used our ABM from Chapter 3 to inform the design of a novel therapeutic and an experiment and then tested the model-derived predictions of the regenerative effect *in vivo*. Our novel therapeutic consisted of a decellularized ECM scaffold and exogenous growth factor. Informed by ABM simulations in Chapter 3, the exogenous growth factor component of the therapeutic was focused on factors to improve SSC behavior and perturbations identified IL-10 as the growth factor to include in our novel therapeutic. The predictive capabilities of the ABM model allowed testing of one therapeutic saving hundreds of hours of experimental work.

In this work, we have demonstrated that an experimental-modeling coupled framework can serve as a predictive tool to guide the design of therapeutics for VML injuries and aid in

experimental design. By utilizing both FE mechanical models and cellular ABMs, we are able to assess the functional response and tissue regeneration of therapeutics prior to *in vivo* testing. We also identified exogenous IL-10 as a direction for more complex therapeutics through the predictive capabilities of the ABM. Coupling the tools of computational modeling and tissue engineering fields has the ability to accelerate the development of more efficacious regenerative therapeutics, and thus, ensure the rapid clinical translation of therapeutics for VML injuries.

1.2 Background

1.2.1 VML injuries

Healthy skeletal muscle is capable of repairing damaged fibers after injury; however, in volumetric muscle loss (VML) injuries, where a large section of skeletal muscle is removed, the intrinsic regenerative process fails and results in functional impairment. VML injuries are common after trauma, including combat-related extremity wounds. In recent military conflicts, most injuries have been to extremities and in servicemembers who have been medically retired, VML injuries contribute to greater than 90% of muscular conditions that lead to long-term disability [1]. Current clinical treatments for VML injuries are limited to physical therapy and functional free muscle transfer, in which a healthy muscle from the patient is transplanted to the injury site to restore motor function and joint movement. However, this treatment requires sufficient healthy muscle to restore the defect, which is challenging in many combat-related extremities injuries; and functional free muscle transfer is associated with poor

engraftment and donor site morbidity [2]. VML injuries contribute significantly to long-term disability of servicemembers [1], and there is a need for new therapeutics to restore the tissue and function in VML injuries.

The treatment of VML injuries is challenging because the wound severity, size and locations varies widely. Regenerative medicine is a promising alternative treatment for VML injuries for it can address wound complexity because therapies can be tuned to the size of the injury and do not require healthy donor tissue. The focus of regenerative approaches has been primarily on two methods: implantations of acellular extracellular matrix (ECM) scaffolds alone, and ECM scaffolds seeded with a potentially myogenic cell source. *In vivo* VML injury rodent studies utilizing acellular ECM treatments have shown minimal fiber generation and extensive fibrosis filling the defect [3–7]. There is functional improvement in these treated injuries compared to unrepaired injuries which is believed to be a result of scaffold mediated functional fibrosis [4]. Cell seeded ECM therapeutics have shown improved functional recovery and regeneration via histological and molecular analyses compared to acellular treatments [3,6–9]. Although regions of muscle regeneration are seen closest to the remaining muscle, there are limits to the injury size that can be repaired since there is minimal new fiber generation in the middle of the defects [6]. Current therapies can be utilized to treat clinical injuries in the cleft lip [6], but most VML injuries occur in the extremities and the larger size requires further development of regenerative medicine approaches. However, the development of novel therapeutics is hampered because the functional and cellular mechanisms of VML injuries are poorly understood [11–13].

Another challenge in developing therapeutics for VML injuries is the *in vivo* model variability which makes it difficult to compare therapeutic efficacy. A wide variety of animal models and muscles are used, and within a specific muscle, different injury sizes and locations are studied [8,14–17]. An additional complication is that different functional testing methods are used to assess muscle recovery. A number of studies use *in vitro* testing where the muscle is completely explanted, others used *in situ* testing where the muscle is partially dissected but the muscle maintains blood supply and innervation, and some test muscle function *in vivo* [8,15,16]. All this variability makes it challenging to compare therapeutics and their functional effect.

1.2.2 Skeletal muscle regeneration after VML injury

Skeletal muscle possesses a remarkable capacity for repair and regeneration following a variety of injuries through a well described process governed by temporally-regulated, highly orchestrated, multicellular interactions (Figure 1-1 top row) [18,19]. Successful muscle tissue repair generally occurs within 28 days and involves 3 well documented phases [20–22]. First, an inflammatory response coordinated by an infiltration of neutrophils and pro-inflammatory macrophages to clear debris. The second phase, repair, follows with fibroblast and SSC activation and proliferation. Within 7 days post-injury, macrophages switch to an anti-inflammatory phenotype and fibroblasts and SSCs numbers peak. After 14 days, the remodeling (third) phase begins and fibroblasts undergo apoptosis and SSCs differentiate and fuse to repair existing myofibers.

However, in the setting of VML injuries, which are characterized by the simultaneous loss of multiple tissue compartments, the intrinsic regenerative process fails, resulting in permanent cosmetic and functional deficits. The repair process of skeletal muscle after VML injury is dominated by an inflammatory and fibrotic response, resulting in permanent loss of muscle volume and replacement of muscle with scar tissue (Figure 1-1 bottom row) [10,12,13]. The pro-inflammatory pathways remain upregulated for four weeks, as opposed to one week in successful muscle repair [11]. The number of fibroblasts and SSCs peak around day 7 before declining, and SSCs fail to differentiate and fibroblasts and myofibroblasts fill the defect space with fibrotic tissue, which includes densely packed collagen [4,11,23].

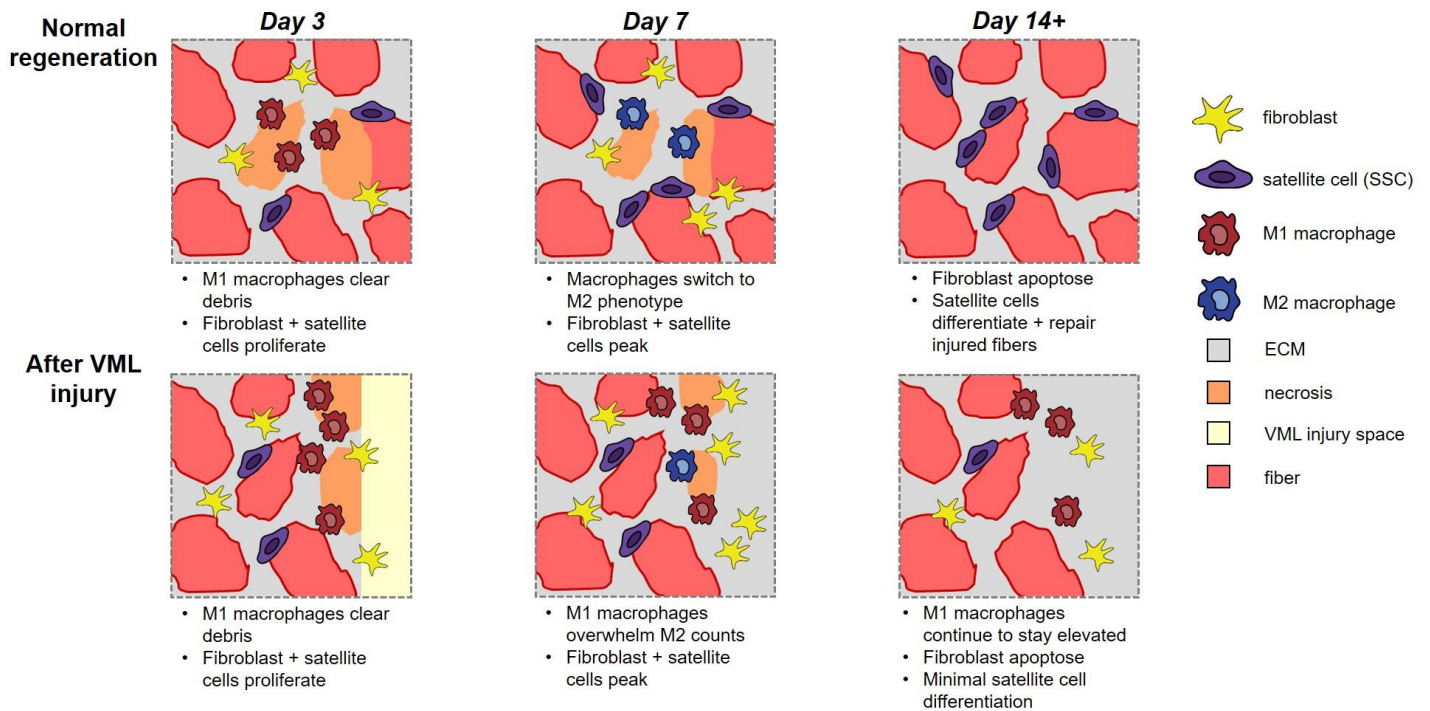


Figure 1-1. Skeletal muscle regeneration overview. *Top row:* normal regeneration where muscle is able to repair fibers and heal. *Bottom row:* after VML injury where regeneration fails.

Although few studies have examined the cellular mechanisms and inflammatory response in VML injuries, it is believed that many of the specific behaviors of SSCs and fibroblasts are consistent across injury types [10,20,24–26]. After injury, fibroblasts are recruited to the injury site by interleukin-4 secreted by eosinophils [10,27]. The growth factor myostatin, released by damaged ECM, promotes the proliferation of fibroblasts [28–30], while the transforming growth factor beta (TGF- β) causes fibroblasts to differentiate to myofibroblasts [10,11,13,31]. Fibroblasts and myofibroblasts secrete collagen and fibronectin to rebuild the ECM, as well as other growth factors such as TGF- β , insulin-like growth factor (IGF), interleukin-6 (IL-6), fibroblast growth factor (FGF), and matrix metalloproteinases (MMPs) [32–39]. SSCs are responsible for the repair and maintenance of skeletal muscle fibers. Typically, SSCs are quiescent at the muscle fiber membrane and then are activated by hepatocyte growth factor (HGF) released from the ECM after injury [40–43]. SSCs are recruited to the injury site by a combination of growth factors, including HGF, IGF, FGF, and MMPs [44–47]. There are microenvironmental and secreted factors that influence SSC proliferation and differentiation. Once SSCs are terminally differentiated to myotubes, the myotubes fuse with an existing fiber to repair the muscle or put down muscle protein to start a new fiber [48–50]. Approximately 10% of the SSC population does not undergo differentiation and restores the SSC pool [51–53].

1.2.3 Skeletal muscle FE model of VML injury

Three-dimensional FE modeling provides a framework to represent muscle as a fiber-reinforced composite using a skeletal muscle constitutive model [54]. In the constitutive model, skeletal muscle is represented as a transversely isotropic, hyperelastic and quasi-incompressible material with a preferred direction. The preferred direction corresponds to the fiber trajectories of the muscle. The model uses an uncoupled form of the strain energy density function to enforce the incompressible behavior. The strain energy density function is separated into the deviatoric and dilatational tissue responses and uses physically-based strain invariants to relate material parameters to physically meaningful measures (Figure 1-2). The deviatoric component represents the contributions to strain energy from the along-fiber stretch (λ), along-fiber shear (B_1), and cross-fiber shear (B_2). The along-fiber stretch parameter determines both the active and passive force-length properties of muscle and the active force-length relationship is scaled by the muscle activation (α). G_1 and G_2 are the along-fiber and cross-fiber shear moduli, respectively. The dilatational component of the strain energy density function penalizes volume changes, where K is the bulk modulus and J is the relative change in volume.

FE skeletal muscle models incorporate muscle geometry, fiber architecture, shear properties, volume preservation, and active and passive muscle fiber characteristics to create a tool which can be used to explore and analyze the mechanisms of muscle function [54]. A number of human skeletal whole muscle models have been developed to: 1) determine the force production of individual muscles at varying locations within the pelvic floor [55], 2) evaluate stretch and strain changes during contraction of the biceps brachii and biceps femoris

longhead [54,56], and 3) assess the effects of muscle activation in cleft palate repair [57].

Additionally, FE micromechanical models have been used to separate muscle fibers and ECM and investigate how changes in the microstructure and how changes associated with disease affect tissue level material properties [58,59]. Another study used a FE model to explore the relationship between force production and VML injury treatment properties [6]. We used the FE skeletal muscle model to improve mechanistic understanding of how VML injury location affects the corresponding functional deficits (Chapter 2).

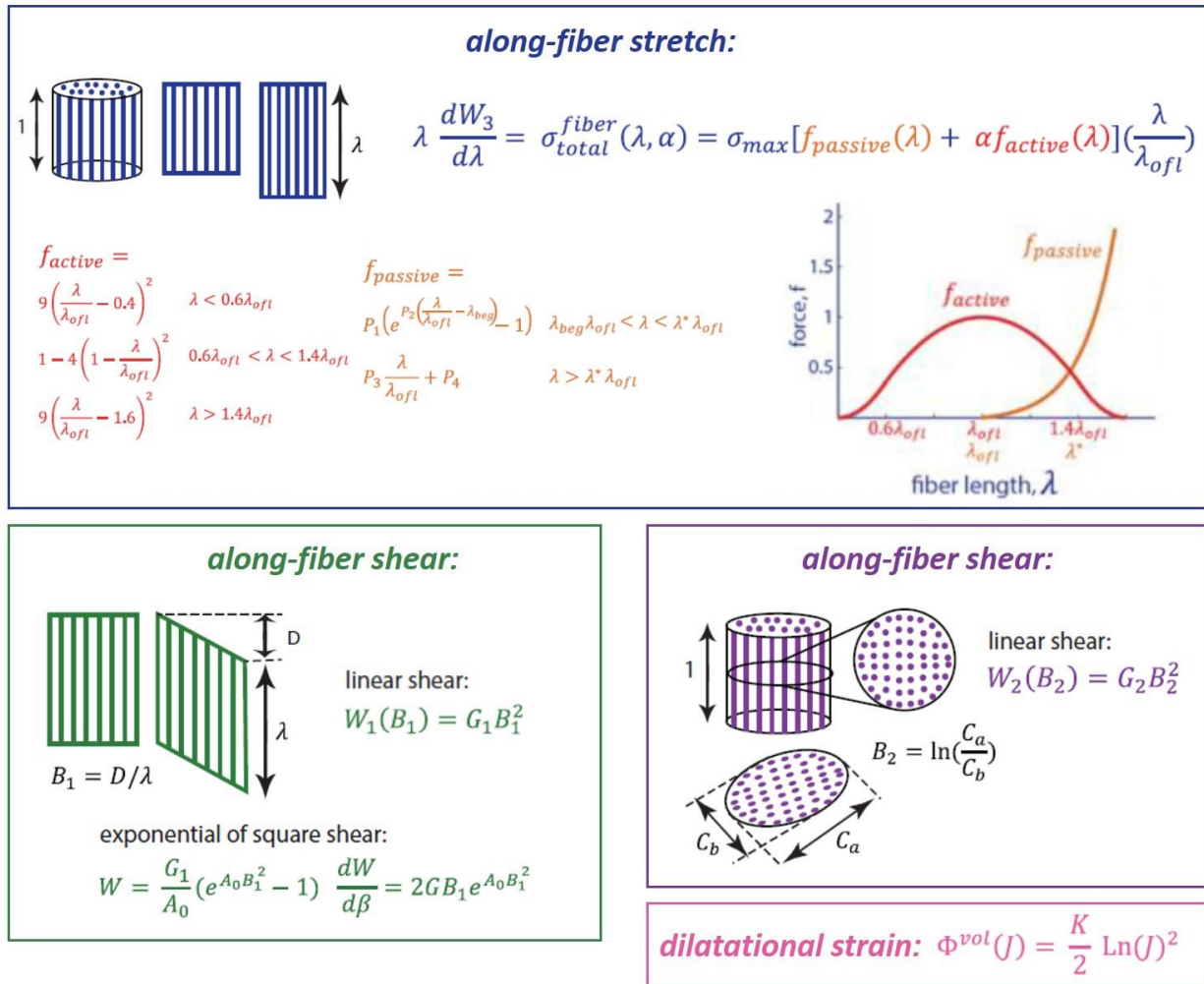


Figure 1-2. Constitutive model of skeletal muscle.

1.2.4 Skeletal muscle ABM of VML injury

Agent-based models simulate cellular behaviors and show the effects of these cellular behaviors on the system as a whole. The platform provides a compilation and synthesis of the work in the field, as cellular behaviors are prescribed by literature-derived rules to cells (agents). The stochastic, rules-based approach of autonomous agents leads to emergent, system-level behaviors providing insight into biological interactions and processes. Our group has previously developed an ABM of muscle regeneration focused on the role of inflammatory cells in disuse-induced muscle atrophy and following laceration injury [60,61]. The injury and muscle regeneration ABM was then expanded to study how different Duchenne muscular dystrophy mechanisms influence muscle regeneration [62]. Building upon this work, we expanded the use of ABMs to study the cellular responses following VML injury to improve mechanistic understanding of how cellular behaviors contribute to failed muscle regeneration in VML injuries and to serve as a tool to guide the development of therapeutics (Chapter 3).

Chapter 2

**A coupled framework of *in situ* and *in silico* analysis
reveals the role of lateral force transmission in force production
in volumetric muscle loss injuries**

Acknowledgements: Sarah Dyer, David Remer, Xiao Hu,
George J. Christ, Silvia S. Blemker

“Clear eyes, full heart, can’t lose.” – Coach Taylor
Friday Night Lights

2.1 Abstract

Volumetric muscle loss injuries (VML) are challenging to treat because of the variability in wound location. Regenerative medicine offers promising alternative treatments, but there is little understanding of the correlation between magnitude of VML injuries and corresponding functional deficits that must be addressed. There is a need for a tool that can elucidate the relationship between VML injury and force loss, as well as the impact on specific mechanisms responsible for force production. The purpose of this study was to develop a novel coupled framework of *in situ* and *in silico* methods to more precisely understand the relationship between injury location and force production deficits. We created a three-dimensional finite-element model of the pennate latissimus dorsi (LD) muscle in the rat and validated the model experimentally. We found that the model's prediction (2.6 N/g Model I, 2.1 N/g Model V) compared favorably to *in situ* testing of isometric force generation of the injured rat LD muscle (2.8 ± 0.3 N/g Experimental I, 2.1 ± 0.2 N/g Experimental V). Further model analysis revealed that the contribution from lateral and longitudinal force transmission to the total force varied with injury location and led to a greater understanding of the mechanisms responsible for VML-related force deficits. In the future, the coupled computational and experimental framework can be used to inform development of preclinical VML injury models that better recapitulate the spectrum of VML injuries observed in affected patients, and the mechanistic insight can accelerate the creation of improved regenerative therapeutics for VML injuries.

2.2 Introduction

Volumetric muscle loss (VML) injuries result in a permanent loss of muscle structure and function. These types of deficits can result from congenital diseases and are also common after trauma, including combat-related wounds. Development of technologies to treat VML injuries is hampered by the fact that the spectrum of injuries and wound locations vary widely [1].

Regenerative medicine is a promising approach for the treatment of these injuries that has the potential to address the complexity of VML wounds; however, within the literature, a wide variety of *in vivo* models are currently used to study these injuries — making straightforward comparisons of the efficacy of distinct technologies challenging. Most commonly, VML injuries have been studied in limb muscles of rodents [8,15,63,64]. These studies utilize injuries that differ in location; therefore, the measured magnitudes of corresponding functional deficits vary widely. Taken together, these observations reinforce the importance of improved understanding of the mechanisms responsible for VML-induced force deficits. The focus of this study is to systematically characterize the impact of injury location on the biomechanics of force production in intact and VML-injured muscles in the rat latissimus dorsi (LD) muscle—a pennate muscle that is clinically relevant and dimensionally similar to human craniofacial muscles that are affected by VML injuries [65].

In this regard, force production within skeletal muscle is dependent on both the active and passive muscle fiber characteristics and the intramuscular connective tissue properties [66,67]. In the case of VML injuries, the direct connection of myofibers to the tendon is disrupted which dramatically impairs the ability of the fibers to transmit force longitudinally. Previous studies have shown that skeletal muscle fibers without direct myotendinous

connections have the potential to contribute to force production within a muscle by transmitting force laterally through the connective tissue [67–69]. It stands to reason, therefore, that lateral force transmission contributes to force production in VML injuries. However, it remains unclear how injury location affects the contribution of lateral force transmission to whole muscle force production.

In silico three-dimensional finite-element (FE) modeling provides a framework for determining the complex relationship between injury location and force production in VML injuries. FE skeletal muscle models incorporate muscle geometry, fiber architecture, shear properties, volume preservation, and active and passive muscle fiber characteristics to create a tool which can be used to explore and analyze the mechanisms of muscle function [54]. For example, a number of human skeletal whole muscle models have been developed to: 1) determine the force production of individual muscles at varying locations within the pelvic floor [55], 2) evaluate stretch and strain changes during contraction of the biceps brachii and biceps femoris longhead [54,56], and 3) assess the effects of muscle activation in cleft palate repair [57]. Additionally, an FE model with simplified muscle structure has been used to study the mechanics of force transmission between extracellular matrix and myofiber [70,71]. However, to our knowledge, there are no published reports using FE skeletal muscle modeling to improve mechanistic understanding of how VML injury location affects the corresponding functional deficits.

Our goal, therefore, was to develop a coupled framework of *in situ* and *in silico* methods to uncover the relationship between VML injury location and muscle force production. The *in silico* models allow us to optimize experimental variables, such as injury location, and better

design experiments prior to expensive *in vivo* testing. This report focused on using the capabilities of the model in a manner that extends beyond experimental analysis to explore how VML injury can alter the contributions of lateral and longitudinal force transmission. As a first step in this direction, we created FE models of five distinct rat LD VML injuries, validated the predicted force deficit experimentally in two of these injuries, and then used the analytic capabilities of the model to identify and compare the biomechanical mechanisms governing force production/force loss among the distinct injury locations.

2.3 Methods

2.3.1 Finite-element Model

The three-dimensional FE model of an intact rat LD was created based on measurements from dissected LDs of four male Lewis rats [6]. The x-y dimensions and weight of the LDs were measured, and the thickness was measured at 12 locations around the LDs. Three-dimensional model of the LD was simplified to have a shape that combines one rectangle and one triangle medial in the x-y plane with varying thickness in the z-direction (Figure 2-1A model compared to Figure 2-4C explanted intact muscle). The FE model was meshed using 4-node enhanced tetrahedral elements (4149 elements) in AMPS finite-element software (AMPS Technologies).

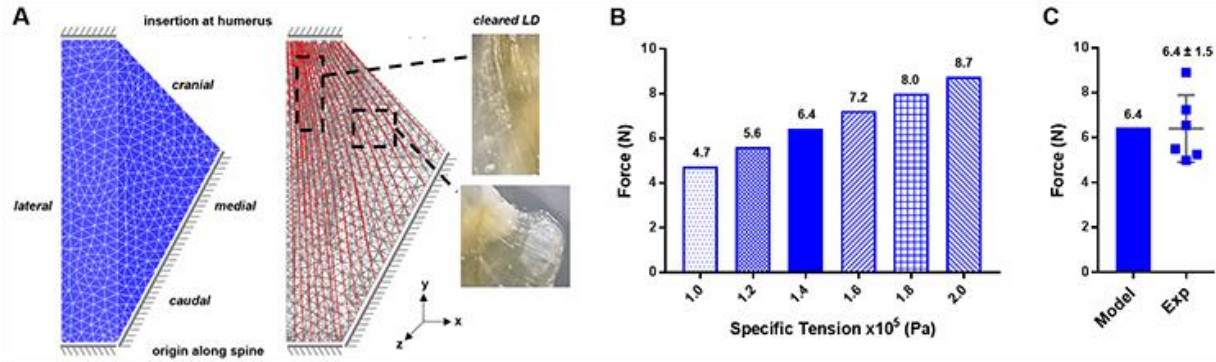


Figure 2-1. Three-dimensional finite element model of the rat latissimus dorsi (LD) constrained as shown along the cranial rectangular edge and caudal rectangular and triangular edges with the elements (A, left). The model fiber trajectories highlighted (A, middle) are similar to the observed fiber directions of a cleared LD muscle (A, right). Sensitivity analysis of specific tension parameter to determine ideal parameter value (B). Intact LD model was calibrated to intact experimental data ($n = 6$), and specific tension of 1.4×10^5 Pa best replicated experimental isometric force measurements of intact LDs (C).

2.3.1.1 Muscle model

Skeletal muscle properties were implemented using a constitutive relationship that has previously been described in detail [54]. The LD was modeled as a transversely isotropic, hyperelastic and quasi-incompressible material with a preferred direction. Muscle fiber direction originates along the spine and runs to the insertion at the humerus (Figure 2-1A). Fiber trajectories were determined using computational fluid dynamics and then each element of the model was assigned a fiber direction (Figure 2-1A) [72,73]. The model's along-fiber stretch captures the longitudinal force development and transmission in the same direction using active [66] and passive stress-strain relationships [54]. Model fiber stretch is defined as $\lambda = l/l_0$ ($\lambda < 1$ for a shortening fiber), l is the final fiber length, and l_0 is the initial fiber length and assumed to be at optimal length. The model's shearing along and across the fiber direction is representative of lateral force transmission between fibers via the extracellular matrix.

The intact LD muscle model was calibrated to fit intact experimental data of isometric force. The LD thickness varies across its length and width making it challenging to calculate the true cross-sectional area and thus determine the peak isometric stress (σ_{\max}) of the rat LD. A sensitivity analysis of the σ_{\max} parameter was run (Figure 2-1B), model force outputs were compared to intact experimental data, and 1.4×10^5 Pa was the parameter value which best replicated an *in situ* LD muscle (Figure 2-1C). The final model parameter values used in this study for both intact and injured models are in Table 2-1.

Table 2-1. Material parameters for the LD muscle model [54]. Passive parameters (P_1 , P_2 , λ^*) were determined experimentally [6].

σ_{\max}	P_1	P_2	λ^*	G_1	G_2	K
Pa	dimensionless			Pa	Pa	Pa
1.4×10^5	0.0043	14.2395	1.3306	3870	22400	1×10^7

2.3.1.2 Model simulations

To replicate *in situ* experimental testing conditions, the cranial rectangular surface and caudal rectangular and triangular edges of the model were fixed. In total, five different injuries (11x15 mm and entire thickness of the muscle) were created at various locations within the muscle model (Figure 2-2) and isometric contractions were simulated (Strain-Enriched FEA, AMPS Technologies). First, an injury was created in the middle of the rectangular portion of the LD (Model I) and then the injury was moved within the boundaries of the muscle and below the thoracodorsal motor nerve (Model II – V). It would not be possible to stimulate the LD using *in situ* testing if an injury removed the motor nerve innervation. Muscle activation levels were set at the maximum activation for all trials to simulate maximum tetanic force. Total force of the

modeled LD was measured in the y-direction on the cranial rectangular surface in the x-z plane. A mesh sensitivity analysis of the intact LD model demonstrated that a consistent force value is achieved with meshes greater than 2000 elements. Injury model mesh counts were all above this minimum value, providing confidence in the output force of these models.

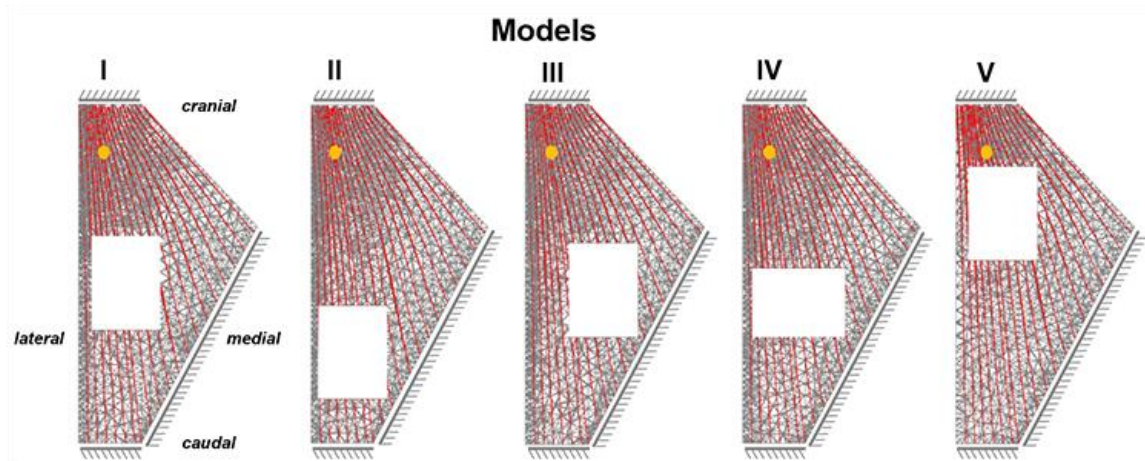


Figure 2-2. Five different injuries ($11 \times 15 \text{ mm}^2$) were created in the rat LD model at varying locations within the muscle. Red lines across each muscle represent the fiber direction, and the yellow dot represents the thoracodorsal nerve location. First, the injury was placed in the middle of the rectangular portion of the LD (Model I) and then the injury was moved within the anatomical constraints of the muscle. The movement of the injury was limited by the muscle boundary as well as the nerve location.

2.3.1.3 Model analysis

To directly compare model predictions and experimental measurements, the model force prediction was normalized to LD model weight. The model is a simplified geometry of the LD muscle and likely overestimates the true volume of the LD, thus the rat LD model assumed mass per unit volume was calculated by dividing the average weight of intact experimental LDs (Table 2-2) by the intact muscle model volume. Then the weights of Models I (1.570 g) and V

(1.521 g) were determined using the model volumes and calculated rat LD model assumed mass per unit volume.

To determine force generation for the end-to-end fibers region of the muscle, MATLAB was used to identify the nodes on the cranial x-z surface which corresponded to end-to-end fibers and then force production from those specific nodes was measured in AMPS. Model outputs of along-fiber stretch and along-fiber shear strain distributions were assessed at the time of maximum contraction. The normalized fiber lengths within the models were determined by mapping the fiber trajectories from computational fluid dynamics through the FE mesh and then tracking those fibers throughout the simulation to determine their change in length and pennation angle using MATLAB (MathWorks) software [6].

Table 2-2. Animal weight and LD muscle weights.

Group	Animal weight (g)	Excised muscle weight (g)	LD muscle weight (g)
Intact (n = 6)	405.1 ± 29.9	0	1.890 ± 0.234
Experimental I (n = 5)	416.7 ± 30.7	0.282 ± 0.380	1.903 ± 0.112
Experimental V (n = 6)	417.0 ± 34.7	0.122 ± 0.010	1.878 ± 0.220

2.3.2 Animals

In total, 17 Male Lewis rats (Charles River Laboratories) aged 20 weeks were used for *in situ* analysis. The Institutional Animal Care and Use Committee of the University of Virginia approved all animal procedures.

2.3.3 *In situ* testing of the rat LD muscle

2.3.3.1 Surgical setup

Custom nerve cuffs were made to directly stimulate the thoracodorsal nerve innervating the rat LD [16]. The cuffs consisted of silicone tubing (0.762 mm inner diameter, Dow Corning) and two stainless steel wires (Cooner Wire) running through the tubing. A slit the length of the tube allowed the nerve to be placed inside.

While under isoflurane anesthesia, a 10 cm incision was made from the base of the neck down the spine of the rat and another posterior incision was made the length of the left forelimb. The entire left LD was exposed and the tendon insertion point on the humerus was dissected. The tendon was cut and then pierced once with 3-0 silk suture right above the tendon-muscle insertion so as not to injure the muscle and impact force production. Additional 3-0 silk was knotted around the tendon to adequately secure the suture to the tendon. Approximately 15 mm of thoracodorsal nerve was then carefully dissected from the muscle. The nerve was placed in the nerve cuff and suture was tied around the cuff to keep the nerve in place.

For VML injury groups, the injury was made in the LD prior to cutting the tendon. With the LD exposed, a defect 11 x 15 mm² was excised from the LD muscle in two different locations, both 1-2 mm from the lateral edge of the LD. For Experimental Injury I, the bottom edge was placed 5 mm above the caudal edge of the rib cage. For Experimental Injury V, the top edge was placed 10 mm below the cranial edge of the LD.

2.3.3.2 *In situ* measurements

Immediately following surgical setup, *in situ* functional assessment was performed as previously described with modifications using an Aurora muscle lever system (Aurora Scientific, Mod 305C-LR-FP) [16]. Under anesthesia, the rat was placed in the right lateral recumbent position on a heated platform and the tendon suture was connected to the lever arm. The rat was anchored to a metal rod running along the platform by its spine to prevent the rat from shifting during muscle contraction. The nerve was stimulated through the nerve cuff using an Aurora Scientific stimulator (Model 701C). Muscle length was optimized using stimulations at 1 Hz to identify the muscle length with the largest twitch contraction. A stimulation of 1 Hz was used because at higher frequencies, the suture is more likely to rip out of the tendon; therefore, we needed to minimize the number of high frequency stimulations to avoid damage during the experiment. Contractile function of the LD was assessed at the determined optimal length by measuring isometric force at a range of stimulation frequencies to ensure tetanic force was reached (10-200 Hz). After testing, animals were euthanized via CO₂ inhalation and the LD muscle was harvested. Peak isometric force was determined to be the maximum force value achieved at a frequency greater than 100 Hz. Each maximum isometric force value was then normalized to the weight of the muscle to account for biologic variability between animals.

2.3.4 Statistical Analysis

All weights and experimental isometric force values were reported as mean values with standard deviation and compared between groups using a one-way analysis of variance

(ANOVA). Force-frequency curves were reported as mean values with standard deviation and compared between groups using a two-way ANOVA. If significant differences were observed in any statistical test, a Holm-Sidak post hoc test was performed. The level of significance was set at $P < 0.05$ in all statistical tests (GraphPad Prism).

2.4 Results

2.4.1 Model prediction of injury location effect

Moving the injury location within the boundaries of the muscle demonstrated that a caudal injury (Model II) generates a force value closest to an intact muscle (Figure 2-3). An injury in the middle of the muscle (Model I) resulted in generation of 4.1 N of force, 36% lower than intact muscle. Other injuries in the middle region (Models III and IV) generated comparable force values to Model I. The injury location that created the largest force deficit from intact was located cranially (Model V), and this model isometric force prediction was 50% lower than an intact LD.

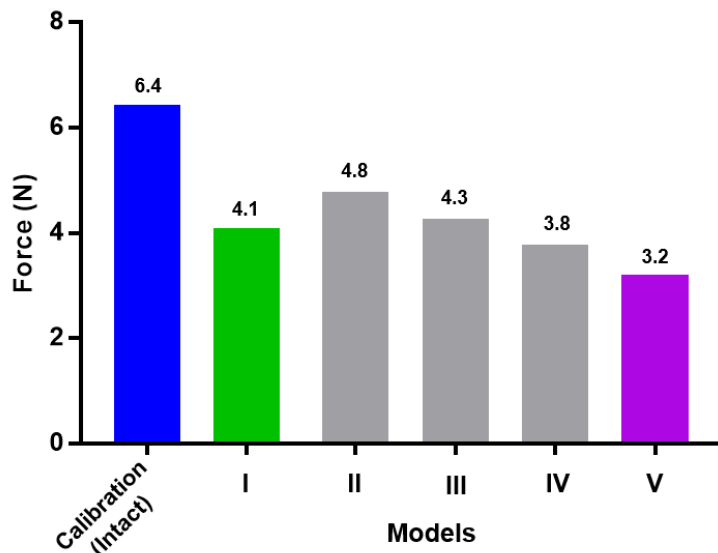


Figure 2-3. The injury in the middle of the rectangular portion (Model I) generated 36% less force than the intact muscle. A sensitivity analysis to injury location showed that the model simulated force production of the injury near the cranial boundary of the muscle (Model V) resulted in the smallest force value compared to intact.

2.4.2 Experimental validation of injury location effect

First, the injury location of Model I was created *in vivo* and force production was immediately tested *in situ* (Figure 2-4C). The predictions of Model I, 2.6 N/g, were validated by the experimental force values, 2.8 ± 0.3 N/g (Figure 4A). Then the force predictions of Model V, 2.1 N/g, were tested and confirmed by the experimental results, 2.0 ± 0.2 N/g (Figure 2-4A). There was a significant difference in isometric force between all experimental groups. The force-frequency plots in Figure 2-4B demonstrate that maximum tetanic force was reached in all groups. Furthermore, at any frequency above 40 Hz, the normalized force of contraction for Experimental Injury V and Experimental Injury I was significantly less than the intact group (Figure 2-4B). Animal weights and LD muscle weights remained similar between groups with no significant difference measured (Table 2-2).

For both Experimental Injury I and V groups, the injury area (11×15 mm²) was consistent; however, a smaller muscle weight was excised for Experimental Injury V compared to I. The fibers cranially are under more tension *in vivo*, and thus, when muscle is excised, fibers contract and the defect is larger than originally measured. Therefore, less muscle was excised for Experimental Injury V to create an injury with the same dimensions as Experimental Injury I (upper panels of Figure 2-4C show the equivalent size of injuries I and V). When the LD muscles were excised and no longer under tension, the difference in excised muscle tissue volume was again obvious (lower panels of Figure 2-4C show the size of Experimental Injury V was clearly smaller than Experimental Injury I).

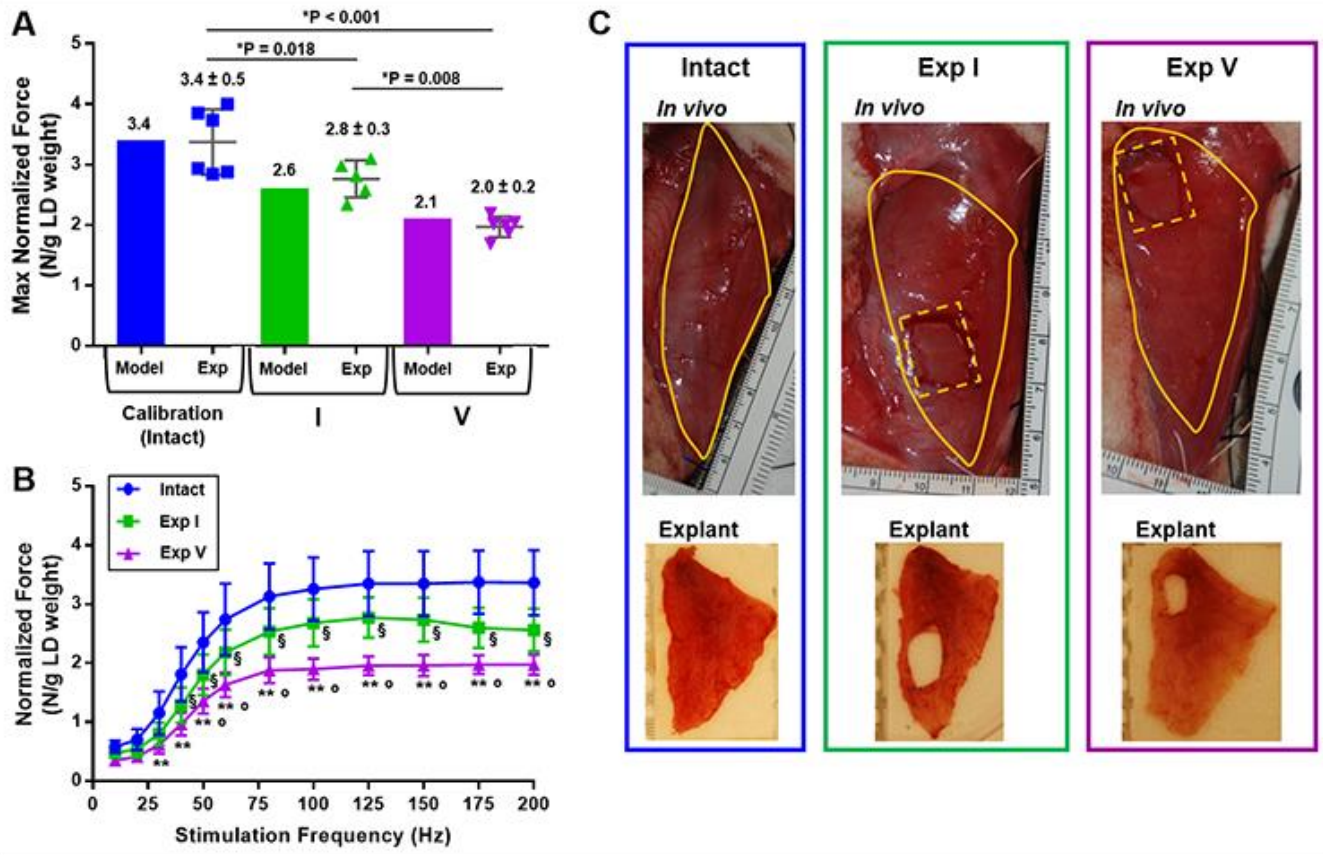


Figure 2-4. Results of groups Experimental I (n = 5) and Experimental V (n = 6), shown as scatter dot plots, validate the model normalized force predictions, shown as bars (A). The LD weight normalized force-frequency curves demonstrate that maximum tetanic isometric force was achieved for each group (B). ** indicates statistical significance between intact and Experimental V, § indicates significance between Experimental I vs Experimental V, and § is for intact compared to Experimental I. Representative images of intact, Experimental I and Experimental V LDs just before testing (*in vivo*) and after harvest (explant) (C). Solid yellow line denotes approximate boundary of LD muscles *in vivo* and dashed yellow boxes mark injury border.

2.4.3 Analysis of injury location effect

The mechanisms responsible for the observed difference in force production between the 5 distinct injuries was explored using the FE LD model. Injury location affects the percent of non-end-to-end fibers attached at the cranial edge of the LD muscle (Figure 2-5A). In Model II, for example, the injury is in the most caudal portion of the muscle and 26% of the fibers attached cranially are non-end-to-end. As the injury is moved cranially, the region of non-end-to-end fibers increases and at the most cranial point of injury (Model V), 45% of the fibers are non-end-to-end. The increase in cut fibers contributes to the lower isometric force of the cranial injury location.

The non-end-to-end fibers are not anchored caudally and thus must contribute to force production by laterally transmitting force to end-to-end fibers through the connective tissue [67–69]. The extent to which non-end-to-end fibers contribute to total muscle force provides a measure of the contribution of lateral force transmission in the muscle, and this non-end-to-end fiber force contribution varied between injuries (Figure 2-5A). Model II has the smallest percentage of non-end-to-end fibers and thus those fibers contribute the least to total force compared to other injured muscles (12%). On the other hand, Model V has the largest percent of non-end-to-end fibers; however, these fibers generate less force than end-to-end fibers and the result is a smaller total force.

Lateral force transmission increases in injured compared to intact muscle as highlighted by the along-fiber shear strain distributions of the intact model, Model I and Model V at the time of maximum isometric force (Figure 2-5B). During activation of intact and injured muscles, fibers slide past each other causing the connective tissue to deform and experience stress.

Therefore, larger shear strains are indicative of larger shear deformations of the connective tissue which physically translates to larger contributions of lateral force transmission [58]. Comparison of the along-fiber shear strains of the models demonstrates that injury location affects the magnitude and distribution of shearing within the muscle compared to intact muscle. Focusing specifically on the triangular portion of the LD, the intact model shows minimal along-fiber shear strain, Model I shows areas with increasing strain, and Model V shows distinct areas of large shear strain.

To better understand the difference in force production between the two injuries tested experimentally, longitudinal force transmission was also explored for Models I and V. The along-fiber stretch distributions at the time of maximum force show regional variability along the muscle length (Figure 2-6A, C). To quantify the difference between injuries, normalized fiber length for both regions of non-end-to-end and end-to-end fibers was measured at the point of attachment. In Model I, 33% of the fibers are non-end-to-end and operate low on the ascending limb of the force-length curve and generate minimal isometric force (Figure 2-6B, Table 2-3). In Model V, 45% of the fibers are non-end-to-end and operate very low on the ascending limb of the force-length curve contributing to a total weighted normalized fiber force of 0.488 (Figure 2-6D, Table 2-3). This is lower than the weighted normalized fiber force of Model I, 0.557, and contributes to the lower observed isometric force of the cranial injury location.

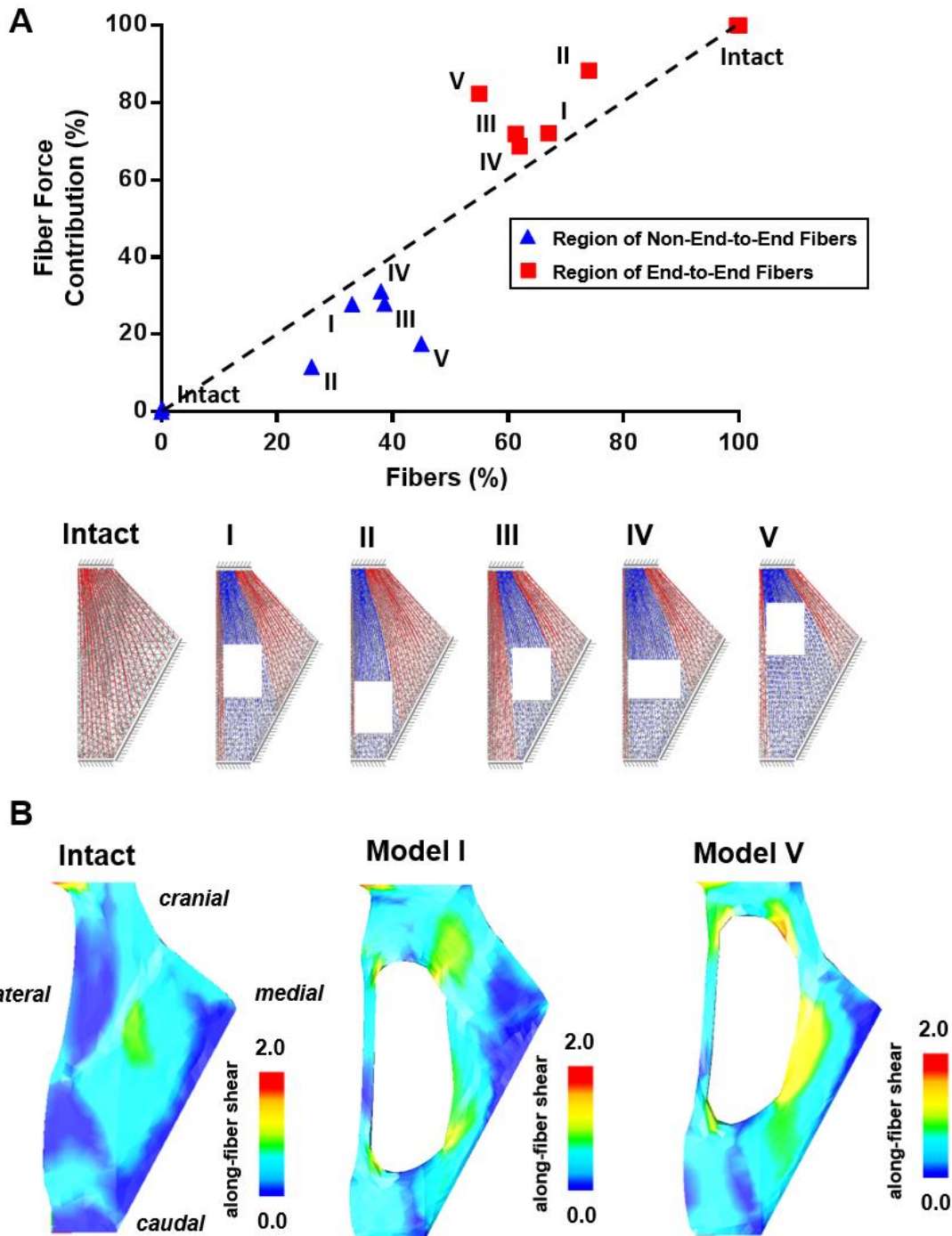


Figure 2-5. Injury location affects the percent region of non-end-to-end (blue) and end-to-end fibers (red) present and their respective force contribution (A). The force contribution of the region of non-end-to-end fibers is evidence of lateral force transmission. All fibers in the model are active during the model simulation, and the regional fiber percentages are quantified on the cranial x-z surface of the LD. Along-fiber shear strain distributions of the intact model, Model I and Model V at the time of maximum isometric force provide additional evidence of lateral force transmission and highlight the effect of injury location on shear distributions (B).

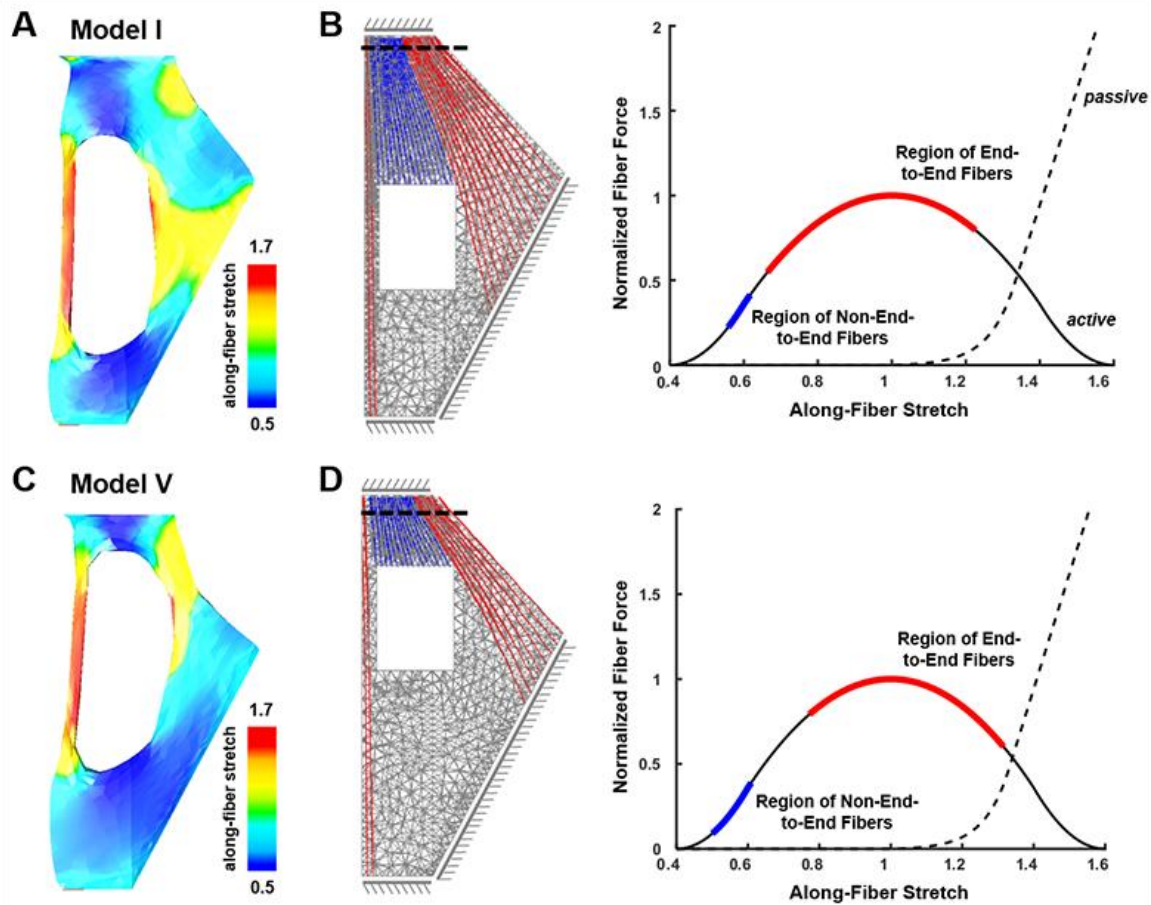


Figure 2-6. The along-fiber stretch distribution at the time of maximum force contraction shows regional variations in fiber length for both Model I (A) and Model V (C), where the models assume all fibers start at their optimal fiber length and stretch < 1 for a shortening fiber. Further analysis into fiber length variability measured the normalized fiber length of the region of non-end-to-end (blue) and end-to-end fibers (red) 3 mm from the cranial attachment of the LD (dotted line on LD). In Model I, 67% of the fibers are end-to-end and operate near the optimal length on the force length curve and are capable of generating optimal force production (B). In Model V, 45% of the fibers are non-end-to-end and operate very low on the ascending limb of the force-length curve and account for the low force production of the injured muscle (D). Force-length curves depict the standard deviation range for each fiber region.

Table 2-3. The normalized fiber lengths and active forces for end-to-end and non-end-to-end fibers for both Model I and Model V. Fiber lengths and fiber region percentages were measured from model deformations. The normalized fiber force was determined from the active force-length curve using the calculated normalized fiber length. Total normalized fiber force for the muscle was found by weighting the calculated average fiber force by each fiber region percentage.

Group	Fiber Type	Normalized along-fiber stretch	Normalized fiber force	Fiber region percentage	Total weighted normalized fiber force
<i>3 mm from cranial edge of LD</i>					
Model I	End-to-End	0.945 ± 0.280	0.675 ± 0.240	67.0%	0.557
	Non-End-to-End	0.587 ± 0.030	0.317 ± 0.092	33.0%	
Model V	End-to-End	1.04 ± 0.27	0.700 ± 0.250	55.0%	0.488
	Non-End-to-End	0.555 ± 0.055	0.230 ± 0.150	45.0%	

2.5 Discussion

VML injuries are a challenging medical condition to treat because of the variability in wound location, which translates into a wide spectrum of permanent functional deficits. While VML injuries are inadequately treated with current treatments, regenerative medicine technologies offer great potential for improved functional outcomes [8,15,16]. However, more rapid and efficient clinical translation of regenerative therapeutics would likely be aided by a computational tool that can capture the intrinsic variability of VML injuries to first predict anticipated functional outcomes of specific VML injuries, and eventually, to guide injury specific treatment options. Thus, we report the development of a novel coupled framework of *in situ* and *in silico* methods that provides important new biomechanical insights regarding the relationship between VML injury location and the corresponding force deficits produced in a clinically relevant rodent LD model.

The use of three different experimental data sets to create (intact data), validate (injury I), and test (injury V) our FE models provides strong confidence in the validity of the model. The predictive force capabilities of the model allowed testing of only two experimental injuries, instead of five, which saved over 90 hours of experimental work and approximately 30 rats. Additionally, the force production of Experimental Injury V injury was comparable to another published study which experimentally evaluated a smaller VML injury also near the cranial portion of the rat LD *in situ* [16].

The experimental and computational coupled framework of this study allows us to explore the relationships between injury location, force production, and the responsible biomechanical mechanisms. The FE model simulations predicted that, for injuries with identical areas, location can have a dramatic effect on force production. Specifically, the cranial injury location (Model/Experiment V) resulted in a functional isometric force deficit 40% below intact values, whereas the same injury area in the middle of the LD (Model/Experiment I) produced a functional deficit only 20% lower than intact values, Figure 2-4A. Interestingly, approximately 6% of the LD weight was removed with Experimental V and about 15% of the LD was removed with Experimental I, yet Experimental V generated 0.8 N/g less force than Experimental I.

Analysis of fiber regions in each injury location model was consistent with the previous experiments that suggest non-end-to-end fibers contribute to force production by laterally transmitting force to end-to-end fibers [67]. We found that the percent of non-end-to-end fibers increases as an injury location moves cranially, and the percent force contribution of non-end-to-end fibers varied with injury location. Specifically, the percent of injured fibers affects how lateral force transmission influences total force production (Figure 2-7). Models II and III

generate more force than would be predicted if there was no lateral transmission indicating that lateral transmission improves force production. However, comparison of Model V to this idealized scenario indicates that force production is impaired. This may be a result of the large number of injured fibers causing larger deformations, increased shearing, and thus impairing longitudinal force transmission as shown by the increased range of end-to-end fiber lengths and suboptimal normalized fiber force (Figure 2-6D, Table 2-3). Future studies will further explore this complicated relationship between lateral and longitudinal force transmission.

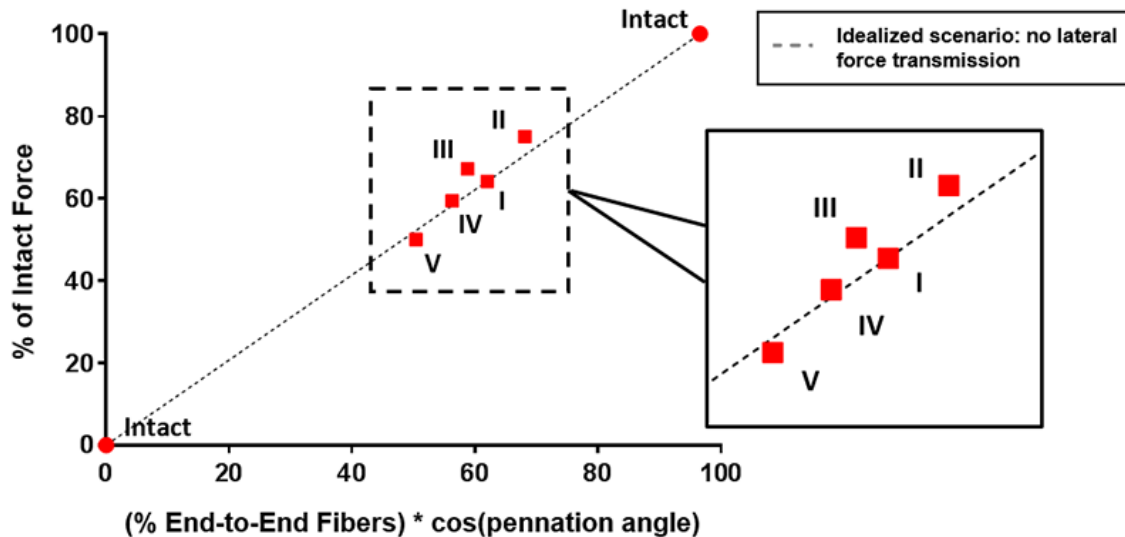


Figure 2-7. The relationship between lateral and longitudinal force transmission is affected by the percent of injured/end-to-end fibers. On the x-axis, the percent of end-to-end fibers is multiplied by the cosine of average pennation angle to account for the varying angle of end-to-end fibers in each injury model and allow for direct comparison between models. Each injury cuts different fibers thus altering the average pennation angle and force transmission. The dotted line represents an idealized scenario of no lateral force transmission where the percent of end-to-end fibers directly correlates to force production. Models II and III are above the line indicating that lateral force transmission is contributing to the total force. However, Model V is below the line and lateral force transmission appears to be impairing force production.

The effects of injury location on force production can further be explained by exploring local variability of fiber lengths along the length of the muscle using the model. The along-fiber stretch, which is fiber length relative to the original optimal fiber length, distributions of Models I and V demonstrate the non-uniformity of fiber length within the LD. The local length variation along the LD is consistent with other studies that have demonstrated that myofiber length varies substantially across entire muscles [74,75]. When the fiber length is measured near the LD's attachment, which is where the force is measured *in situ*, Model V has a larger percent of non-end-to-end fibers operating at a shorter along-fiber stretch than Model I. This larger percentage of shorter fiber lengths likely accounts for the lower force production of Model V compared to Model I.

The demonstrated ability of the LD FE model to accurately predict experimental results and quantify biomechanical mechanisms provides motivation for additional studies using the model as a predictive tool prior to testing of VML injuries *in vivo*. The model can be utilized to explore the relationship between injury size and force deficits, and furthermore, expanded to include the long-term response of VML injuries by incorporating a passive material to represent the filling of the defect with connective tissue or an active material to simulate the regenerative response of a therapeutic. Additionally, the model can be used to identify the preferred experimental injury location in a given muscle to increase the margin of difference between the isometric force produced in intact and VML injured muscles — thus producing more favorable conditions for evaluating treatment effects. Analytic capabilities provided by the model have the potential to significantly increase mechanistic insight, and thus, better inform preclinical

experimental design, such as designing a novel therapeutic approach based on the biomechanical requirements of the injury environment.

In conclusion, this work demonstrates that the use of both FE models and *in situ* functional testing of VML injuries provides critical insight into the biomechanical mechanisms governing the relationship between VML injury location and force production/deficit. Combining the tools of the computational modeling and tissue engineering fields should accelerate the development of more efficacious regenerative therapies, and thus, ensure improved functional outcomes following even the most debilitating VML injuries.

Chapter 3

Agent-based model provides insight into the mechanisms behind failed regeneration following volumetric muscle loss injury

Acknowledgements: Advanced Research Computing Services, Shayn M. Peirce, George J. Christ, Silvia S. Blemker

“I can be flexible, as long as everything is exactly the way I want it.” – Lorelai

Gilmore Girls

3.1 Abstract

Skeletal muscle possesses a remarkable capacity for repair and regeneration following a variety of injuries. When successful, this highly orchestrated regenerative process requires the contribution of several muscle resident cell populations including satellite stem cells (SSCs), fibroblasts, macrophages and vascular cells. However, volumetric muscle loss injuries (VML) involve simultaneous destruction of multiple tissue components (e.g., as a result of battlefield injuries or vehicular accidents) and are so extensive that they exceed the intrinsic capability for scarless wound healing and result in permanent cosmetic and functional deficits. In this scenario, the regenerative process fails and is dominated by an unproductive inflammatory response and accompanying fibrosis. The failure of current regenerative therapeutics to completely restore functional muscle tissue is not surprising considering the incomplete understanding of the cellular mechanisms that drive the regeneration response in the setting of VML injury. To begin to address this profound knowledge gap, we developed an agent-based model to predict the tissue remodeling response following surgical creation of a VML injury. Once the model was able to recapitulate key aspects of the tissue remodeling response in the absence of repair, we validated the model by simulating the tissue remodeling response to VML injury following implantation of either a decellularized extracellular matrix scaffold or a minced muscle graft. The model suggested that the pro-inflammatory cells and fibroblasts, as well as the SSC microenvironment and absence of pro-differentiation SSC signals, impaired the regeneration of new muscle fibers within the VML defect. The major implication of this work is that agent-based models may provide a much-needed predictive tool to optimize the design of

new therapies, and thereby, accelerate the clinical translation of regenerative therapeutics for VML injuries.

3.2 Introduction

In response to common injuries, such as lacerations or strains, skeletal muscle repair occurs through a well described process governed by temporally-regulated, highly orchestrated, multicellular interactions [18,19]. However, in the setting of volumetric muscle loss (VML) injuries, which are characterized by the simultaneous loss of multiple tissue compartments (i.e., muscle, vessel, nerve and extracellular matrix (ECM)), the intrinsic regenerative process fails, resulting in permanent cosmetic and functional deficits. VML typically results from trauma, such as battlefield injuries to wounded warriors, or civilian vehicular accidents and there are no current treatment options for complete restoration of form and function. In this scenario, the lack of insight into the mechanisms responsible for the failure of functional regeneration, in the context of VML injury, represents a major barrier to development of novel therapeutics for improved functional outcomes.

Successful muscle tissue repair in response to lacerations or strain injuries generally occurs within 28 days and involves 3 well documented phases [20–22]. An initial inflammatory response coordinated by an infiltration of neutrophils and pro-inflammatory (M1) macrophages to clear debris. The second phase, repair, follows with fibroblast and satellite stem cell (SSC) activation and proliferation. Within 7 days post injury, macrophages switch to an anti-inflammatory (M2) phenotype and fibroblasts and SSCs numbers peak. After 14 days, the remodeling (third) phase begins and fibroblasts undergo apoptosis and SSCs differentiate and

fuse to repair existing myofibers. In contrast, the repair process of skeletal muscle after VML injury is dominated by an inflammatory and fibrotic response [10,12,13], resulting in permanent loss of muscle volume, replacement of muscle with scar tissue, and resulting functional impairments (Figure 3-1). Following VML injuries, pro-inflammatory pathways remain upregulated for four weeks, as opposed to one week in successful muscle repair [11]. SSCs fail

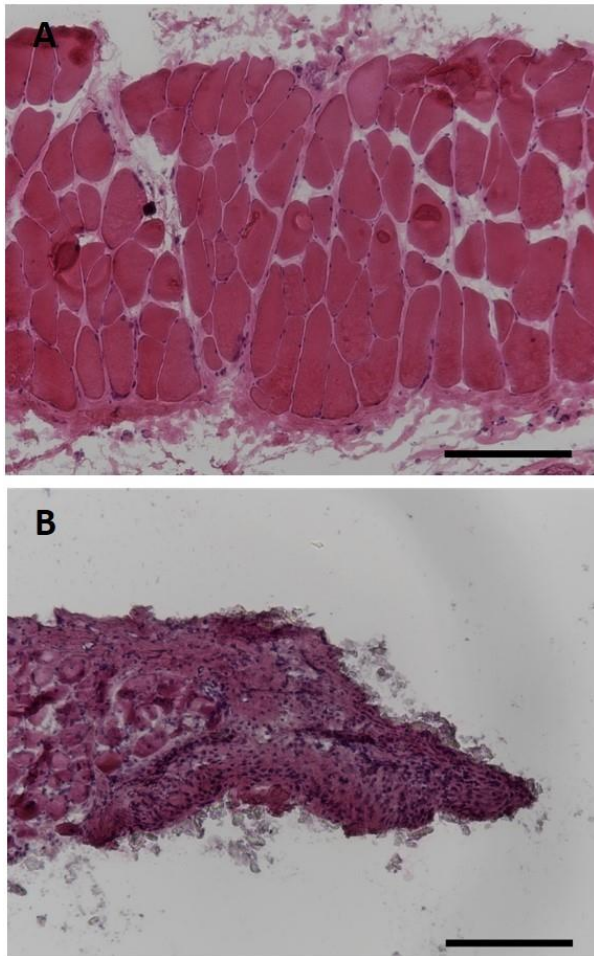


Figure 3-1. Histology of hematoxylin and eosin-stained rat latissimus dorsi skeletal muscle shows the cross-section of healthy muscle (A) and the cross-section 7 days after VML injury (B). The lack of muscle fibers on the right half of the image marks the defect caused by the VML injury. Scale bars = 200 μm .

to differentiate and fibroblasts and myofibroblasts fill the defect space with fibrotic tissue, which includes densely packed collagen [4,11,23].

In short, VML injuries require therapeutic intervention for complete functional regeneration. Both preclinical studies [3,4,6], as well as limited initial clinical trials [76,77], clearly indicate there is a need for improved therapeutic design. Strategies evaluated thus far have included implantation of decellularized ECM, minced muscle grafts (MMGs), as well as a variety of natural and synthetic biomaterials seeded with muscle progenitor cells and/or a combination of growth factors to help promote SSC proliferation and differentiation [3,4,6,7,15,78,79]. The results have been

variable, but inclusion of cells with decellularized ECM at the time of implantation has generally shown greater promise in functional restoration of muscle tissue after VML injury than implantation of decellularized ECM alone [3,6–8]. Despite rapidly increasing preclinical activity, important questions remain about which early cellular processes are required to more effectively drive the VML injury response. For example, will modulating the early inflammatory response or mitigating fibrotic pathways in VML injuries, or both, improve muscle regeneration and functional outcomes? A better understanding of these mechanisms is a prerequisite to the design of more efficacious regenerative therapeutics for VML repair [10,11,80–84].

Experimental identification and validation of the critical cellular mechanisms and microenvironmental conditions associated with the tissue healing response to VML injury is a resource-intensive and time-consuming process. The deployment of agent-based models (ABMs) in parallel with experiments provides a powerful way to synthesize and integrate data in order to systematically predict, in a more rational and cost-effective manner, how cellular mechanisms of interest impact tissue repair/remodeling and optimally affect regeneration [85]. ABMs simulate cellular behaviors and show the effects of these cellular behaviors on the physiological system as a whole. Agents represent individual cells within a tissue as well as environmental components, such as ECM, and the computational platform synthesizes the published work in the field, as agent behaviors are governed by literature-derived rules [86]. Our group has previously developed an ABM of muscle regeneration that was focused on the role of inflammatory cells following laceration injury [61]. We subsequently modified this model to study how different Duchenne muscular dystrophy mechanisms influence muscle

regeneration [62]. In this study, we are expanding the use of ABMs to study the cellular responses following VML injury.

The goal of this work was to develop an ABM of muscle regeneration in the setting of VML injury that focused on the dynamics of fibroblasts and SSCs in order to better understand the critical cellular mechanisms responsible for regeneration. We first used the ABM to predict the tissue healing response in an unrepaired VML injury, and then we tuned the model to replicate important cell population dynamics from published experimental studies. The ABM was validated by simulating VML injury and tissue healing/repair following implantation of either an acellular biomaterial (decellularized ECM) or another therapeutic that included a cellular component (MMG). In both cases the model simulations were compared to published experimental data. Lastly, in order to identify new strategies for muscle regeneration following VML, we evaluated the impact of perturbation of parameters and combinations of parameters of interest, all of which had defined cell behaviors known to be important in muscle regeneration.

3.3 Methods

3.3.1 ABM design

We created an ABM of skeletal muscle regeneration following VML injury (Figure 3-2). To develop our model, we used over 100 published experimental studies to define 80 rules that govern the behaviors of fibroblasts, SSCs, inflammatory cells, and skeletal muscle. The ABM represented a two-dimensional cross-section of a rat skeletal muscle consisting of 164 muscle

fibers. The agents that occupied space in the model included muscle fibers, ECM, necrotic muscle tissue, fibroblasts, myofibroblasts, quiescent and activated SSCs, myoblasts, myocytes, and myotubes. Model components whose spatial location was not tracked included eleven growth factors and three types of inflammatory cells: neutrophils, proinflammatory (M1) macrophages, anti-inflammatory (M2) macrophages. We built the ABM in Repast, a java-based modeling platform (Argonne National Laboratory) and the ABM's code is available for download (<https://simtk.org/projects/abm-vml>).

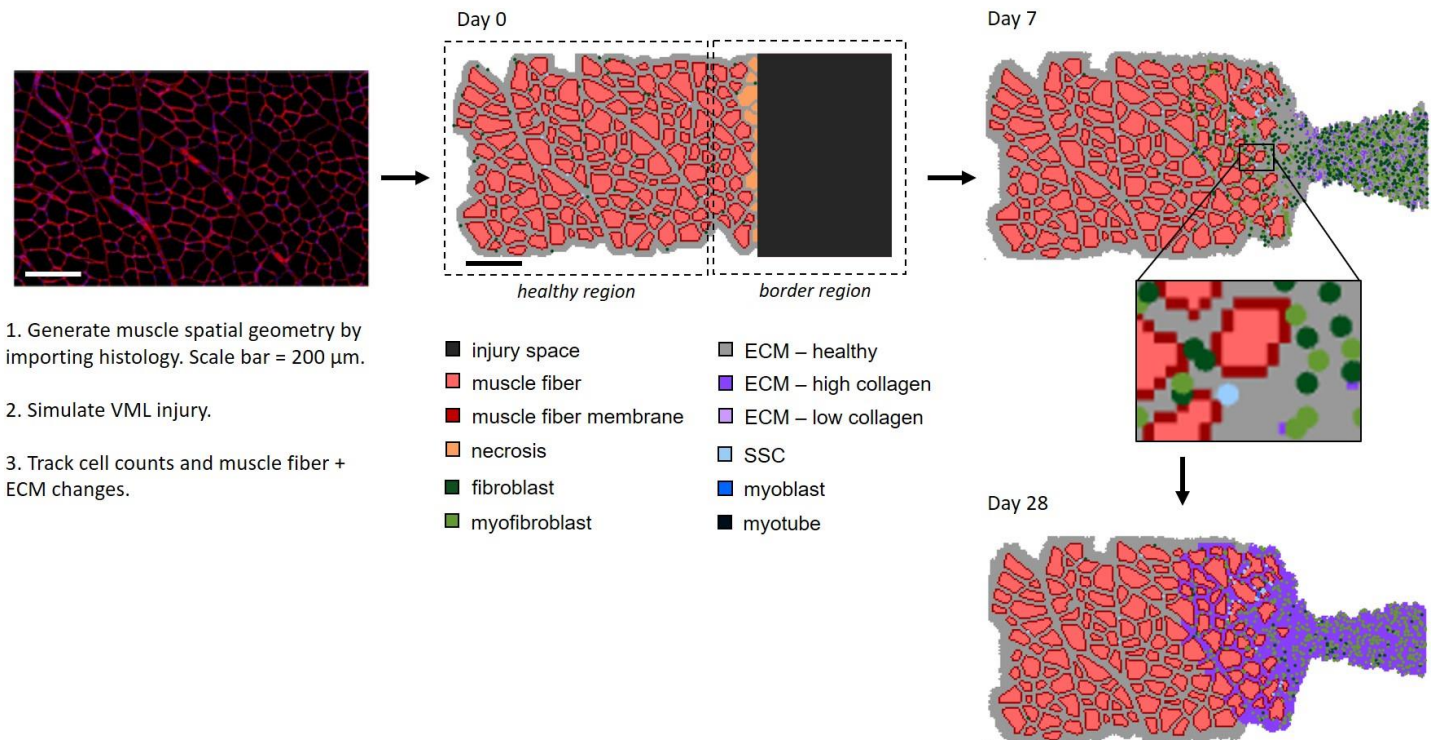


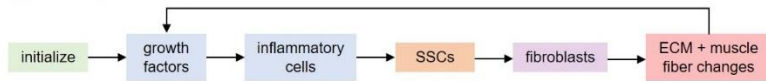
Figure 3-2. ABM simulates muscle regeneration for 28 days following VML injury. The spatial geometry of the ABM was defined by importing a histological image [11]. Then a VML injury was simulated by removing 12 fibers and creating an injury space and replacing severed fibers at the edge of the injury and native muscle with necrotic elements. The ABM consisted of two regions – the healthy region of muscle fibers near the injury that were not affected by the defect and the border region consisted of fibers near the injury and the injury space. Regeneration was followed over time by tracking cell counts, muscle fiber counts, and collagen density in each region.

Overall, the ABM was a two-dimensional grid of over 30,000 pixels including the muscle fibers and injury area ($1.59 \times 0.74 \text{ mm}^2$). The muscle cross-section geometries in the ABM were generated by importing a micrograph of a histological section of muscle ($1.3 \times 0.74 \text{ mm}^2$, $10 \mu\text{m}$ thick) with 188 fibers [11,87]. The image was first processed in MATLAB (Mathworks) to generate a file consisting of each pixel labeled as fiber, fiber border, or ECM. This labeled file was then imported into the ABM grid. The VML injury was created at the start of the simulation by removing 12 imported muscle fibers on the right edge of image and adding pixels to create the injury defect. Fibers that were severed by the creation of the injury were automatically replaced with necrotic agents. After injury and initial necrosis, the muscle area was $1.1 \times 0.74 \text{ mm}^2$ (164 fibers) and the injury area was $0.49 \times 0.74 \text{ mm}^2$. The injury area is larger than the area of the cut fibers to ensure that the ratio of remaining muscle area to injury space was comparable with the experimental studies we used to tune our model (approximately 20% VML injury) [11,88]. Simulations were run with a 1-hour time step for a simulated 28 days following injury to capture the timeframe of typical muscle repair [20–22]. All simulations were repeated 10 times to capture the stochastic cell behaviors of the model. The key model outputs included the time-varying counts for each cell type in the model and the number of muscle fibers.

In VML injuries, the spatial relationship between cells relative to the VML defect location affects their responses during the regeneration process; therefore, the ABM consisted of a healthy muscle region and a border region that was adjacent to the defect. The healthy region consisted of the muscle fibers near the VML injury that were not affected by the defect, approximately $130 \mu\text{m}$ from the injury space [89]. The border region consisted of the fibers within $130 \mu\text{m}$ of the injury and the injury space [4,78,89]. This ABM spatial representation and

the baseline number of cells (e.g. fibroblast, SSC) were defined when the ABM was initialized. At each time step of the simulation, every cellular agent (e.g. fibroblast, SSC) determined its location in the simulation space and then its behaviors were determined by a probability-based decision tree (Figure 3-3. Flowchart depicts the ABM rules, logic flow, and agent actions. After initialization, the growth factors and inflammatory cells are calculated during each subsequent time step. Then SSCs, fibroblasts, fibers, and ECM follow a probability-based decision tree to guide their actions.). For example, an SSC agent near the injury in the border region had a chance of proliferation that was proportional to the magnitude of the border region proliferation signal. The collective actions of all the autonomous agents (fibroblasts, SSCs, ECM, muscle fibers, and growth factors) lead to emergent, system-level behaviors (fiber counts, cell population dynamics) that were output by the simulations.

High level ABM overview:



ABM subroutines:

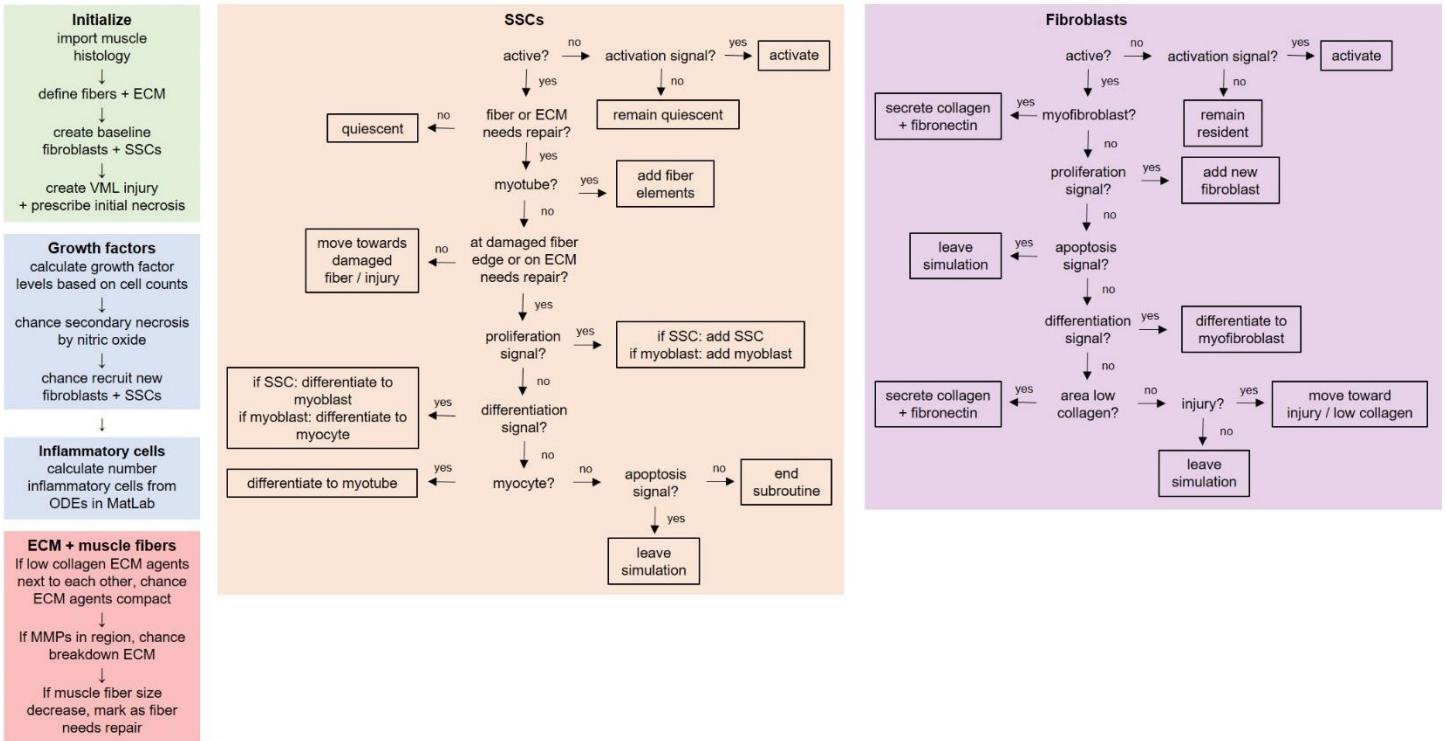


Figure 3-3. Flowchart depicts the ABM rules, logic flow, and agent actions. After initialization, the growth factors and inflammatory cells are calculated during each subsequent time step. Then SSCs, fibroblasts, fibers, and ECM follow a probability-based decision tree to guide their actions.

3.3.1.1 Agent actions

The simulated behaviors of fibroblast and SSC agents included secretion of growth factors, quiescence, activation, recruitment, migration, proliferation, differentiation, and apoptosis. To simulate migration, the agents were programmed to move to a neighboring pixel based on experimentally derived migration rates (Table 3-1, Table 3-2). Quiescent agents did not migrate or secrete growth factors until they were activated by growth factors. If an agent was recruited to the injury, then a new agent was added to the simulation. An active agent

could undergo migration, secretion of growth factors, proliferation, differentiation, and apoptosis. Agent proliferation was represented by adding an additional agent to the simulation next to the proliferating agent. There is no rule directly preventing cell overlap in the simulation but the chances of a fibroblast and SSC agent overlapping is very low because the preferred location of a SSC agent is on a fiber border agent and the preferred location of a fibroblast agent is on an ECM agent. Agent differentiation was represented by changing the agent type to the differentiated state (rules that govern differentiation behaviors and states are defined in the fibroblast and SSC agents subsections). If an agent underwent apoptosis, it was removed from the simulation. Agent behavior was influenced by behavior signals that were defined by a function of factors that are known to promote or suppress each behavior (Eq. 1). The cell behavior signal was then normalized by a factor accounting for the size of the ABM grid and the probability of a cell behavior occurring was weighted by this behavior signal (Eq. 2) [61,62].

$$\text{cell behavior signal} = \sum \text{factors promote} - \sum \text{factors suppress} \quad (1)$$

$$\text{cell behavior probability} = \frac{1}{\text{normalization factor} - \text{cell behavior signal}} \quad (2)$$

3.3.1.2 Fibroblast agents

During model initialization, the fibroblast agents were distributed randomly throughout the ECM at a density of 1 fibroblast per every 3 fibers for a 10 μm thick cross-section [90–92]. After VML injury, additional fibroblast agents were recruited at a rate that was proportional to the amount of IL-4 secreted by eosinophils [10,27]. Fibroblasts migrated to the injury site at a rate of 44 $\mu\text{m}/\text{h}$ and had a preference to move to low collagen ECM agents [10,90,93]. The growth factor myostatin promoted proliferation of fibroblast agents [28–30], and high levels of

TGF- β promoted an increased likelihood of fibroblast agents differentiating to myofibroblasts [10,11,13,31]. The likelihood of fibroblast apoptosis was elevated by the presence of TNF- α , whereas TGF- β blocked apoptosis [11,94]. There is experimental evidence that fibroblast counts decrease after injury, and studies have shown that this is partially a result of differentiation to adipocytes but the mechanism is not clear [36,94,95]. We incorporated a fibroblast removal rule to capture this behavior and the likelihood of fibroblast removal in the simulation was tuned to capture the experimental data of declining fibroblast counts after injury (ABM parameterization subsection, Figure 3-4A). Fibroblast and myofibroblast agents secreted growth factors and collagen following injury (Table 3-1). Experimental studies have shown that fibroblast secretion of collagen is dependent on the magnitude and frequency of stretch it experiences; therefore, we incorporated a fibroblast collagen-stretch dependency in the model defined by experimental results [96]. This collagen-stretch dependency parameter can be set at the start of the simulation and adjusts the fibroblast collagen secretion accordingly. For this work, we have assumed that we are simulating normal rat movement of intermittent stretching, 12 hours of rest and 12 hours of active time, and the fibroblasts secrete normal levels of collagen. If the fibroblast or myofibroblast agent was greater than 200 μm from healthy muscle, then the agent became hypoxic and the collagen secretion and migration speed decreased [97–99]. Other effects of hypoxia, such as the release of apoptotic factors, were not included in the model for the mechanisms of fibroblast count decrease after injury are not clear, as mentioned above, and our goal was to focus on the growth factors secreted after injury.

Table 3-1. Fibroblast agent behaviors were defined by literature derived rules

<i>Fibroblast Agent Behavior</i>	<i>References</i>
Initial count: 1 per every 3 fibers	[90–92]
Recruitment signal: eosinophil recruited IL-4	[10,27]
Migrate toward injury/low collagen at rate of ~44 $\mu\text{m}/\text{h}$	[10,90,93]
Proliferation signal: myostatin from damaged ECM	[28–30]
Differentiation signal: TGF- β	[10,11,13,31]
Apoptosis signal: TNF- α If sustained high levels of TGF- β , then blocked apoptosis	[11,94]
Generalized decrease (removal) of fibroblast following injury, e.g. adipogenic differentiation	[36,94,95]
Secretions: TGF- β , IGF, IL-6, FGF, MMPs	[32–38]
Secrete collagen + fibronectin to rebuild ECM and fill injury space	[38,39]
Myofibroblast secrete more collagen than fibroblasts and TGF- β , MMPs	[3,11,13,31,100]
If > 200 μm from healthy muscle, then fibroblasts and myofibroblasts decrease collagen secretion + migration speed	[97–99]

3.3.1.3 SSC agents

During initialization, the SSC agents were randomly located at a muscle fiber edge in a quiescent state at a density of 1 SSC per 23.5 muscle fibers for a 10 μm thick cross-section [90,101]. Following VML injury, SSC agents became activated by ECM damage and the presence of hepatocyte growth factor [40–43]. Recruitment of SSC agents to the injury site was based on a recruitment signal of growth factors (Table 3-2). Migration of activated SSCs toward the injury site occurred at a rate of 50 $\mu\text{m}/\text{h}$ [4,78,102,103]. SSC agents proliferated based on the microenvironmental cues and growth factors outlined in Table 3-2. If there was sustained upregulation of the inflammatory response, then SSC proliferation was attenuated [90]. Terminal differentiation of SSC agents was based on a differentiation signal and microenvironmental cues (Table 3-2). To simulate regeneration, differentiated myotubes could add muscle fiber agents to the periphery of an injured fiber or deposit fiber agents to generate

a new fiber depending on its location [48–50]. Approximately 10% of the SSC population was instructed not to undergo differentiation, and helped to restore the SSC agent pool [51–53].

Table 3-2. SSC agent behaviors were defined by literature rules

<i>SSC Agent Behavior</i>	<i>References</i>
Initial count: 1 per every 23.5 fibers	[90,101]
Activation signal: HGF, released from ECM after injury	[40–43]
Recruitment signal: HGF + IGF + FGF + MMP – 2*TGF- β	[44–47]
Migrate to injury site at ~50 $\mu\text{m}/\text{h}$	[4,78,102,103]
Migrate if MMP degrade ECM	[46,104]
Microenvironmental cues for proliferation + differentiation: on fiber edge, on ECM with stiffness similar to healthy muscle	[105–108]
Proliferation signal: 3*IGF + 3*FGF + HGF + TNF- α + IL-6 + IFN γ – IL-10 – 4*TGF- β	[13,42,43,109–111]
Proliferation attenuated by sustained upregulation of inflammatory response	[90]
Differentiation signal: 4*IL-10 – 2*FGF – 2*IGF – 2*HGF – IFN γ – TNF α	[45,110,112,113]
10% of SSCs do not express Myf5 and will not differentiate	[51–53]
Activated SSCs differentiate to myoblasts, myoblasts to myocytes, and myocytes to myotubes	[41,114,115]
Myotubes put down muscle protein to repair existing fiber or put down new fiber	[48–50]
Apoptosis signal: TGF- β	[116]
Secretions: IL-6, MMPs, IL-1	[117,118]

3.3.1.4 ECM and muscle fiber agents

At initialization, a single muscle fiber was represented by an average of 72 pixels.

Muscle fiber agents were removed along the edge of the ABM grid to represent VML injury, and the fibers which were cut were replaced by necrotic agents. During the simulation, secondary necrosis spread based on nitric oxide levels secreted by inflammatory cells [19,26]. The rate of necrosis agent removal was dependent on the number of M1 macrophage agents [13,26].

Agents representing cleared necrosis were converted to a low-density collagen ECM agent.

Fibroblast agents secreted collagen in low collagen areas and in the injury space [26,39]. If

areas of very low collagen remained, then two neighboring ECM agents with low collagen had a probability of merging into a single agent. This simulated behavior reduced the thickness of the muscle cross-section near, and within, the injury site, which has been observed experimentally [6]. Areas of high-density collagen ECM agents corresponded to fibrotic tissue [4,16]. When differentiated myotubes were fused to a fiber edge that had been damaged through necrosis, muscle fiber agents were added at the periphery of the fiber to increase the muscle fiber size. If the myotubes were on an ECM agent with healthy levels of collagen (defined as a model specific range), then there was a chance of putting down a fiber agent to generate new muscle fibers. For ECM agents, a healthy level of collagen was defined to be a range of model-specific values that corresponded with temporal observations of low fibrosis levels in experimental histology [4,6,79]. Given the parameters in our model, we assumed that ECM levels of collagen correlated to muscle stiffness and thus this microenvironmental rule captured the SSCs dependency on healthy muscle stiffness to proliferate and differentiate [105,106,108].

3.3.1.5 Growth factors

The 11 growth factors in the model (Table 3-1, Table 3-2) were varied from baseline levels (before injury) to levels following VML injury. Growth factors were tracked in each region of the model, healthy versus border regions, and added at each time step based on the defined secretions for each cell type in their respective region. The amount of growth factors within each region were tracked over time. We have assumed that the growth factors are evenly distributed in each region, they do not diffuse or move within the region, and they decay over

time at a fixed half-life of 5 hours that represents the growth factors diffusing out of the tissue [20,119–122].

3.3.1.6 Inflammatory cell ordinary differential equations

The inflammatory cell dynamics were defined based on previous work by Martin et al. and Virgilio et al. [61,62]. Our goal was to incorporate the dynamic behaviors of inflammatory cells but also reduce the computational cost of the ABM. The inflammatory cells were represented as a system of three coupled ordinary differential equations (ODEs) for neutrophils, M1, and M2 macrophages. The ODEs were defined by 20 parameters that represent the effect of one cell type on another cell. A genetic algorithm (GA) was used to parameterize the ODEs by minimizing the difference between ABM macrophage populations predicted by the model and experimentally measured macrophage dynamics after VML injury [78,82]. Each generation had 500 individuals with 20 variables. The GA objective function [Eq. 1] was a sum of squared differences between simulation results (subscript ABM) and experimental data (subscript EXP) (Eq. 3).

$$\text{Objective Function} = \sum_{t=1}^{672} (N_{\text{ABM}} - N_{\text{EXP}})^2 + \sum_{t=1}^{672} (M1_{\text{ABM}} - M1_{\text{EXP}})^2 + \sum_{t=1}^{672} (M2_{\text{ABM}} - M2_{\text{EXP}})^2 \quad (3)$$

To compare our hourly model predictions with the discrete experimental observations, we fit the experimental macrophage population dynamics with a fourth order polynomial equation (MATLAB). Each comparison was weighted by the variance of the experimental data. Variance for fitted time points was determined using a linear interpolation between experimental time points. We used a MATLAB GA solver (GA) where GA individuals that had the lowest objective

function scores were used as parents for the next generation of individuals (20% offspring, 80% new random individuals). The GA was designed to stop if the objective function failed to decrease 1×10^{-9} for 50 consecutive generations, with a limit of 1000 generations.

Within the ABM simulation framework, the inflammatory cell ODEs were solved for each region (healthy and border) by calling the MATLAB engine and using a MATLAB non-stiff differential equation solver, ode45. The regional breakdown of inflammatory cells was approximated to be 60% in the border region and 40% in the healthy region [78]. Perturbations varying the distribution of macrophages in each region are included in Appendix A. To couple the inflammatory cell ODEs with the behaviors of the other spatial cell agents, the inflammatory cell agents had defined rules based on cell counts at the beginning of each time step. The inflammatory cells secreted growth factors and removed necrosis agents, and their ODEs were dependent on the spatial cell agent counts at each time-step. Inflammatory cell ODEs (Eq. 4-6) include the following, where $\%_{\text{necrosis}}$ is the current ratio of muscle that is necrotic, Fb is the current number of fibroblast agents, and SSC is the current number of SSC agents:

$$\frac{dN}{dt} = 52.08 * \%_{\text{necrosis}} - 0.0021 * \text{Fb} - 0.28 * N - 0.0023 * M1 - 0.012 * M2 - 0.0022 * \text{SSC} + 0.065 * N * \%_{\text{necrosis}} \quad (4)$$

$$\frac{dM1}{dt} = 2.24 * \%_{\text{necrosis}} + 0.21 * \text{Fb} + 0.05 * N - 1.03 * M1 - 0.42 * M2 + 23.31 * \text{SSC} + 0.03 * M1 * \%_{\text{necrosis}} \quad (5)$$

$$\frac{dM2}{dt} = 126.73 * \%_{\text{necrosis}} + 1.91 * \text{Fb} + 0.07 * N - 0.74 * M1 - 9.07 * M2 + 7.96 * \text{SSC} \quad (6)$$

3.3.2 ABM parameterization

To parameterize the baseline (no repair) model of VML injury, we ran simulations and systematically adjusted the unknown model parameters manually (Table 3-3) until the model predictions (95% confidence intervals) were consistent with published experimental data, which included fibroblast (marked by *col3a1*) and SSC (marked by *Pax7*) fold changes [11] and inflammatory cell fold changes (inflammatory macrophages marked by *CCR7*, anti-inflammatory macrophages marked by *CD163*) [82]. *Tcf4+* is a fibroblast marker that has been reported to be specific to skeletal muscle [91]; however, there were no VML studies that have quantified expression of this marker. Thus, we fit our fibroblast and myofibroblast fold changes to the observed changes in gene expression of *col3a1* (collagen 3) following VML injury [11] and it has been used as a marker of fibroblasts in other tissues [123–125].

Model predicted cell counts were normalized by the number of cells at initialization to calculate the fold change and allow for direct comparison with values reported in experimental studies. When comparing the ABM predicted cell counts with published experiments, we focused on 7 to 14 days post injury because this is when the counts peak according to the literature [11,82].

Table 3-3. Unknown model probability parameters were tuned to recapitulate published experimental results

<i>Probability Parameter</i>	<i>Equation</i>	<i>Range Tested</i>	<i>Value</i>
Maximum probability of fibroblast recruitment per hour, x_1	If fibroblast recruitment probability $> x_1$, recruitment probability = x_1	0.0200 – 0.2000	0.0333
Maximum probability of fibroblast proliferation per hour, x_2	If fibroblast proliferation probability $> x_2$, proliferation probability = x_2	0.0200 – 0.5000	0.0286
Maximum probability of fibroblast differentiation per hour, x_3	If fibroblast differentiation probability $> x_3$, differentiation probability = x_3	0.0100 – 0.2000	0.0125
Maximum probability of fibroblast apoptosis per hour, x_4	If fibroblast apoptosis probability $> x_4$, differentiation probability = x_4	0.0100 – 0.2000	0.0125
Maximum probability of fibroblast removal per hour, x_5	If fibroblast removal probability $> x_5$, removal probability = x_5	0.0200 – 0.2000	0.1000
Maximum probability of SSC recruitment per hour, x_6	If SSC recruitment probability $> x_6$, recruitment probability = x_6	0.0008 – 0.0400	0.0008
Maximum probability of SSC proliferation per hour, x_7	If SSC proliferation probability $> x_7$, proliferation probability = x_7	0.0100 – 0.5000	0.0400
Maximum probability of SSC differentiation per hour, x_8	If SSC differentiation probability $> x_8$, differentiation probability = x_8	0.0100 – 0.5000	0.0666
Maximum probability of SSC apoptosis per hour, x_9	If SSC apoptosis probability $> x_9$, apoptosis probability = x_9	0.0020 – 0.5000	0.0020
Probability of SSC creating new fiber on ECM with healthy levels of collagen, x_{10}	$1/x_{10}$	0.0100 – 0.0400	0.0200

3.3.3 Validation of ABM

Once the model parameters were tuned, we ran simulations to verify the model predictions and validate the ABM using data from the literature that was distinct from the data used for model calibration. We first simulated the administration of the anti-fibrotic agent, Losartan, to baseline (no repair) VML injuries [82]. Losartan was modeled by reducing TGF- β

secretion from myofibroblasts and macrophages by 60% [126]. We assumed TGF- β production was impaired by 60% for Losartan inhibits a receptor in the angiotensin pathway which thereby blocks TGF- β activation and signaling; however, there are other pathways involved in TGF- β production and signaling thus we chose to reduce but not eliminate TGF- β production [82,126]. We then simulated two VML treatments that have been experimentally tested [3,4,11,88]: implantation of either a decellularized ECM or a MMG at the site of injury. We simulated decellularized ECM by filling the injury space with ECM agents at initialization [3,4]. Perturbations varying the decellularized ECM structure are included in Appendix B. MMG consists of autologous muscle minced into 1 mm³ pieces, and it was modeled by filling the injury space with 38 muscle fibers. Twenty percent of the fiber agents were replaced by necrotic agents to represent fibers that were damaged during the mincing of fibers [3,11,88]. We assumed that the MMG fibers were parallel to the native muscle fibers for there was insufficient quantified literature data to make a more detailed assumption, and thus the MMG fiber cross sections were shown in the injury space. The model predictions were compared to the experimental results from the respective studies.

3.3.4 Analysis of regeneration mechanisms

3.3.4.1 Pro-inflammatory & fibrosis perturbations

There has been a recent shift in the overall strategy for treating VML injuries, with recognition that modulating the early inflammatory response(s), as well as impairing nonproductive fibrotic pathways are also critical to improved tissue healing—as opposed to

focusing solely on tissue engineering (i.e., replacing the lost tissue and cell populations) [10,80–82]. Thus, we utilized the ABM to predict the regenerative effects of modulating the pro-inflammatory and fibrotic cellular components of the tissue healing response, as well as altering the production of fibroblast-generated growth factors. We ran multiple “what-if” simulations to examine how each of the cellular behaviors in the ABM contributes to the tissue remodeling process. We individually varied the maximum number of proinflammatory macrophages, the maximum number of fibroblasts, and the secretion of fibroblast-secreted growth factors after VML injury by reducing them to 25%, 50% and 75% of baseline levels. We tracked the fibroblast and SSC counts over time, the number of new fibers, and the amount of fibrosis as indicated by collagen density to determine if these perturbations altered the ability of muscle fibers to regenerate following VML injury.

3.3.4.2 Combinatorial perturbations

After varying individual cellular behaviors, we then varied multiple parameters in a simulation to examine how the interplay between each of these behaviors leads to the tissue remodeling process.

In model perturbation A, we

- limited the number of M1 macrophages,
- limited the number of fibroblasts,
- and altered two key microenvironmental cues of SSCs (SSC location and ECM stiffness; see Table 3-2 for details) to increase the likelihood of regenerating fibers.

The maximum number of M1 macrophages and fibroblasts was reduced to 75% of baseline levels. In model perturbation A, we eliminated the rule of microenvironmental cues for SSC proliferation and differentiation (see Table 3-2 for details) so that SSC proliferation and differentiation was no longer limited to being on a fiber edge and the ECM collagen levels no longer affected the SSC behavior. In model perturbation B, we lowered the threshold of the SSC differentiation signal. By lowering the threshold below zero, we were able to explore the possibility that the absence of pro-differentiation signals was contributing to the failed regeneration. We tracked the fibroblast and SSC counts over time, the number of new fibers, and the amount of fibrosis as indicated by collagen density to determine if the combination of perturbations altered the ability of muscle fibers to regenerate following VML injury.

3.4 Results

3.4.1 ABM simulated regeneration dynamics of VML injuries without repair

After tuning the unknown model parameters, listed in Table 3-3, the simulations predicted emergent cellular behaviors which were consistent with the findings of experimental studies of VML injuries in the absence of therapeutic repair. Fibroblast and myofibroblast fold changes peaked at day 7 and then plateaued from day 14 onward (Figure 3-4A) [11], consistent with experimental observations of col3a1 gene expression fold changes following VML injury [11]. SSC counts also peaked at day 7 and then remained elevated through day 28 (Figure 3-4B), which is also consistent with experimental observations in the literature [11]. The inflammatory cell dynamics captured the data available, including the sustained upregulation of many

pathways associated with the inflammatory response [11,78,82] following VML injuries and the previously reported overwhelming inflammatory M1 macrophage response compared to anti-inflammatory M2 macrophages (Figure 3-4C) [78,82]. Muscle fiber and ECM changes, including the reduced thickness of the muscle cross-section near and within the injury site, were also consistent with published experimental studies. The ABM model for the baseline case of VML without repair predicted a complete failure in fiber regeneration and abundant collagen deposition in the injury defect (Figure 3-2) [4,78,79,88,89].

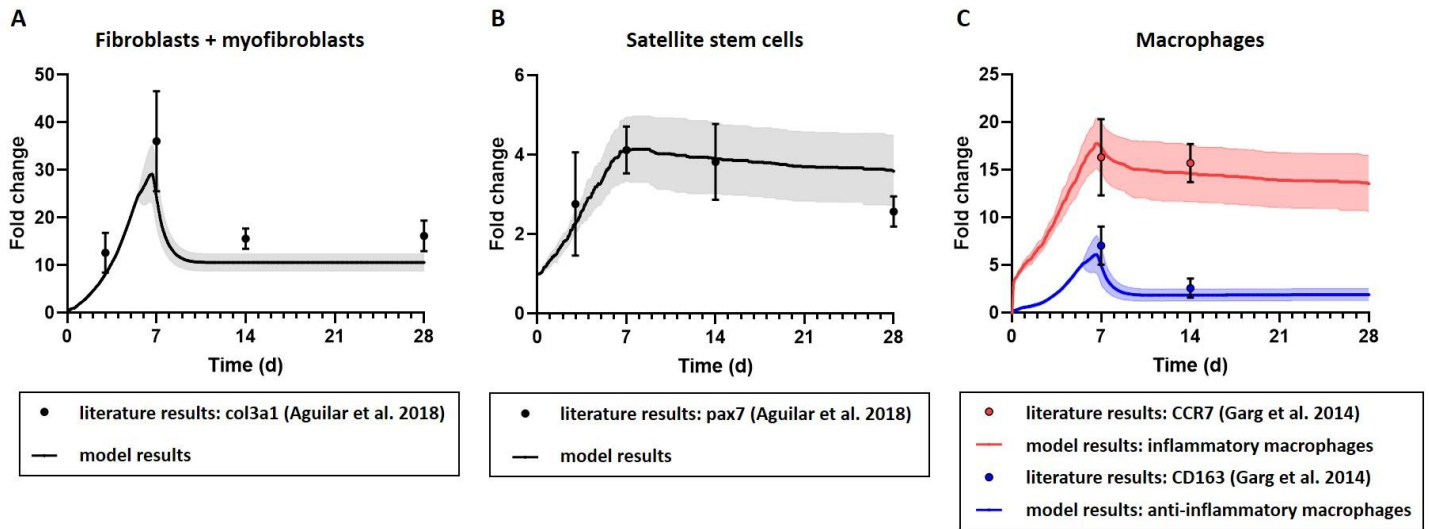


Figure 3-4. ABM of VML injury regeneration without repair parameterized to capture experimentally reported cell population behaviors. The model replicated an experimentally measured fold change in (A) the number of fibroblasts and myofibroblasts, (B) SSCs, and (C) M1 and M2 macrophages, within the model’s predicted 95% confidence interval. Model results were reported as mean \pm 95% confidence interval. Aguilar et al. 2018 experimental data of fibroblasts and satellite cells reported as median \pm standard deviation, and Garg et al. 2014 experimental data of macrophages reported as mean \pm standard error mean [11,82].

3.4.2 ABM validated by comparing simulations to independent experimental results of 3 different VML treatments

Treatment 1. First, ABM simulations were run for the tissue response to VML repair following administration of Losartan. Losartan is an anti-fibrotic therapy that inhibits angiotensin II type 1 receptor activation and thereby blocks TGF- β 1 [82]. Because our model does not specifically incorporate angiotensin II receptor blockade, we simulated the downstream effects of Losartan by reducing TGF- β production by myofibroblasts and macrophages 60% from baseline levels [126]. In this scenario, the ABM did not predict either the reduction in collagen III or the reduction in TGF- β fibrotic markers that has been observed experimentally following Losartan treatment 7 days after injury (Figure 3-5) [82]. However, consistent with experimental observations, the ABM predicted that Losartan treatment was associated with an increase in SSCs 14 days post-administration and injury. The ABM also predicted that by day 28 post injury, Losartan treatment causes collagen accumulation in the defect and no fiber regeneration, as has been reported in the literature [82].

Treatment 2. Next, we evaluated the ability of the ABM simulations to capture essential aspects of VML tissue repair following implantation of decellularized ECM. ABM simulations of decellularized ECM treatment following VML injury predicted an absence of new muscle fibers in the defect, indicating a lack of regeneration (Figure 3-5B), consistent with previously published experimental studies [3,4,6]. Further, the ABM predicted fibroblast, SSC, and M1 macrophage counts at day 28 post injury that were similar to those in VML injury simulations without repair (Figure 3-5A), and by day 28 the simulated defects contained increased collagen similar to VML injury simulations without repair (Figure 3-5B).

Treatment 3. Finally, model simulations of MMG treatment/implantation predicted similar fibroblast and SSC counts, accompanied by similar expression of fibrotic pathways, compared to VML injuries without repair at day 28 post injury, which is consistent with published experimental studies (Figure 3-5A) [3,11,88]. The ABM simulations of MMG treatment were also consistent with experimental observations in that both showed an increased number of muscle fibers by day 28 (Figure 3-5C) [3,11,88]. The model suggests that the new muscle fibers within the VML defect of MMG treated injuries resulted from the implanted muscle fibers within the MMG and were not generated by proliferation and differentiation of SSCs residing within the injured muscle [88]. The ability of our model to accurately predict repair using different treatments provides confidence in the utility of our model to capture tissue regeneration within VML injuries and points to some of the putative mechanisms underpinning experimental observations.

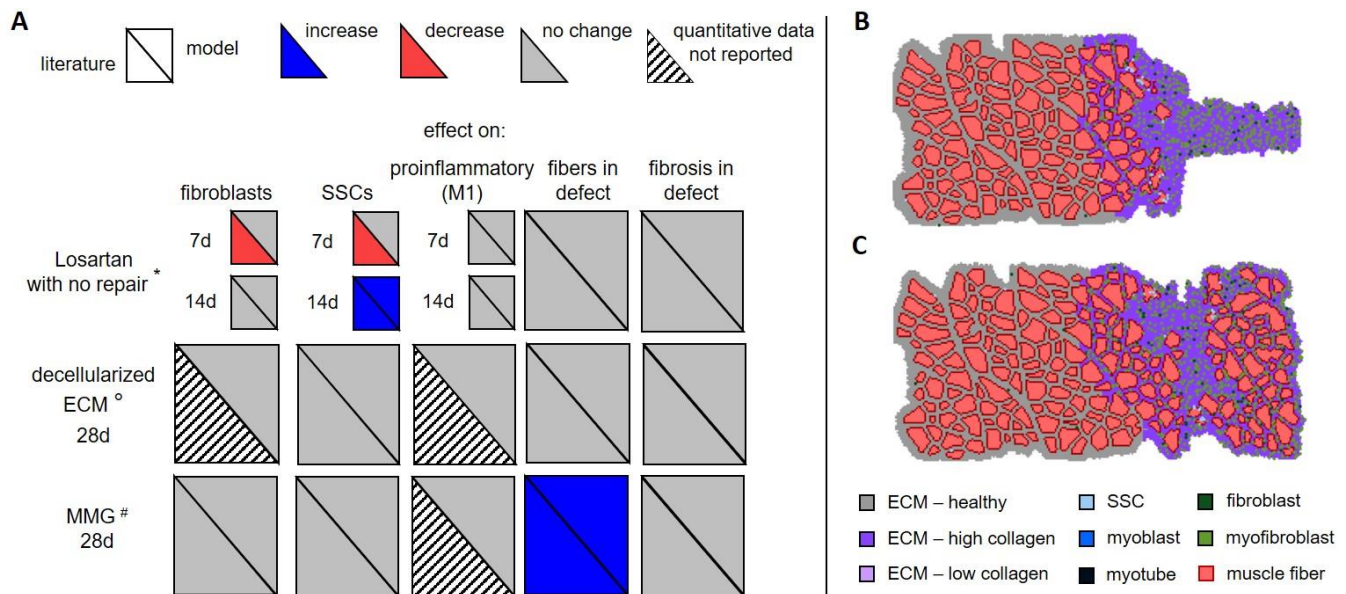


Figure 3-5. ABM predictions of cell behaviors, muscle fiber, and ECM changes 7, 14, and 28 days after injury and treatment were compared with published experimental results. Triangles represent an increase (blue), decrease (red), no change (grey), in response to the indicated treatment (i.e. Losartan with no repair, decellularized ECM, or MMG) or no quantified data available (striped) compared to VML injuries without repair (A). We compared quantitative changes in fibroblast, SSC, and pro-inflammatory macrophage numbers and compared qualitative changes in fibers and fibrosis in the VML defect. We also simulated VML injury treatments published in the literature and compared our model predictions to independent experimental results published in the literature: * [82], ° [3,4,6], # [3,11,88]. Graphical ABM outputs at 28 days showed that treating the VML injury with decellularized ECM resulted in fibrotic tissue (i.e. increased collagen) filling the defect (B) and minced muscle graft (MMG) treatment resulted in muscle fibers present in the defect (C).

3.4.3 ABM perturbations predict outcomes of potential VML treatments

3.4.3.1 Pro-inflammatory & fibrosis perturbations

Simulations reducing the number of pro-inflammatory macrophages did not affect cellular behavior nor the amount of fibrotic tissue relative to baseline simulations (Figure 3-6).

For example, while a 75% reduction in the number of M1 macrophages reduced their numbers to a level similar to M2 macrophages, that perturbation alone was not enough to alter the SSC differentiation signals and promote muscle regeneration. However, reducing the number of fibroblasts near the injury resulted in more SSCs and less collagen accumulation (Figure 3-7).

We simulated a reduction in the amount of fibroblast-generated growth factors (transforming growth factor beta, TGF- β ; fibroblast growth factor, FGF; insulin-like growth factor, IGF) and tracked the cellular counts and collagen density over 28 days (Figure 3-8). A 75% reduction of TGF- β compared to baseline levels resulted in higher SSC counts and lower collagen density (Figure 3-8A). In comparing the 75% reduction of TGF- β simulation to the Losartan simulation, both simulations resulted in higher SSC counts after 10 days post-injury; however, the 75% reduction of TGF- β resulted in zero fibroblasts and myofibroblasts by 14 days post-injury but the Losartan simulation continued to have similar fibroblast and myofibroblast cell counts as the no repair baseline simulation (Figure 3-5A, Figure 3-8A). This suggests that impairing fibroblast recruitment, and/or severely inhibiting TGF- β production following injury, may improve the ability of the muscle to repair following VML injury since there are more SSCs present and less fibrotic tissue, marked by lower collagen density, in the injury. Nonetheless, the ABM predicted no new fibers in the defect as a result of reducing TGF- β production nor reducing the other fibroblast-generated growth factors or cell populations (Figure 3-8), thus suggesting that in isolation this treatment approach would be insufficient to regenerate the muscle lost to VML injury.

Limiting number of M1 macrophages

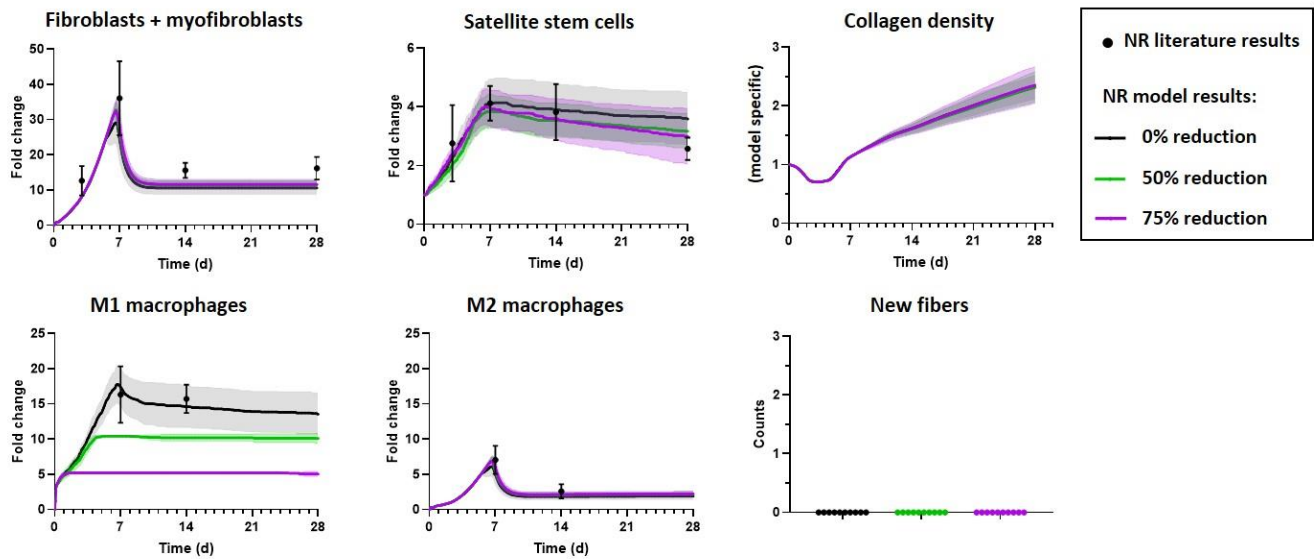


Figure 3-6. Limiting the number of M1 macrophages in the no repair (NR) ABM did not alter the amount of fibrosis as indicated by collagen density nor result in new muscle fibers filling the defect. The number of M1 macrophages was reduced to 50% and 75% of baseline levels. Outputs included fibroblast and myofibroblast fold changes, SSC fold changes, collagen density, macrophages fold changes, and number of new, regenerated fibers. Model results were reported as mean \pm 95% confidence interval. Aguilar et al. 2018 experimental data of fibroblasts and SSCs reported as median \pm standard deviation, and Garg et al. 2014 experimental data of M1 and M2 macrophages reported as mean \pm standard error mean [11,82].

Limiting number of fibroblasts

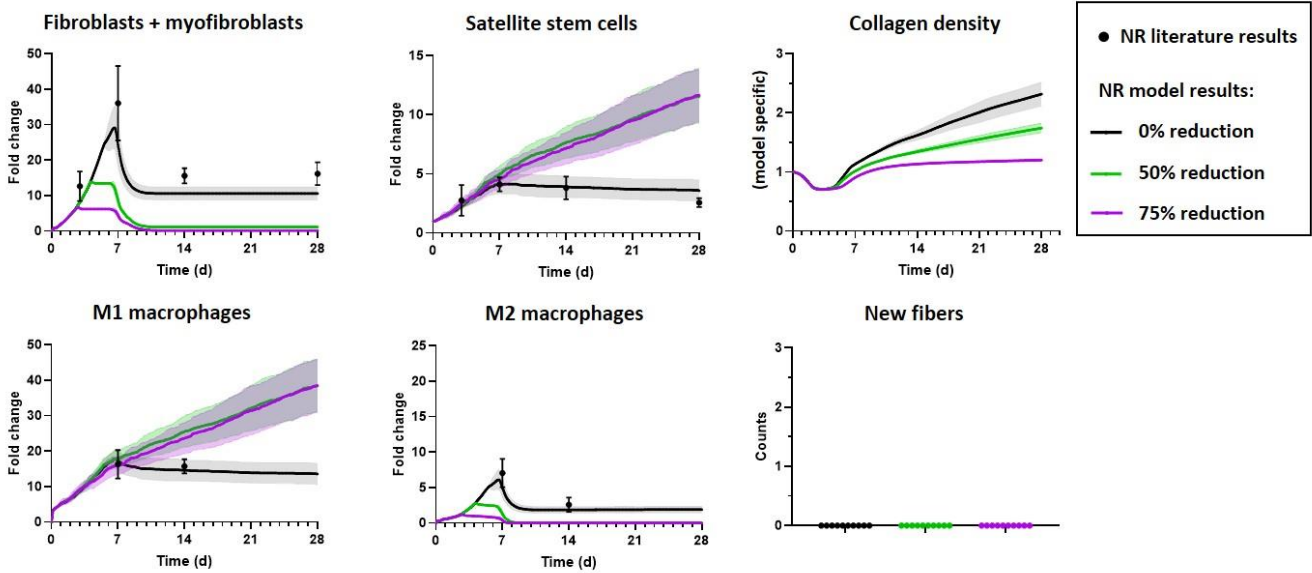
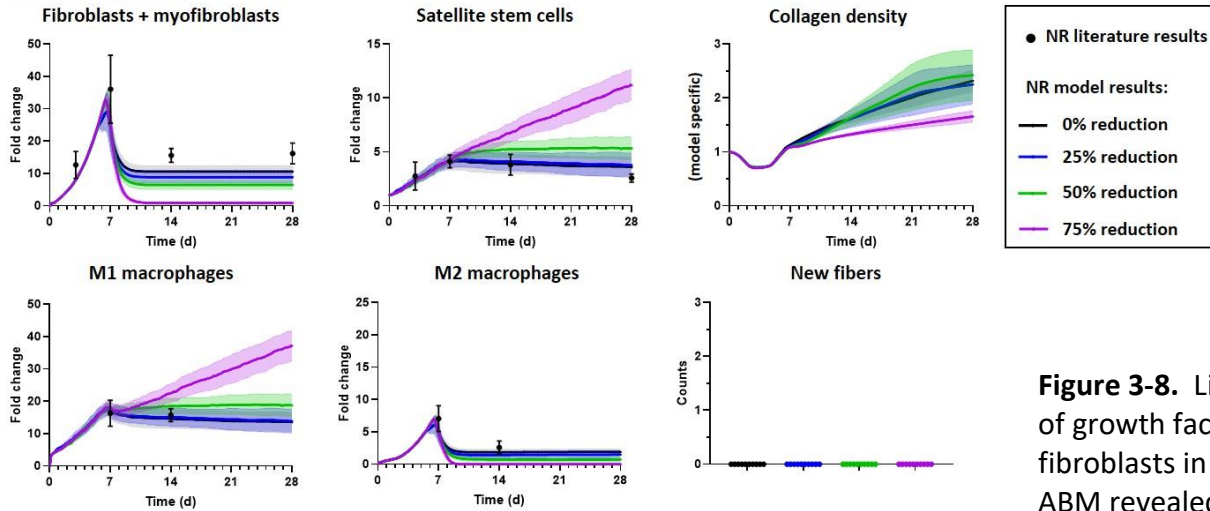
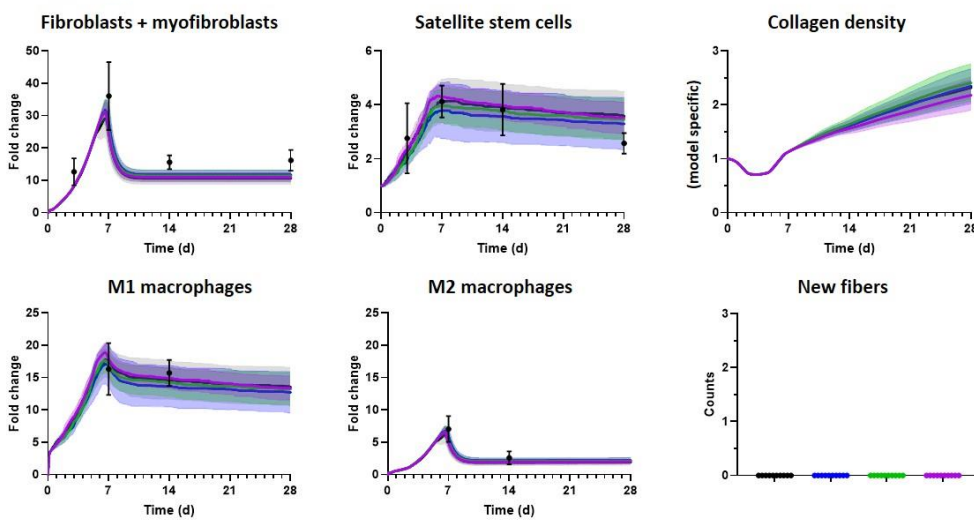


Figure 3-7. Limiting the number of fibroblasts in the no repair (NR) ABM reduced the number of fibroblasts and myofibroblasts following VML injury and altered the amount of fibrosis as indicated by collagen density. The number of fibroblasts was reduced to 50% and 75% of baseline levels. Outputs included fibroblast and myofibroblast fold changes, SSC fold changes, collagen density, macrophages fold changes, and numbers of new, regenerated fibers. Reducing the number of fibroblasts to 50% or 75% of baseline increased the number of SSCs and impaired the rate and extent of collagen accumulation in the defect. None of the perturbations to fibroblasts resulted in new muscle fibers filling the defect. Model results were reported as mean \pm 95% confidence interval. Aguilar et al. 2018 experimental data of fibroblasts and SSCs reported as median \pm standard deviation, and Garg et al. 2014 experimental data of M1 and M2 macrophages reported as mean \pm standard error mean [11,82].

A Limiting TGF- β



B Limiting FGF



C Limiting IGF

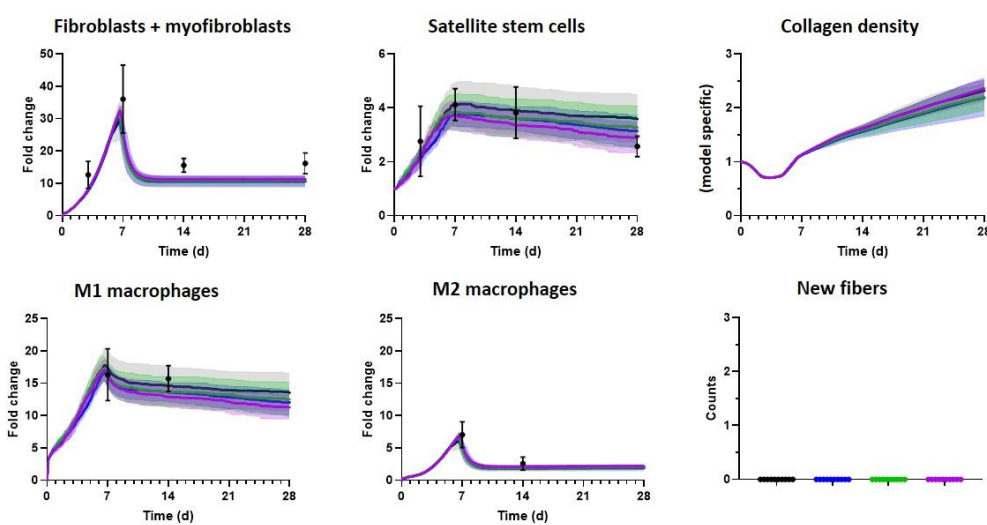


Figure 3-8. Limiting the amount of growth factors produced by fibroblasts in the no repair (NR) ABM revealed that only a large reduction in TGF- β levels altered the collagen density following VML injury. The levels of TGF- β (A), FGF (B), and IGF (C) were reduced to 25%, 50% and 75% below baseline levels, and fibroblast, SSC, and macrophage fold changes, collagen density, and counts of new, regenerated fibers were predicted. A 75% reduction of TGF- β secretion by fibroblasts increased the number of SSCs present and decreased the rate and amount of collagen accumulation (A). None of the perturbations resulted in new fibers filling the defect. Model results were reported as mean \pm 95% confidence interval. Aguilar et al. 2018 experimental data of fibroblasts and SSCs reported as median \pm standard deviation, and Garg et al. 2014 experimental data of M1 and M2 macrophages reported as mean \pm standard error mean [11,82].

3.4.3.2 Combinatorial perturbations

We then simulated VML treatments that incorporated a combination of different approaches. Model perturbation A (limiting the number of M1 macrophages and fibroblasts and altering SSC microenvironmental cues, see Methods for details) alone did not affect the regenerative response of the VML injury (Figure 3-9). When only model perturbation B (lowered SSC differentiation threshold) was implemented there were very few new fibers (Figure 3-9) and most of the differentiated SSCs were located on fibers damaged by secondary necrosis (data not shown). With model perturbation B, there was a decrease in SSC fold change because SSCs differentiated and no longer contributed to the total number of SSCs (Figure 3-9). However, when model perturbation B is implemented in combination with model perturbation A (limiting the number of M1 macrophages and fibroblasts and altering SSC microenvironmental cues), the SSCs are in a better location and environment to generate new fibers and there was improved regeneration as marked by a significant increase in the number of new fibers (Figure 3-9).

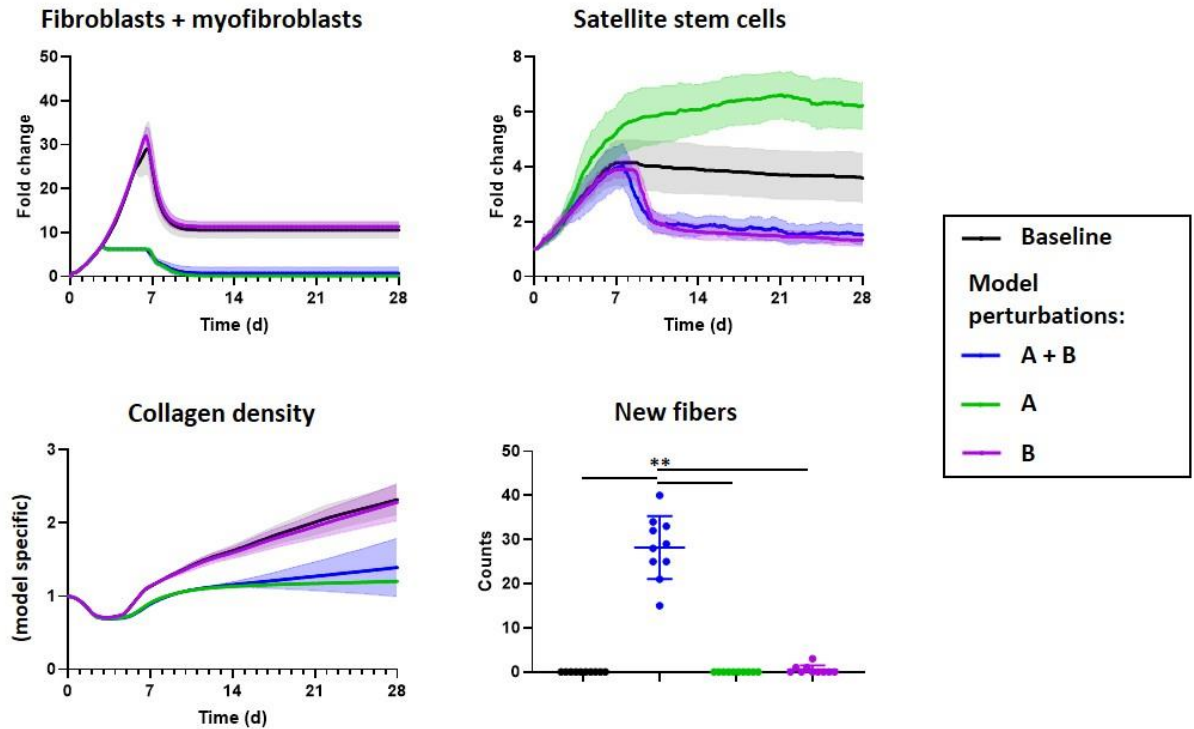


Figure 3-9. A combination of model parameters, reflecting the key biological aspects of failed regeneration in VML injuries, were systematically adjusted alone and in combination to determine how these perturbations affected collagen density and new muscle fiber infiltration into the defect. In the first perturbation, labeled “Perturbation A”, the maximum number of M1 macrophages and fibroblasts was reduced to 75% of baseline levels and SSC migration behaviors were adjusted such that SSCs preferred being in isolation on ECM as opposed to in their niche next to a fiber. Model perturbation B, which corresponded to the threshold for SSC differentiation into myofiber, was reduced so that SSC differentiation was more frequent. When these two perturbations, A and B, were implemented simultaneously, then there was a significant increase in the number of new fibers and collagen density in the defect was reduced. ** $p < 0.0001$, statistical significance between groups using a one-way analysis of variance and Holm-Sidak post hoc test.

3.5 Discussion

The goal of this study was to develop a computational model that predicts muscle regeneration and tissue remodeling following VML injury and/or treatment. By incorporating literature-derived rules from over 100 sources, the ABM was able to capture the autonomous behaviors of fibroblasts and SSCs and simulate regenerative dynamics that were not explicitly defined in the model. We simulated the regenerative response of unrepaired and treated VML injuries, and then we used the model to explore the outcomes of potential therapies and probe mechanisms underlying regeneration following VML injury. One of the fundamental findings of our study is that the model simulations suggested that multiple overlapping cellular mechanisms are responsible for the overt failure of tissue repair in the setting of an untreated VML injuries. Moreover, consistent with existing preclinical and clinical data, the model simulations also indicate that vastly improved muscle regeneration and thus functional outcomes for VML injury cannot be affected by treatments that address individual aspects of the tissue healing response (Figure 3-6, Figure 3-7).

To this end, we conducted theoretical simulations (combinatorial perturbations, Figure 3-9) which predicted that simultaneous alterations in multiple cellular behaviors produced significantly improved muscle regeneration in the VML defect. We explored the impact of the following on muscle regeneration: reducing the presence of pro-inflammatory cells and fibroblasts by 75% and altering the SSC microenvironmental cues required for SSC differentiation (i.e., location on a fiber edge, or on ECM with native healthy stiffness) in model perturbation A, and addressing the absence of pro-differentiation SSC signals in the VML repair environment in model perturbation B. The model simulations suggest that reducing the

presence of pro-inflammatory macrophages and fibroblasts by 75%, simultaneously removing SSC dependency on its microenvironment for differentiation, and additionally lowering the threshold for SSC differentiation so that it occurs more frequently, will significantly increase the number of new fibers in VML defects (Figure 3-9). Although it is not currently possible to implement all of these changes experimentally, the model allowed us to examine if, and how, addressing multiple cellular behaviors in combination would alter muscle regeneration in VML injuries.

It is important to address the simplifying assumptions and limitations of our model. In developing the ABM, our goal was to incorporate fiber regeneration and fibrosis, which are the most prevalent and investigated aspects of repair in VML injury, but we did not incorporate other aspects of muscle structure and function that are known to be affected during regeneration. For example, our ABM does not include neuromuscular junctional changes, microvascular network adaptations, the effect(s) on muscle function and activity (i.e., contraction), or different muscle fiber types. We have focused on a subset of cells (fibroblasts, satellite cells, and macrophages), but there are other cell types present in muscle (e.g. fibroadipocytes, pericyte cells, angioblasts, lymphocytes). For cell types that were modeled, we incorporated relatively simple cellular behaviors and interactions through a series of probability defined rules; as opposed to modeling intracellular behaviors such as individual binding receptors, binding rates, etc. Future studies that expand upon the current model could incorporate more complex behaviors of fibroblasts, different types of collagen, and behaviors of collagen thickening and scarring to more accurately capture and predict fibrotic changes after VML injury.

The development of the model is also limited by the availability of experimental data. The model was primarily informed by the few VML experimental studies that have focused on cell counts at time points less than 2 months post-injury as well as the many studies that have focused on the morphology of the tissue and functional response at longer time points of 3 and 6 months [4,6,15,79]. For the cell types that were modeled, we were limited to defining the cells by the markers used in these experimental studies. However, we had to make assumptions regarding the spatial distribution of cells because this has not been quantified in experimental studies. For example, we had access to experimental data quantifying the number of M1 and M2 macrophages following VML injury but there have been no efforts to describe the spatial concentrations of M1 and M2 macrophages over time [3]. Our ABM represents the higher proportion of M1 macrophages compared to M2 macrophages that has been observed experimentally, and we have assumed a spatial distribution of both M1 and M2 macrophages that places 60% in the border region and 40% in the healthy region [78]. Additional experimental studies are needed to confirm the model predictions about the spatial distribution of cellular behaviors.

In the simulations of no repair and decellularized ECM treated VML injuries, the thickness of the muscle cross-section near, and within, the injury site decreases which is a result of an ECM agent rule that two neighboring ECM agents with low collagen have a probability of merging into a single agent and is consistent with experimental observations [6]. The simulations of VML injuries treated with Losartan did not recapitulate the early cellular dynamics that have been reported experimentally; however, the model was consistent with data collected at later time points that describe cellular changes and failed muscle regeneration

in the VML defect [82]. The Garg et al. 2014 experimental study, for example, reported reduced deposition of collagen type I and no changes in collagen type III in Losartan treated injuries compared to VML injuries without repair [82]. We have incorporated a simplified representation of fibroblast and collagen behaviors, and we did not incorporate collagen subtypes into this ABM. This generalized behavior in our model likely explains why it failed to capture the early cell dynamics; however, in future work, the model can be expanded to represent mechanistic behaviors [127,128]. However, the model's ability to predict cellular changes seen at later time points supports its utility in predicting longer-term remodeling outcomes (i.e. scarring and regeneration), which would be helpful for designing new therapeutic approaches.

With these limitations in mind, the demonstrated ability of the ABM to predict the effects of various treatments for VML injuries motivates its deployment in future studies of novel therapeutics. That is, the model can be utilized to predict the effectiveness of a new therapeutic and aid in the design of more effective therapies to limit the number of experiments that would otherwise need to be conducted. For example, a cell-seeded biomaterial could be simulated in the model and the material's degradability and initial cell density could be optimized through model perturbations. The ABM can also be used to inform the design of experiments by identifying the most critical time points and outcomes to examine in an experimental study—again, perhaps saving the time and expense of unnecessary initial experiments. On a broader scale, computational modeling enables improvements in the design of therapeutics for VML injuries by guiding injury specific treatment options. Finite-element (FE) models can inform therapeutic design based on mechanistic insight of force transmission

[6,129], and now ABMs can be used to inform therapeutic design using cellular mechanistic insight. Furthermore, hybrid models that couple FE modeling with ABMs offer a unique ability to explore the interactions between biomechanical and biochemical mechanisms of muscle regeneration [59,130]. In conclusion, this work demonstrates that an ABM of regeneration following VML injury provides important new insight into the cellular mechanisms governing wound healing and repair. Utilizing computational tools to inform tissue engineering and regenerative medicine therapeutics has the potential to drive more rapid and efficient clinical translation of regenerative therapeutics for VML injuries.

Chapter 4

Experimental-modeling coupled framework informs design of novel therapeutic for volumetric muscle loss injuries

Acknowledgements: Sarah Dyer, Emily Miller, Michael Rariden, George J.
Christ, Silvia S. Blemker

“How long is this going to last? I’m so sick of crying,
I feel like a Villanueva.” – Petra
Jane the Virgin

4.1 Abstract

Volumetric muscle loss (VML) injuries involve a simultaneous loss of resident cells and structures responsible for muscle regeneration resulting in permanent cosmetic and functional deficits. Current preclinical therapeutics for these injuries fail to completely restore functional muscle tissue resulting in a need for improved therapeutic design. Experimental testing of new therapeutics is a resource-intensive and time-consuming process; however, computational tools offer a more cost-effective method to explore the efficiency of new proposed methods for promoting muscle regeneration prior to *in vivo* testing. In this study, we utilized a previously developed computational model to design a novel therapeutic and inform experimental design. Our agent-based model (ABM), which provides a tool to understand cellular mechanisms, informed our therapeutic design of a decellularized ECM with the delivery of exogenous IL-10, as well as time points and outcomes of our experimental design. We found that the *in vivo* data validated our ABM prediction of the regenerative effect for our novel therapeutic. The regenerative effect was assessed by the number of fully differentiated SSCs or myotubes, and the ABM predicted 10.77 ± 5.03 counts/mm² at 28 days post-injury for the therapeutic and the *in vivo* therapeutic data was 11.80 ± 11.36 counts/mm². We also further validated our ABM with *in vivo* cellular data of a decellularized ECM treatment and refined aspects of our ABM using experimental unrepaired VML injury data. We have demonstrated the utility of using computational tools to improve the efficiency of pre-clinical studies; and moving forward, this coupled computational and experimental framework can be expanded to other therapeutics and accelerate the clinical translation of regenerative therapeutics for VML injuries.

4.2 Introduction

In volumetric muscle loss (VML) injuries, there is a simultaneous loss of resident cells and structures responsible for muscle regeneration resulting in permanent cosmetic and functional deficits. The intrinsic regenerative process of skeletal muscle fails, and the mechanisms that limit the ability for the muscle tissue to regenerate are poorly understood [11–13]. VML injuries typically result from trauma, such as battlefield injuries to wounded warriors or civilian vehicular accidents, and currently there are no treatment options that completely restore muscle form and function [3,4,6,76,77]. There is a need for tools that provide insight into the functional and biological mechanisms of VML injury repair and thus can be used to accelerate the development of more efficacious therapies.

Current preclinical therapeutics have included implantation of decellularized extracellular (ECM), minced muscle grafts, and a variety of natural and synthetic biomaterials seeded with muscle progenitor cells and/or a combination of growth factors to help promote SSC proliferation and differentiation [3,4,6,7,15,78,79]. Experimental testing of these therapeutics is a resource-intensive and time-consuming process. For example, the design of a new therapeutic consisting of a cell-seeded scaffold in combination with a growth factor would require multiple groups to be tested in order to determine the ideal cell seeding density and preferred growth factor to include. Then the new therapeutic would need to be tested in multiple injury locations to determine if it aids in restoring function in different mechanical environments. These groups would add numerous animals and hours of experimental work. Computational tools, such as agent-based models, offer a more cost-effective method to predict the effect of new therapeutics prior to *in vivo* testing.

Agent-based models (ABM) provide a tool to improve the mechanistic understanding of how cellular behaviors impact tissue repair/remodeling following VML injury. ABMs simulate cellular behaviors and show the effects of these cellular behaviors on the physiological system as a whole. Agents represent individual cells within a tissue as well as environmental components, such as ECM, and the computational platform synthesizes the published work in the field, as agent behaviors are governed by literature-derived rules [61,62,85,86]. ABMs can also be used to predict the regenerative effects of a new therapeutic and inform the experimental design by identifying the most critical time points and outcomes to examine.

The goal of this work was to utilize our previously developed ABM (Chapter 3) for VML injuries to design a novel therapeutic and inform our experimental design before testing the model predictions *in vivo* (Figure 4-1). We used the ABM to design our new therapeutic, consisting of a decellularized ECM scaffold and exogenous growth factor interleukin-10, and to inform the time points and outcomes of our experimental design. Decellularized ECM was chosen as the material for the therapy because it provides a structure for cells to migrate into the injury defect [76,84,131]. Previous ABMs have modeled exogenous growth factor delivery. Some ABMs have assumed the growth factor was delivered to the tissue and modeled the delivery by simulating the cellular effect of the growth factor [61,132], and others assumed focal delivery and modeled the growth factor's diffusion into the tissue [133]. In this work, the focus was on delivery of exogenous growth factors to the tissue. We tested our model-informed novel therapeutic *in vivo* and validated the ABM prediction of its regenerative effect. We also used no repair *in vivo* data to refine the regional cellular distributions in the ABM.

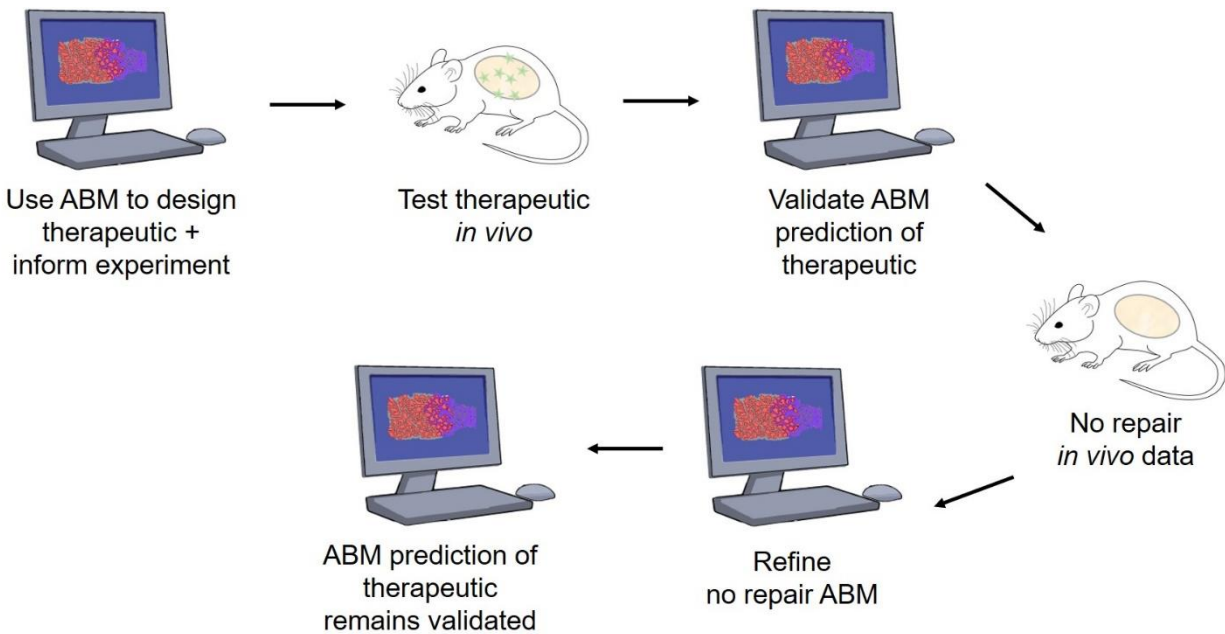


Figure 4-1. Coupled framework of *in silico* and *in vivo* methods to design novel therapeutic for VML injuries.

4.3 Methods

4.3.1 Agent-based model

The previously developed computational model was used to design a new therapeutic for VML injuries and optimize experimental variables of the therapeutic. Briefly, the previously developed ABM predicted tissue regeneration following VML injury from the autonomous actions of different agents in the model (Chapter 3). The ABM represented a two-dimensional cross-section of rat skeletal muscle consisting of 164 muscle fibers and was built in Repast, a java-based modeling platform (Argonne National Laboratory). The agents that occupied space in the model included muscle fibers, ECM, necrotic muscle tissue, fibroblasts, myofibroblasts, satellite stem cells (SSCs), myoblasts, myocytes, and myotubes. Model components whose

spatial location was not tracked included eleven growth factors and three types of inflammatory cells: neutrophils, proinflammatory (M1) macrophages, anti-inflammatory (M2) macrophages. The ABM consisted of a healthy muscle region and a border region that was adjacent to the defect. The healthy region consisted of the muscle fibers near the VML injury that were not affected by the defect [89]. At initialization, the healthy region was approximately 130 μm from the injury space and by 7 days post-injury, it was 350 μm from the injury space. The border region consisted of the fibers within 350 μm of the injury at 7 days post-injury and the injury space [4,78,89]. Simulations were run with a 1-hr time step for a simulated 28 days following VML injury. At each time step, every cellular agent determined its regional location in the simulation space and then its behaviors were determined by a probability-based decision tree (Figure 3-3, Table 3-1, Table 3-2). The key model outputs included the time-varying counts for fibroblasts, SSCs, and M1 and M2 macrophages in the model. The model predicted counts of each cell type were divided by the area of the region and then normalized by the number of cells at initialization to calculate the fold change and allow for direct comparison with values from *in vivo* studies. All simulations were repeated 10 times to capture the stochastic cell behaviors of the model.

4.3.1.1 Therapeutic and experimental design using the ABM

The new therapeutic consisted of decellularized ECM in combination with exogenous growth factors. Decellularized ECM in the injury space was modeled as four layers of 10 μm thick, based on unpublished measurements (Christ Lab), to be consistent with *in vivo* implantation (Appendix B). To model exogenous growth factor delivery in the ABM, it was

assumed that growth factor values greater than 0 have a chance of affecting cellular behavior for there was no therapeutic range of growth factors for VML injury in the literature. A simplified delivery of growth factor was assumed using a piecewise function and pharmacokinetic data for IL-1 β , a growth factor with similar molecular weight and isoelectric point to the growth factors of interest [134]. For hours 1 – 4 after delivery, the growth factor was at its max level before decaying exponentially with a half-life of 1.6 hours. Bioavailability for subcutaneous injection was set at 50% [134]. It was also assumed that the growth factor was evenly distributed throughout the tissue.

A dose sensitivity analysis was run for each growth factor – FGF, IGF, and IL-10. The growth factor concentration delivered was 0.5, 1, 2, 5, 10, and 20 times the maximum amount of the growth factor in the unrepaired ABM. For the growth factors promoting SSC proliferation, the output examined was the maximum number of SSCs in the simulation. For the growth factor promoting SSC differentiation, the output examined was the maximum number of myotubes in the simulation. Myotubes are fully differentiated SSCs capable of repairing muscle fibers and are a marker of muscle regeneration [21,135]. An increase in the number of myotubes is indicative of improved muscle repair. In simulations testing the delivery of a combination of growth factors, the highest concentration of each growth factor was used. The ABM was also used to optimize the delivery of IL-10. Single injections of three doses every 48 hours were simulated starting at 5, 7, or 10 days after VML injury. The continuous infusion of IL-10 for 7 days was simulated starting at 5 or 7 days post-injury. The highest concentration, 20 times the max level in the unrepaired model, was used for all delivery simulations.

4.3.1.2 ABM refinement

ABM model parameters were refined to recapitulate the *in vivo* experimental results of unrepaired VML injuries (Table 4-1). As explained in Chapter 3.3.1.1, the probability of a cell behavior occurring was weighted by the cell behavior signal and a normalization factor accounting for the size of the ABM grid. When initialing building the ABM in Chapter 3, the normalization factor for behavior signals was set to account for the size of the ABM grid and then the maximum probabilities of cell behaviors were tuned (Table 3-3). Varying the max chance of SSC differentiation resulted in minimal changes in the number of differentiated SSCs (Appendix C). Therefore, to re-parameterize the ABM to capture the myotubes counted in the experimental data, the normalization factor for SSC differentiation behavior signal was tuned.

Originally in the ABM, SSCs and fibroblasts were assumed to only recruit to the border region. The literature demonstrated that SSCs were recruited to an injury site in both single fiber and whole muscle experiments [79,88,136]. However, there was no clear definition of the area size near an injury which will recruit SSCs. The *in vivo* data showed that SSCs were recruited to the border and healthy region, so a parameter was added to the ABM to define the probability of a SSC recruited to the border region. If the SSC was not recruited to the border region, then it was recruited to the healthy region.

For fibroblasts, the VML literature was consistent in demonstrating that fibroblasts were the major contributor in replacing connective tissue lost in the injury but the area size near an injury where fibroblasts were recruited was not defined [10,79,90]. Based on the *in vivo* data which showed that fibroblasts were recruited to the border and healthy region, a parameter was added to the ABM to define the probability of a fibroblast recruited to the border region.

The parameter for the maximum probability of fibroblast recruitment was re-parameterized.

These parameters were tuned to capture the regional distribution seen *in vivo*.

Based on published data for a pan macrophage marker, the original regional distribution of M1 and M2 macrophages was approximated to be 60% in the border region and 40% in the healthy region [78]. Following the *in vivo* data, the M2 macrophage distribution was updated to be 50% in the border and 50% in the healthy region.

Table 4-1. Model parameters were tuned to recapitulate *in vivo* experimental results of VML injuries without repair

<i>Probability Parameter</i>	<i>Equation</i>	<i>Range Tested</i>	<i>Value</i>
Normalization factor of SSC differentiation signal, x_4	SSC differentiation probability = $1/(x_4 - \text{differentiation signal})$	-5000 – 5000	0
Probability of fibroblast recruited to border region, x_1	$1/x_1$	0.2500 – 0.7500	0.2500
Maximum probability of fibroblast recruitment per hour, x_2	If fibroblast recruitment probability > x_2 , proliferation probability = x_2	0.0400 – 0.2000	0.0667
Probability of SSC recruited to border region, x_3	$1/x_3$	0.2500 – 0.7500	0.5000

4.3.2 Animals

In total, 50 male Lewis rats (Charles River Laboratories) aged 11 weeks were used for the *in vivo* experiment. Experimental groups and group sizes were as follows: no repair group (n = 20), decellularized ECM (decell ECM) group (n = 20), and decellularized ECM with IL-10 (IL-10 + decell ECM) group (n = 10). For the no repair and decell ECM groups, 5 rats were sacrificed at 7, 10, 14, and 28 days after VML injury. For the IL-10 + decell ECM group, 5 rats were sacrificed at 14 and 28 days post-injury. The ABM model predictions informed the time points of the *in vivo*

study and the immunofluorescent stains chosen. The Institutional Animal Care and Use Committee of the University of Virginia approved all animal procedures.

4.3.2.1 Surgical procedures

For VML injury creation surgery, the rat was under isoflurane anesthesia and a 4 cm incision was made from the armpit down the length of the rat, approximately 2 cm from the spine. The cranial portion of the LD was exposed and a circular injury 12 mm in diameter was created using a biopsy punch (Acuderm). The VML injury was 10 mm from the cranial edge and 1-2 mm from the lateral edge of the LD. For groups with decell ECM, the scaffold was folded twice (longitudinally and transversely), trimmed to fit the size of the injury, and then sutured into the injury bed with 6-0 vicryl sutures (Ethicon) [6,7]. Decellularized ECM scaffolds were prepared as previously described [8,137]. In all groups, fascia and fat pad were sutured over the injury site with 6-0 vicryl suture, and the skin was sutured with 5-0 prolene (Ethicon) suture. Buprenorphine (0.05 mg/kg, subcutaneously) was administered for 3 days.

The rats to be sacrificed at 14 day and 28 day time points in the decell ECM and IL-10 + decell ECM groups had subcutaneous pumps implanted at 7 days post-VML injury. The pumps and catheters (Alzet 2001, 1 μ L/hr for 7 days) were filled using sterile techniques the night before implantation and placed in sterile 0.9% saline at 37°C to minimize the chance of occlusion or a clot forming in the catheter. The decell ECM group received pumps filled with sterile PBS, and the IL-10 + decell ECM group received IL-10 dissolved in 0.1% BSA and PBS at a concentration of 0.125 μ g/ μ L. The growth factor value in the model does not translate to an experimental dose, thus a previously published IL-10 dose of 10 μ g/kg per day was used *in vivo*

[138,139]. Under isoflurane anesthesia, a 1 cm long incision was made 8 cm caudal from the neck and 2 cm lateral to the spine. A subcutaneous pocket was made for the pump, and the distal end of the catheter was tunneled under the fascia to the LD injury. The catheter was secured in place with 4-0 prolene suture (Ethicon). The incision was closed with staples. After 7 days, the pump and catheter were removed under isoflurane anesthesia and the incision was closed with staples. Ketoprofen (4 mg/kg, subcutaneously) was administered at time of pump implantation and removal.

At the specified time points, experimental and uninjured contralateral control muscles were removed for analysis. Animal and LD muscle weights at the time of VML injury surgery and explant are in Table 4-2. For the 14 and 28 day harvest groups, whole blood was collected by cardiac puncture and then centrifuged to collect serum. IL-10 levels were detected in serum using the rat IL-10 quantitative sandwich ELISA kit as described by the manufacturer's protocol (Abcam).

Table 4-2. Animal weight and LD muscle weights

<i>Group</i>	<i>Animal weight at VML surgery (g)</i>	<i>Excised injury muscle weight (g)</i>	<i>Animal weight at explant (g)</i>	<i>LD muscle weight (g)</i>
<i>No repair</i>				
7d explant (n = 5)	332.3 ± 21.42	0.149 ± 0.021	330.4 ± 24.32	1.076 ± 0.082
10d explant (n = 5)	331.5 ± 14.68	0.154 ± 0.018	339.7 ± 8.505	1.000 ± 0.061
14d explant (n = 5)	332.8 ± 10.47	0.148 ± 0.014	355.3 ± 10.14	1.031 ± 0.151
28d explant (n = 5)	346.4 ± 28.49	0.155 ± 0.033	353.3 ± 3.643	0.928 ± 0.287
<i>Decell ECM</i>				
7d explant (n = 5)	325.4 ± 9.858	0.146 ± 0.016	321.2 ± 14.92	1.191 ± 0.093
10d explant (n = 5)	323.7 ± 21.14	0.172 ± 0.010	333.4 ± 12.86	1.238 ± 0.252
14d explant (n = 5)	329.5 ± 9.958	0.145 ± 0.018	350.5 ± 11.60	1.207 ± 0.174
28d explant (n = 5)	339.1 ± 4.109	0.166 ± 0.023	385.2 ± 11.62	1.067 ± 0.207
<i>IL-10 + decell ECM</i>				
14d explant (n = 5)	323.7 ± 6.855	0.144 ± 0.014	345.2 ± 9.830	1.362 ± 0.249
28d explant (n = 5)	340.7 ± 7.115	0.159 ± 0.023	374.9 ± 12.06	1.066 ± 0.173

4.3.2.2 Histology and immunohistochemistry

Muscles from all experimental groups were frozen in liquid nitrogen cooled isopentane. The injury area was divided in half, and muscle samples were embedded in OCT floating in a dry ice/ethanol bath at approximately -70°C to help prevent freeze-artifact. Transverse muscle sections (10 µm thick) were cut from the middle of the injury region of the muscle. Hematoxylin and eosin stains were done using standard techniques to determine the basic morphology of cells in and around the injury and to observe connective tissue deposition.

For immunofluorescent staining, slides were prepared by fixing the tissue (4% PFA in PBS) for 10 minutes followed by antigen retrieval if needed. Autofluorescence reduction treatment was with 0.3% Sudan black solution for 15 minutes and then permeabilization with 0.5% Triton-X-100 in PBS for 30 minutes. Primary antibodies were incubated overnight at 4°C to detect myotubes or immature myosin heavy chain (anti-mouse F1.652, Hybridoma Bank, 1:10 dilution), SSCs (anti-mouse Pax7, Hybridoma Bank, 1:50 dilution with antigen retrieval), laminin (anti-rabbit ab11575, Abcam, 1:200 dilution), fibroblasts (anti-rabbit PDGFRa, ab203491, Abcam, 1:500 dilution with antigen retrieval), and macrophages (anti-mouse CD68, MCA341R, BioRad, 1:100 dilution with antigen retrieval; anti-rabbit CD163, ab182422, Abcam, 1:400 dilution with antigen retrieval). M1 macrophages stained CD68+/CD163- and M2 macrophages stained CD163+ [7,61,82]. PDGFRa+ cells were representative of non-myogenic fibro-adipogenic progenitor cells [90,95,140,141]. Secondary antibodies were applied for 2 hrs at room temperature at 1:400 dilution: alexa fluor 488 (anti-rabbit, ab150077, Abcam; anti-mouse, ab150113, Abcam) and alexa fluor 594 (anti-rabbit, ab150080, Abcam; anti-mouse, ab150116, Abcam). Slides were mounted with DAPI containing mounting media.

All slides were imaged using a Leica Inverted Confocal Microscope DMI8 and 20x objective. For each animal, a 3x3 image panel was acquired of the injury/muscle interface for 2 sections. Custom MATLAB code was used to define the healthy and border regions of the image and quantify the number of cells in each region that were double positive for the respective marker and DAPI. The border region was defined by identifying the fiber closest to the injury space and then measuring 350 μm , consistent with the ABM defined border region, into the muscle (Figure 4-2). The counts of each cell type were divided by the area of the region and

then normalized by the number of cells in the contralateral control to calculate the fold change and allow for direct comparison with values from ABM predictions.

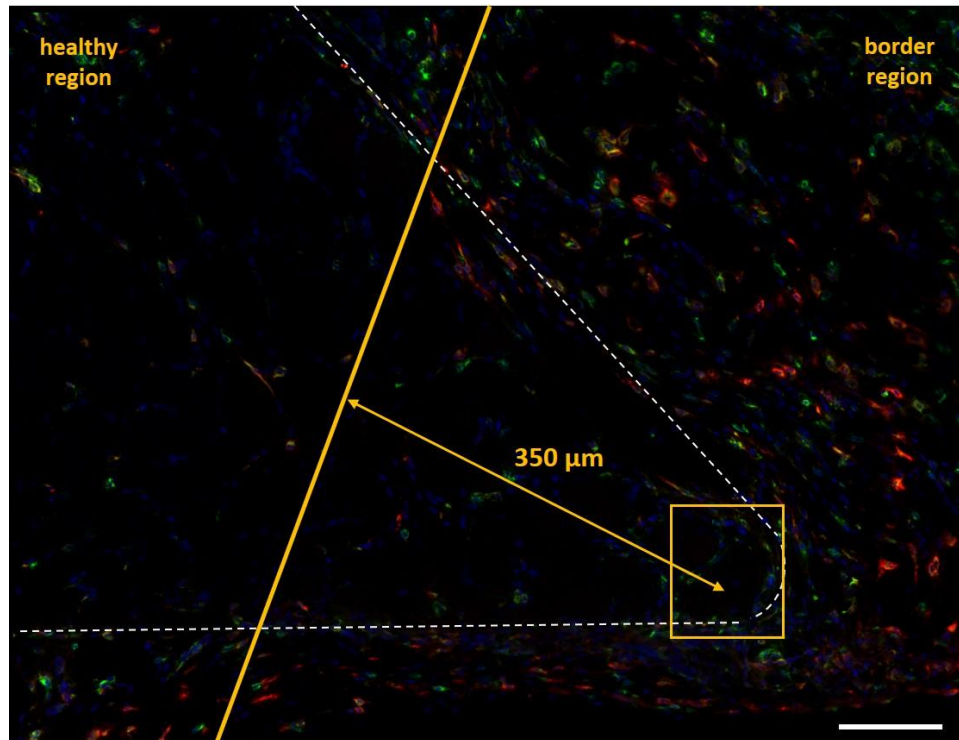


Figure 4-2. Immunofluorescent stain of decellularized ECM at 10 days post-injury for macrophages (M1 CD68+ (green)/CD163-, M2 CD163+ (red), and DAPI (blue)). The white dashed line marks the outline of the native LD muscle. The native LD muscle is on the left side and the injury on the right side of the image. The yellow box marks the fiber closest to the injury space, and then from that fiber 350 μm is measured into the native muscle to identify the edge of the border region, marked by the solid yellow line. Scale bar = 100 μm .

4.3.3 Statistical analysis

In vivo data were presented as mean \pm standard deviation and ABM predictions were presented as mean \pm 95% confidence interval, unless otherwise noted. For dose sensitivity analysis using the ABM, statistical significance between the count of each concentration of exogenous growth factor and the baseline count was calculated using a t-test and Holm-Sidak

post hoc test. All other statistical significance was determined using a one-way analysis of variance (ANOVA) and Tukey multiple comparisons test. The level of significance was set a $p < 0.05$ in all statistical tests. Statistical analysis was conducted using GraphPad Prism.

4.4 Results

4.4.1 ABM predictions for therapeutic and experimental design

Using the ABM model of a VML injury treated with decellularized ECM, a dose sensitivity analysis of exogenous growth factor delivery reveals that increasing the concentration of FGF and IGF, SSC proliferation growth factors, increases the maximum number of SSCs (Figure 4-3A, B). Increasing the concentration of IL-10, SSC differentiation growth factor, significantly increases the maximum number of myotubes (Figure 4-3C). Although FGF and IGF increase the number of SSCs near the injury, delivering the growth factors in combination with IL-10 did not significantly improve the number of myotubes and thus would not significantly improve the repair of muscle fibers in the VML injury (Figure 4-4A). The combination of IGF, FGF, and IL-10 resulted in less myotubes compared to IL-10 alone for IGF and FGF promote SSC proliferation, are modeled as suppressing differentiation and thus two proliferating growth factors further impair differentiation (Chapter 3.3.1). Informed by the ABM predictions, exogenous delivery of IL-10 was chosen for the therapeutic. Then the ABM model of a decellularized ECM treated VML injury was used to design the experimental delivery of IL-10. A 7-day continuous infusion of IL-10 starting at day 7 predicted the highest number of myotubes in the injury and was chosen for the *in vivo* experiment (Figure 4-4B).

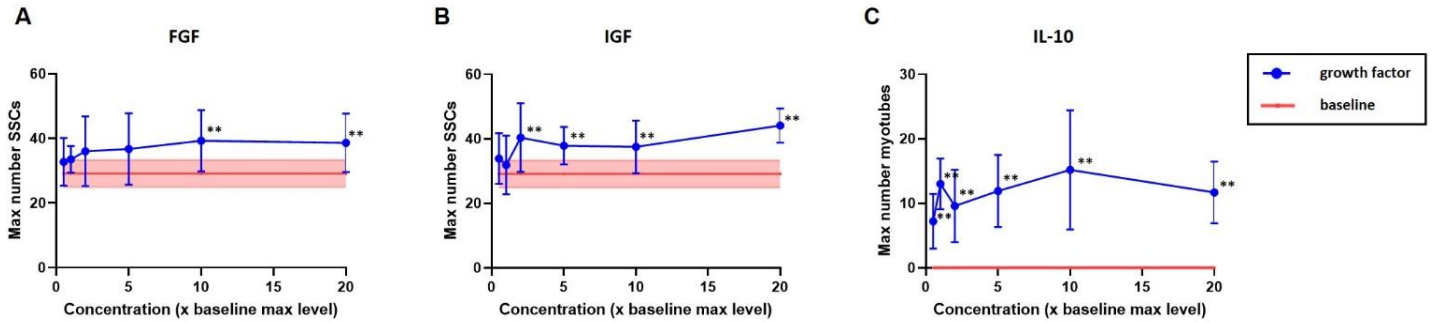


Figure 4-3. ABM model of a VML injury treated with decellularized ECM used to inform therapeutic design. Dose sensitivity analysis of exogenous growth factors revealed that the addition of a SSC proliferation growth factor – FGF (A), IGF (B) – increased the number of SSCs. While delivery of a SSC differentiation growth factor, IL-10 (C), significantly increased the number of terminally differentiated SSCs or myotubes, a marker of muscle regeneration. Model results reported as mean \pm standard deviation. ** $p < 0.05$

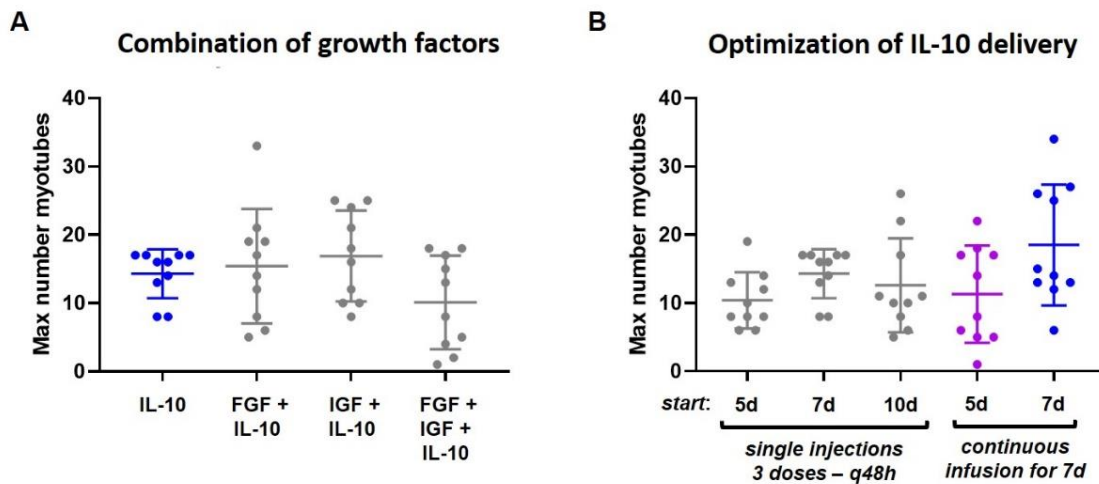


Figure 4-4. Delivery of a combination of growth factors did not significantly improve the number of myotubes in the ABM model of a VML injury treated with decellularized ECM (A). Thus, the delivery of IL-10 alone was optimized using the ABM. Single injections of 3 doses of IL-10 given every 48 hours was simulated with doses starting at 5, 7, and 10 days after VML injury creation, and continuous infusion of IL-10 for 7 days starting at 5 and 7 days after VML injury was simulated (B). Continuous infusion of IL-10 for 7 days starting at day 7 post-VML injury predicted the highest number of myotubes. Model results reported as mean \pm standard deviation.

4.4.2 *In vivo* experimental validation of model-predicted therapy effect

The treatment of decellularized ECM in combination with continuous infusion of IL-10 for 7 days starting at 7 days post-VML injury *in vivo* validated the ABM predictions of increased myotube counts (Figure 4-5). The initial ABM predicted a treatment with IL-10 delivery would result in significantly more myotubes at 14 days and 28 days post-injury (initial ABM: 17.00 ± 3.94 counts/mm²) compared to an unrepaired and decellularized ECM treated injury. For *in vivo* experimental data of myotube counts, the IL-10 group was significantly larger than the other two groups at 14 days and the IL-10 group was also larger at 28 days, although not significantly. The experimental results validated the model predictions. No significant differences in serum levels of IL-10 concentration were found *in vivo* (Figure 4-6).

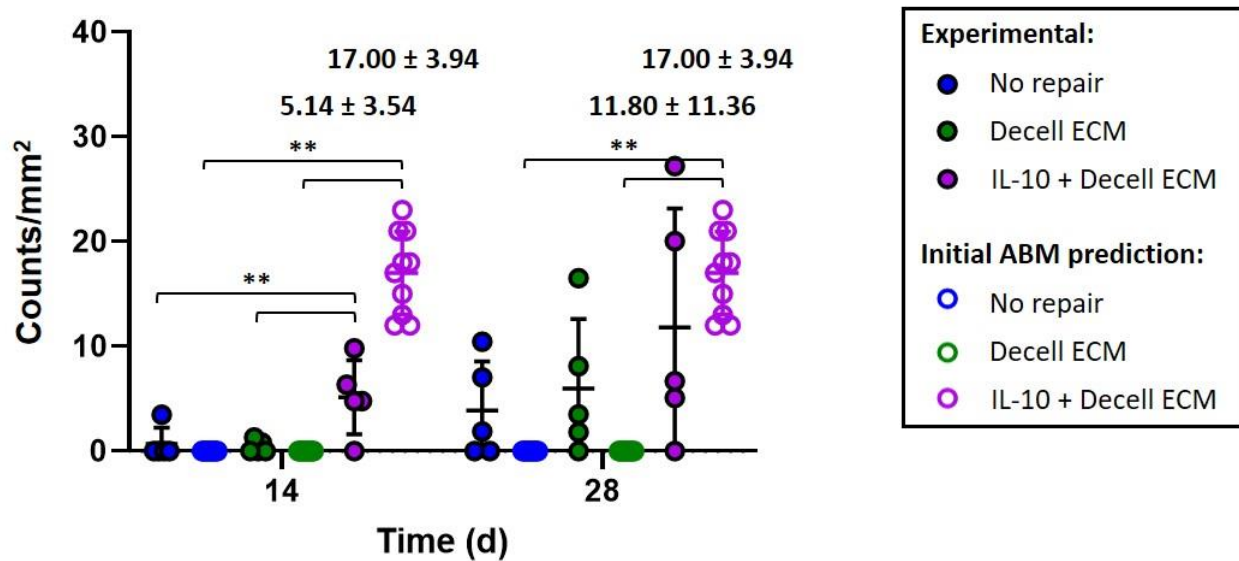


Figure 4-5. The continuous infusion of IL-10 for 7 days *in vivo* validated the initial ABM predictions of myotube counts in the total area. At 14 days post-injury, the model predicted significantly more myotubes compared to unrepaired and decellularized ECM alone and this was confirmed *in vivo*. Experimental and model results reported as mean \pm standard deviation. ** $p < 0.05$, statistical significance between groups using a one-way analysis of variance at each time point and Tukey multiple comparisons test.

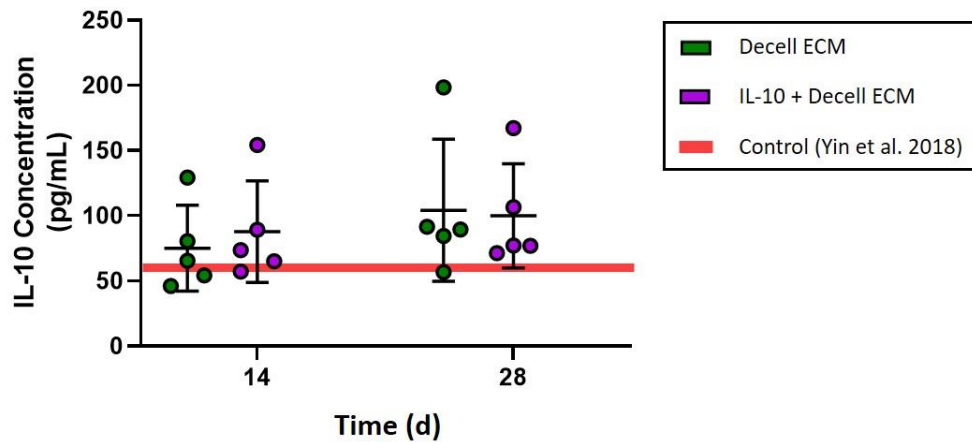


Figure 4-6. *In vivo* serum levels of IL-10 concentration were not significantly different between VML injuries treated with decellularized ECM with continuous infusion of IL-10, decellularized ECM alone, and control rats with no injuries [142].

4.4.3 Unrepaired VML injury *in vivo* experimental cell counts comparable to ABM predictions

For an unrepaired VML injury, the cell counts of SSCs, fibroblasts, and macrophages were compared to ABM predictions and literature experimental data. The experimental fold of SSCs and macrophages was consistent with ABM predictions and literature experimental data (Figure 4-7A, C) [11,82]. For fibroblasts, the experimental and ABM fold change was consistent at 7 and 10 days post-injury; but experimentally, the counts of PDGFR α + cells increased at the later time points of 14 and 28 days (Figure 4-7B). The increased experimental fibroblast count corresponds with the qualitative observation of increasing connective tissue over time seen in the no repair VML injury (Figure 4-8).

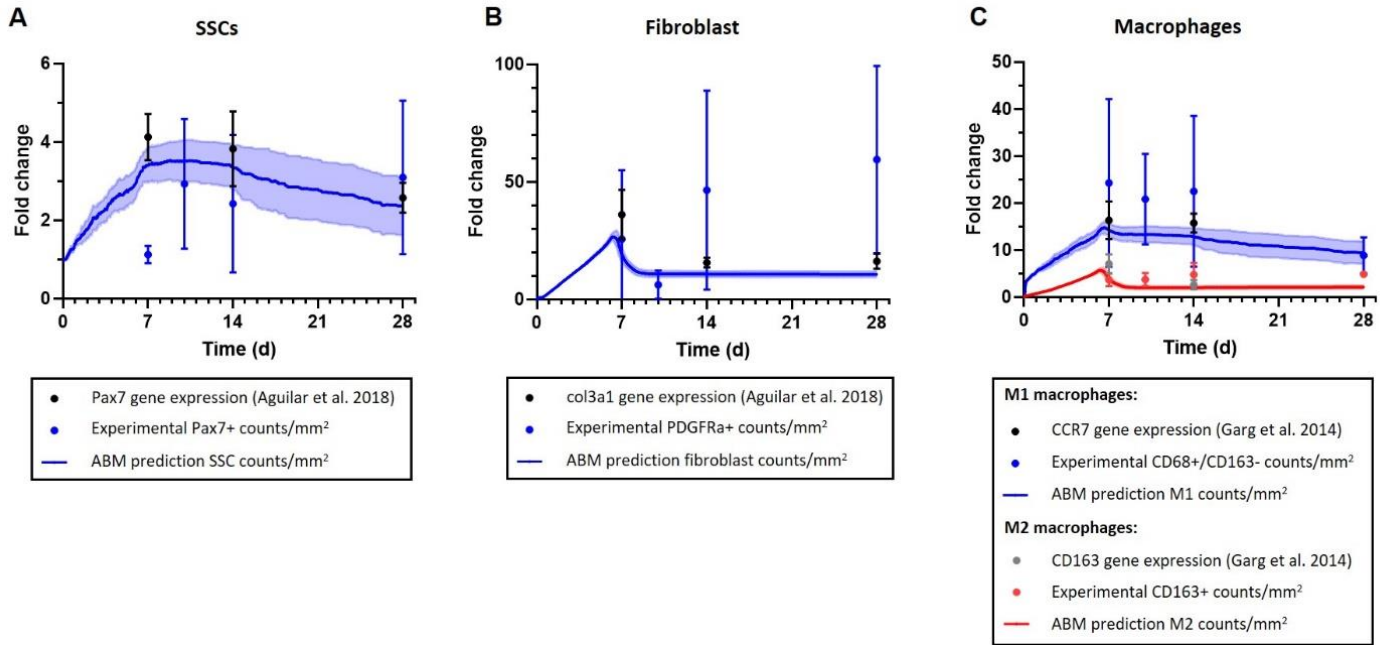


Figure 4-7. For unrepaired VML injuries, comparison of ABM predictions and *in vivo* experimental data of SSCs (A), fibroblasts (B), and macrophages (C). The ABM predictions of SSC and macrophages were similar to experimental data. The ABM predicted fibroblast counts and experimental counts were similar at 7 days post-injury but then diverged at later time points. Aguilar et al. 2018 experimental data of fibroblasts and SSCs reported as mean \pm standard deviation, and Garg et al. 2014 experimental data of M1 and M2 macrophages reported as mean \pm standard error mean [11,82]. Literature fold change is the gene expression normalized by the contralateral control gene expression.

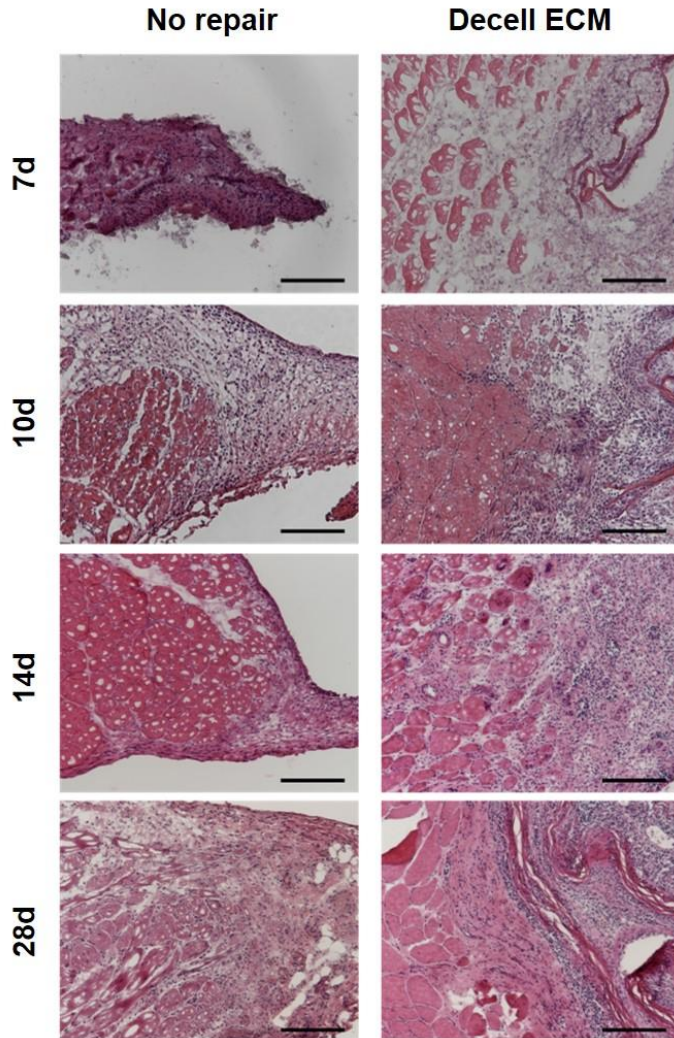


Figure 4-8. Histology of hematoxylin and eosin-stained rat LD muscle shows the cross-section in no repair and decellularized ECM treated VML injuries 7, 10, 14, and 28 days post-injury. The native LD muscle is on the left side and the injury on the right side of each image. Holes in some muscle fibers are a result of freeze artifact. Scale bars = 200 μm .

4.4.4 Decellularized ECM treated VML injury *in vivo* experimental cell counts larger than ABM predictions

A VML injury treated with decellularized ECM was created *in vivo* and cell counts of SSCs, fibroblasts, and macrophages were analyzed over 28 days and compared to ABM predictions. The experimental fold change of SSCs was similar to ABM predictions, although it was a bit lower than ABM predictions at 7 and 10 days post-injury (Figure 4-9A). The experimental fibroblast fold change had similar discrepancies to the ABM predictions at 14 and

28 days post-injury as the unrepaired VML injury (Figure 4-9B). For macrophages, the experimental fold change of M1 and M2 macrophages was higher than the ABM predictions (Figure 4-9C).

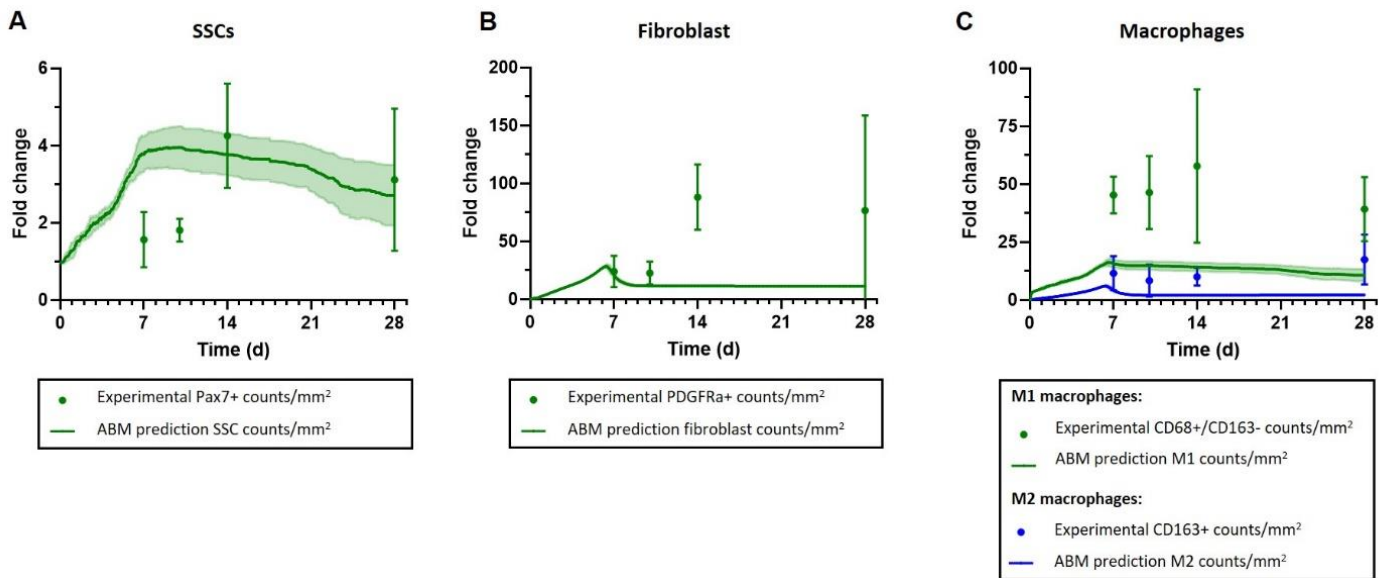


Figure 4-9. For VML injuries treated with decellularized ECM, comparison of ABM predictions and *in vivo* experimental data of SSCs (A), fibroblasts (B), and macrophages (C). The experimental data and ABM predictions for SSC fold change were consistent. The fibroblast and macrophage experimental fold changes were higher than ABM predictions.

4.4.5 ABM refined based on experimental results of VML injuries without repair

The cellular regional distribution of unrepaired VML injury experimental data revealed an aspect of the ABM to be refined and improved. The experiment SSC regional distribution showed approximately 50% of the cells in the border region and 50% in the healthy region; however, the initial ABM predicted 90% in the border region and only 10% in the healthy region (Figure 4-10A). There was also discrepancy between the regional distributions of experimental and ABM fibroblast counts. The experimental data showed a 50% border, 50% healthy region

breakdown and the initial ABM predicted a 90% border, 10% healthy region breakdown (Figure 4-10B). The M1 macrophage regional distribution was consistent between experimental data and ABM predictions (data not shown), but the experimental M2 macrophage regional distribution was approximately 50% in the border and 50% in the healthy region; while the initial ABM prediction was 60% in the border and 40% in the healthy region (Figure 4-10C).

After refining and tuning model parameters (Table 4-1), the refined ABM predicted SSC regional distribution was more similar to the 50%-50% distribution of experimental results (Figure 4-10A). However, at 10 and 14 days post-injury, the refined ABM predicted slightly more SSCs in the border region than the experimental data. The total SSC counts predicted by the ABM were also slightly larger than the *in vivo* total data (Figure 4-7A), so it's likely that the smaller area of the regional counts highlighted the discrepancy between ABM and experiment. Overall, the SSC fold changes are order of magnitudes smaller than the other cells and this difference in SSCs between model and experiment is unlikely to affect the predicted outcome of the ABM. The refined ABM predicted fibroblast regional distribution was similar to the experimental data at 7 days post-injury but then diverged from experimental counts at later time points (Figure 4-10B). The refined ABM predicted M2 macrophages regional distribution was a similar distribution of 50% in the border and 50% in the healthy region, like the experimental data (Figure 4-10C).

The experimental myotube counts of unrepaired VML injuries at 28 days post-injury revealed that a few SSCs were terminally differentiating to myotubes (*in vivo*: 3.88 ± 4.68 counts/mm²); however, the ABM did not capture this behavior (initial ABM: 0 counts/mm²) (Figure 4-5). The unrepaired VML injury ABM was refined and parameters re-tuned to capture

this occurrence (refined ABM: 6.21 ± 6.83 counts/mm²) (Table 4-1, Figure 4-11A). After refinement of the ABM, the model predictions of the therapeutics' regenerative effect remained validated by experimental data (Figure 4-11B). For the therapeutic group at day 28, the refined ABM predicted myotube counts (refined ABM: 10.77 ± 5.03 counts/mm²) that were more similar to *in vivo* experimental data (*in vivo*: 11.80 ± 11.36 counts/mm²) than the initial ABM (initial ABM: 17.00 ± 3.94 counts/mm²).

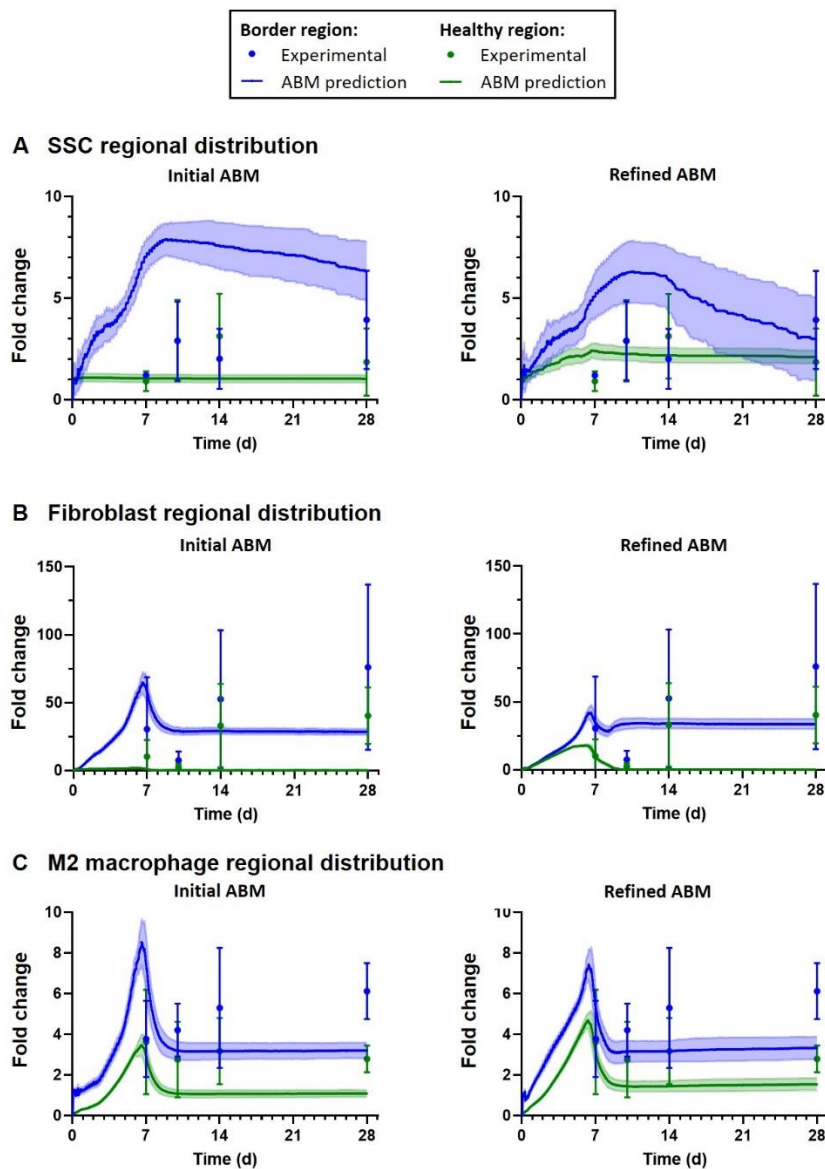


Figure 4-10. Experimental regional cellular distributions of SSCs (A), fibroblasts (B), and M2 macrophages (C) led to additional refinement of the ABM. For unrepaired VML injuries, the initial ABM predicted too many cells in the border region whereas the experimental data showed a 50%-50% distribution of the cells between the regions (column I). After tuning model parameters, the refined ABM predictions of regional distributions were similar to experimental counts (column II).

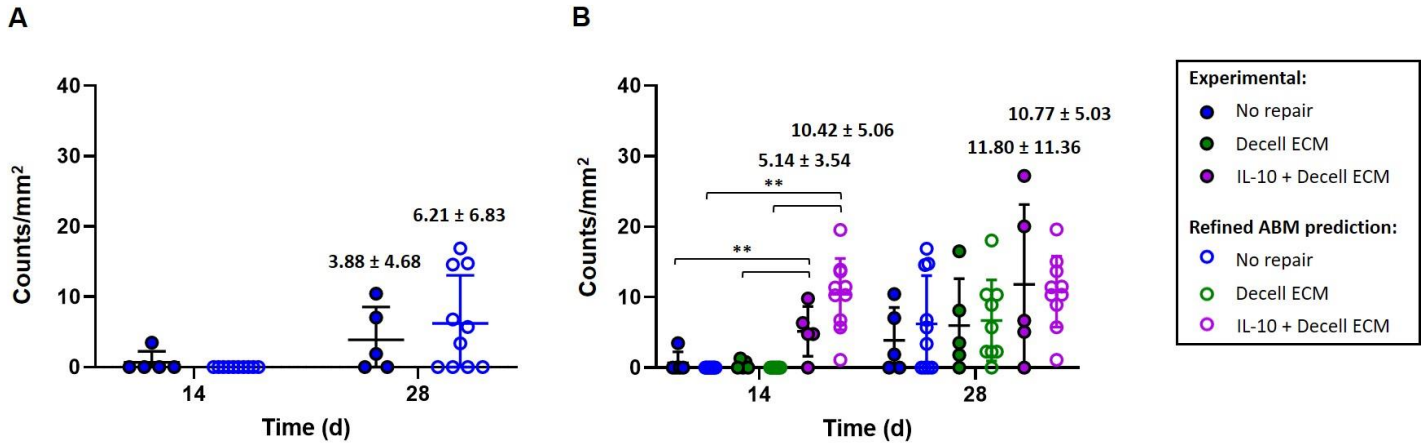


Figure 4-11. The unrepaired VML injury ABM was tuned to capture the myotube counts measured experimentally at 28 days post-injury (A). Refinement of the ABM did not alter the outcome of the ABM predictions for the therapeutic experimental data validated the model (B). Experimental and model results reported as mean \pm standard deviation. ** $p < 0.05$, statistical significance between groups using a one-way analysis of variance at each time point and Tukey multiple comparisons test.

4.5 Discussion

VML injuries are a challenging medical condition to treat because of the simultaneous loss of resident cells and structures responsible for muscle regeneration and the functional and biological mechanisms of repair are poorly understood [11–13]. Current treatments inadequately treat VML injuries, although regenerative medicine technologies offer great potential for improved functional outcomes [6–8]. There is a need for more rapid and efficient clinical translational of regenerative therapeutics; thus, in this work we demonstrate the utility of a computational model to design a novel therapeutic and aid in experimental design. The predictive capabilities of the ABM allowed testing of one therapeutic, instead of over 11 different combinations of growth factor delivery, which saved hundreds of hours of experimental work and over 100 rats.

Our ABM simulations in Chapter 3 revealed that treatments designed to modulate the pro-inflammatory and fibrotic cellular components of the tissue healing response would not be successful in improving muscle regeneration following VML injury (Figure 3-6, Figure 3-7, Figure 3-8). We also revealed in theoretical simulations that lowering the threshold for SSC differentiation, so that it occurs more frequently, helps to improve the muscle regeneration in the injury (Figure 3-9). Therefore, our focus in this new therapeutic was to alter SSC behaviors. The ABM reflects the current understanding of biology and currently it is believed that the microenvironment and secreted factors influence SSC behavior in muscle regeneration (Table 3-2) [21,40,104]. We focused on altering the growth factor environment because it can be easily adjusted *in vivo*. Specifically, the effects of fibroblast growth factor (FGF), insulin-like growth factor (IGF), and interleukin-10 (IL-10) on muscle regeneration were explored [45,109–113]. Through a series of ABM simulations, we decided to deliver exogenous IL-10 continuously via a subcutaneous pump to VML injuries which will help to eliminate experimental variability of delivery.

To our knowledge, the effect of exogenous IL-10 for muscle regeneration has been predominantly tested *in vitro* and this was the first use of IL-10 for VML injuries *in vivo* [110,113,143]. The effect of IL-10 on SSC differentiation behavior was encouraging but was inadequate to replace lost muscle fibers in the injury space. The H&E images of the IL-10 and decellularized ECM group were comparable to the decellularized ECM group images, and there were few new fibers seen in the injury space (Figure 4-8). This observation suggests that the differentiated SSCs were located on remaining fibers damaged during injury creation. Therefore, it was unlikely that IL-10 in combination with decellularized ECM improved the

muscle's functional response; however, incorporating IL-10 with more complex therapeutics that can regenerate some of the lost muscle fibers may further improve the regenerative and functional outcome.

The unrepaired VML injury ABM predictions of SSCs and macrophages were consistent with experimental data; however, there was discrepancy in the fibroblast counts after 10 days post injury. The ABM was built and tuned to previously published experimental data of a VML injury in the rat tibialis anterior (Chapter 3) [11]. In that study, the H&E images showed less connective tissue at 14 and 28 days post-injury compared to 7 days which was consistent with the fibroblast counts [11]. In our experiment in the rat LD, the H&E images showed more connective tissue at 14 and 28 days post-injury compared to 7 days which was consistent with our experimental fibroblast counts (Figure 4-8, Figure 4-7). Therefore, it is likely that this discrepancy in counts reflects the different muscles used for VML injury. Additional experimental studies that explore a more robust range of fibroblast markers are needed to ensure that the increased trend in fibroblast counts in the rat LD is reflective of increased fibrosis and not PDGFRa marker specific. Currently in the ABM, generalized fibroblast behaviors and development of fibrosis are incorporated (Table 3-1). Future studies that expand upon the current model could incorporate more complex behaviors of fibroblasts, different types of collagen, and behaviors of collagen thickening and scarring to more accurately capture and predict fibrotic changes after VML injury. Based on the fibroblast experimental regional counts, it appears that the discrepancy between model and experiment at 14 and 28 days was a result of differences in the healthy region (Figure 4-10). Expanding the fibroblast behavior in the model may aid in more accurately predicting these fibroblast regional behaviors.

The experimental data of cell counts for the decellularized ECM treated VML injury was the first quantified, temporal data for decellularized ECM treatments and provided additional data to validate our ABM. The SSC experimental counts were similar to ABM predictions; however, the macrophage experimental counts were higher than model predictions (Figure 4-9). The high macrophage counts were consistent with the *in vivo* qualitative observation of a pus bolus forming around day 7 and then disappearing between days 14 and 28. This is indicative of a foreign body response; however, our ABM currently does not have the capability to account for this response which likely explains the discrepancy between experiment and model predictions. Macrophages are currently incorporated in the ABM as a system of ordinary differential equations, which accounts for their counts but does not include their behaviors or interactions with other agents. Expanding the model to include the autonomous behaviors of macrophage agents would provide a platform to model a foreign body response.

Several simplifying assumptions were made in modeling the delivery of exogenous growth factors (Section 3.2.1.1). There was no quantified *in vivo* data demonstrating that IL-10 was successfully delivered to the injury for there was not a significant difference in IL-10 serum levels at day 14 between the decellularized ECM alone and IL-10 and decellularized ECM groups. Yet the experimental counts of myotubes were consistent with model predictions indicating that IL-10 was indeed delivered. Because of the short half-life of IL-10 (1.6 hours), it is likely that we missed collecting serum at a time when IL-10 serum levels were elevated [134]. Additionally, the temporal response of exogenous growth factor delivery could be improved in the model. In the ABM, the full effect of IL-10 on myotube counts is achieved by 14 days post-injury but the experimental data shows that the response is more gradual and the maximum

number of myotubes does not occur until 28 days post-injury (Figure 4-11). Future *in vivo* studies focused on the pharmacokinetics of IL-10 delivery would further improve the accuracy and predictive capabilities of the model.

A circular VML injury was chosen for this experimental study because it can be created *in vivo* with a biopsy punch which improves injury consistency between animals. We used our previously validated FE model of VML injuries (Chapter 2) to determine whether to do *in situ* testing experimentally (Appendix D). A power analysis using the FE model predicted force of treated injuries and the standard deviation of previous *in situ* testing [129] revealed that at least 20 additional rats would need to be tested *in situ* to see statistical difference between unrepaired and decellularized ECM treated VML injuries. The ABM predicted a couple new fibers for the IL-10 and decellularized group, which would have a negligible effect on whole muscle force production [6]. Therefore, *in situ* testing would not show a significant difference between decellularized ECM alone and the IL-10 and decellularized ECM groups and we did not include *in situ* testing in our experiment.

In conclusion, this work demonstrates that computational models can be used to design a novel therapeutic for VML injuries and inform experimental design before testing *in vivo*. Using the ABM (Chapter 3) to design the therapeutic and identify the time points and outcomes in the experimental study saved time and expenses and thus, improved the efficiency of pre-clinical studies. Additionally, we were able to refine the ABM using the experimental data which further improved the ABM's ability to capture cellular dynamics following VML injury. The demonstrated capability of the ABM to accurately predict the therapeutic effect of a scaffold in combination with exogeneous growth factor provides confidence in utilizing the ABM to design

more complex therapeutics, such as cell-seeded biomaterials where simulations could be used to optimize the initial cell density and material's degradability. Coupling the tools of computational modeling and tissue engineering fields has the ability to accelerate the development of more efficacious regenerative therapeutics, and thus, ensure the rapid clinical translation of therapeutics for VML injuries.

Chapter 5

Conclusions

“Let’s go. I’ve had enough waking hours for one day.” – Moira Rose
Schitt’s Creek

5.1 Summary

My goal in this dissertation was to couple the computational modeling and tissue engineering fields to improve the design of therapeutics for VML injuries and accelerate their translation to the clinic. The treatment of VML injuries is challenging because the wound severity, size and location varies widely. Although regenerative medicine is a promising alternative treatment for these injuries, there are no current treatment options that result in complete restoration of muscle form and function. The lack of insight into the mechanisms responsible for the failure of functional regeneration in VML injuries is a major barrier to the development of novel therapeutics for improved functional outcomes. We believed this was an ideal opportunity to use computational models to unravel the complex mechanical and cellular mechanisms in VML injuries that may be difficult to elucidate with only experimental tools and to improve experimental design prior to expensive *in vivo* testing.

First, we built and validated a biomechanical FE model to inform the effect of injury location on *in situ* force production. The coupled framework of *in situ* and *in silico* methods provided new biomechanical insights into force production of VML injuries in a complex muscle architecture. We then focused on cellular mechanisms and built an ABM that predicts tissue regeneration following VML injury. The model allowed us to elucidate the cellular mechanisms contributing to failed muscle regeneration in these injuries and identify targets of future VML therapeutics. Lastly, we used our ABM to inform the design of a novel therapeutic and an experiment that validated the model-derived predictions of the regenerative effect of the therapeutic *in vivo*.

Our coupled experimental-modeling framework provided insight into both mechanical and cellular mechanisms of VML injuries and served as a predictive tool to guide the design of a novel therapeutic for VML injuries and aid in experimental design. The predictive capabilities of our computational models saved hundred of hours of experimental work and animals, thus improving the efficiency of tissue engineering therapeutic development. Moving forward, this coupled framework provides the tools to continue utilizing computational models to accelerate the development of more efficacious regenerative therapeutics and ensure the rapid clinical translation of therapeutics for VML injuries.

5.2 Contributions

5.2.1 FE mechanical model of VML injury for *in situ* testing

I have developed the first FE model of VML injuries to uncover the relationship between injury location and muscle force production. Previous FE models of VML injury had been developed to understand force production in different sized injuries and with treatments in the case of *in vitro* functional testing, where only the longitudinal fibers are constrained [6]. However, my FE model of *in situ* functional testing represents a more physiologically relevant force for all muscle fibers are constrained, consistent with how the latissimus dorsi is anchored *in vivo*. Analysis of FE model simulations revealed that for injuries with identical areas, location can have a dramatic effect on force production. Specifically, injury location affects the percent of injured fibers and this percentage of injured fibers affects how lateral force transmission influences total force production. Our model simulations provided important new

biomechanical insights regarding the relationship between VML injury location and the corresponding force deficits produced in a clinically relevant rodent LD model.

5.2.2 ABM of muscle regeneration following VML injury

I have developed the first computational model to better understand the cellular mechanisms of muscle regeneration in VML injuries. Previous work in our lab developed ABMs of muscle inflammation to study the role of macrophages in healing after laceration injury and of muscle regeneration to probe the effects of different mechanisms of Duchenne muscular dystrophy [61,62], but there is no computational model that has been focused on the cellular mechanisms of regeneration in VML injuries. Few experimental studies have focused on exploring the mechanisms governing regeneration in VML injuries, and there is a need in the field to expand mechanistic knowledge in order to improve the design of therapeutics [10,11]. Our model simulations suggested that multiple overlapping cellular mechanisms are responsible for the overt failure of tissue repair in untreated VML injuries and therapeutics focused on addressing one component will not improve the regenerative response.

5.2.3 Addition of exogenous IL-10 in VML therapeutics

The use of exogenous IL-10 in the treatment of VML injuries was the first application of IL-10 in this injury model. Previous *in vivo* studies have used exogenous IL-10 in the treatment of liver ischemia, renal ischemia, hindlimb ischemia, spinal injuries, stroke, and Chron's disease and a few studies have explored the effect of exogenous IL-10 on macrophage phenotype in muscle regeneration *in vitro* [110,113,138,143–148]. However, to our knowledge, our *in vivo*

study was the first use of exogenous IL-10 in the treatment of VML injuries. The design of our novel therapeutic was informed by ABM simulations, which identified IL-10 as a promising exogenous growth factor to improve SSC differentiation in VML injuries. These model predictions were validated with our experimental data and we observed significantly more terminally differentiated SSCs in injuries treated with exogenous IL-10. These promising results suggest the use of exogenous IL-10 in combination with more complex therapeutics, such as cell-seeded scaffolds which have shown promise in regenerating some fibers, may further improve muscle regeneration and function in the injury.

5.2.4 Coupled experimental-modeling framework

Our novel coupled framework of biomechanical and cellular models with experimental testing optimizes experimental variables and design of therapeutics for VML injuries prior to expensive *in vivo* studies. Experimental *in vivo* studies are time consuming and resource intensive but by coupling experimental work with computational models hundreds of hours of experimental work and animals can be saved. The ABM provides tissue regeneration predictions of the proposed therapeutic and then the ABM prediction of muscle regeneration can be simulated in the FE model to predict the functional response. This feedback loop can continue until the preferred experimental variables have been identified and then can be validated experimentally. Additionally, the computational models can be used to interpret and understand experimental results. We have demonstrated the utility of computational models in informing therapeutic design (Chapter 3, 4) as well as informing experimental variables, such as injury location, injury size, time points, group sizes and assays to include (Chapter 2, 4).

Coupling the tools of computational modeling and tissue engineering fields can accelerate the development of more efficacious regenerative therapeutics, and thus, ensure the rapid clinical translation of therapeutics for VML injuries.

5.3 Future applications

The goal of this dissertation was to combine the tools of the computational and tissue engineering fields to improve the efficiency and efficacy of novel therapeutics. The work presented in this dissertation has developed the foundation for using an experimental-modeling coupled framework to improve the design of therapeutics for VML injuries. The next steps include expanding the muscles modeled, incorporating expanded cellular behaviors in the ABM, and follow up experimental studies to provide additional insight into mechanisms specific to VML injuries. The long-term goal of this coupled framework is to design injury specific treatment options to improve patient outcomes following VML injury.

5.3.1 Future modeling work to study VML injuries

Finite-element models

VML injuries are challenging to treat because the wound severity, size and location varies widely. The FE model developed in this work was of the rat LD, which has a complex muscle architecture of parallel and pennate fibers (Chapter 2). Expanding to FE models of other muscles, such as the tibialis anterior (TA) which is composed of parallel fibers, will provide mechanical insight into additional injury environments. The FE models can be used to predict

anticipated functional outcomes of specific VML injuries in other *in vivo* experimental studies and identify the preferred experimental injury location in a given muscle to increase the margin of difference between isometric force produced in intact and VML injured muscles, providing a more favorable condition for evaluating treatment effects. Additionally, biomechanical insight into the relationship between muscle environment and the corresponding force deficits can eventually be used to guide injury specific treatment options. This computational tool will have the ability to capture the intrinsic variability of VML injuries and ensure improved functional outcomes for patients.

Agent-based models

The ABM developed in this work captures the regenerative response of unrepaired and treated VML injuries; however, simplifying assumptions were made when developing the model (Chapter 3). Specifically, the fibroblast behavior included in the ABM is a simplified representation of fibroblast and collagen behaviors and we did not incorporate collagen subtypes into this ABM. Expanding fibroblast behavior in the ABM to include more specifics about the effect of the mechanical environment, collagen subtypes, and development of fibrosis would likely allow the model to more accurately model anti-fibrotic therapies. Fibrosis is an important aspect of the tissue response following VML injury and impairing or slowing down its development, in combination with other treatments, would aid in improving muscle regeneration [10,11,81,82,149]. Thus, an important next step in utilizing this ABM for the design of more complex therapeutics is to expand the modeling of fibroblast behavior.

It is known that the pro-inflammatory presence following VML injuries is an important aspect of the tissue response, and we incorporated inflammatory cells in our ABM through a system of ordinary differential equations (Chapter 3). This allowed us to capture their cell counts and the effect of their counts on the behavior of other agents. However, our *in vivo* data of pro-inflammatory macrophages showed higher counts with a treatment of decellularized ECM than in unrepaired injuries suggesting that there was an inflammatory response to the treatment (Chapter 4). Although decellularized ECM is not believed to elicit an inflammatory response, our experimental data at time points less than 28 days reveal that may not be the case. Currently, the ABM does not have the ability to capture the interactions of macrophages with ECM for autonomous behaviors are not incorporated in the model. Expanding the model to incorporate macrophage behaviors and interactions would improve the predictive capabilities of the ABM in therapeutic design. For example, to use the model to tune biomaterials that have the ability to attenuate inflammatory cells, it would be crucial to have macrophage autonomous behaviors incorporated in the ABM to accurately predict their effect on regeneration in VML injuries.

Moving forward, the ABM can be used to simulate and design complex therapeutics. The model has the capability to simulate biomaterials with varying collagen composition or degradation. Previous experimental studies have demonstrated the utility of cell-seeded therapeutics for VML injuries, and the ABM can aid in designing these therapies which would limit the number of experiments that would need to be conducted. Using model perturbations, the preferred population of cells to seed and the initial cell density for the therapeutic could be optimized. If the cell composition of the therapeutic is known, then that could be imported into

the model and the regenerative effect simulated. Additionally, the administration of exogenous growth factors in combination with a cell-seeded scaffold could be explored. For example, a novel therapeutic consisting of decellularized ECM seeded with muscle progenitor cells in combination with IL-10 was simulated and showed a significant increase in muscle regeneration, marked by the number of fully differentiated SSCs (myotubes) and number of new fibers (Figure 5-1).

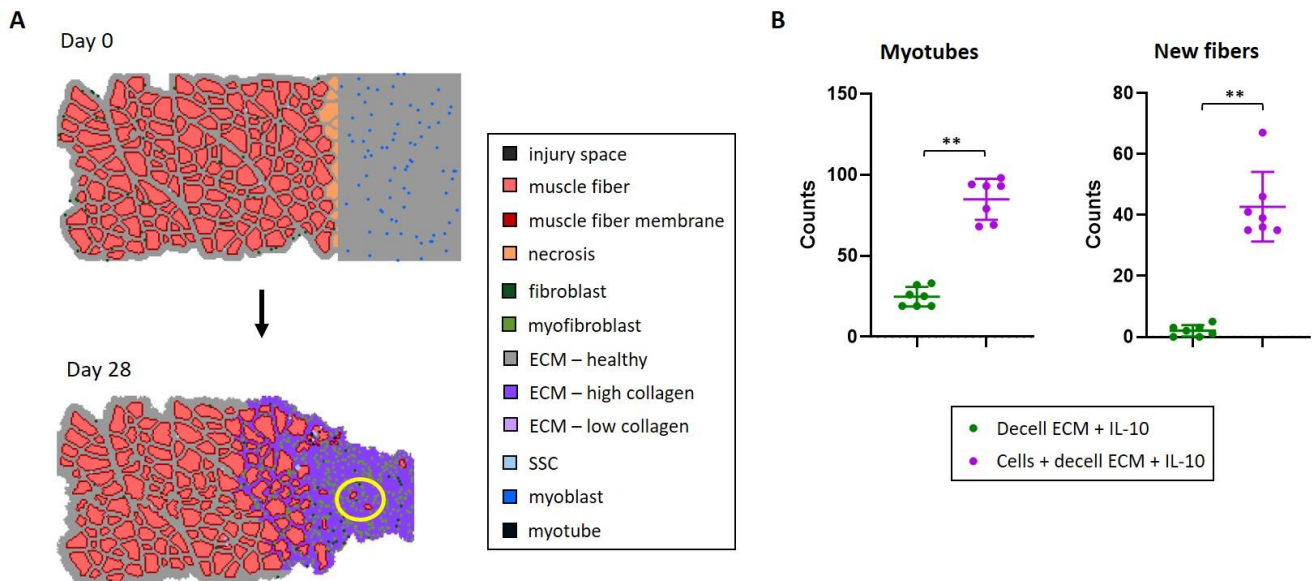


Figure 5-1. ABM simulations of exogenous IL-10 in combination with cell-seeded decellularized ECM and decellularized ECM treated VML injuries. Example therapeutic of ABM simulation with muscle progenitor cells seeded at 2×10^4 cells/cm² on decellularized ECM at day 0 and then day 28 (A). The yellow circle is highlighting new, small fibers present in the injury defect. The cell-seeded decellularized ECM with IL-10 treatment predicted significantly more myotubes and new fibers compared to decellularized ECM with IL-10. Model results reported as mean \pm standard deviation. ** $p < 0.05$

5.3.2 Future experimental work to study VML mechanisms of regeneration

Comparison of our experimental fibroblast data of unrepaired VML injuries in the LD compared to unrepaired injuries in the TA reveals that there may be differences in fibrosis development depending on the muscle (Chapter 4). To date, a handful of studies have examined the mechanisms of fibroblast development in VML injuries and it has not been compared across injury models [10,11,23,149]. The first step is an *in vivo* study of VML injuries in the rat LD examining a range of fibrosis markers to ensure that the temporal behavior of the PDGFR α marker is consistent with other fibroblast markers. Then FE models of the rat LD and TA can be used to explore mechanical differences in each injury environment. Based on the mechanical insight, a follow up experimental study can be performed to identify if differences in fibrosis development are a result of the mechanical environment or a biological difference between muscles. If there are mechanical and/or biological differences, new therapeutics could be tested computationally in each environment using the FE and ABM models to determine the environment where a therapeutic would be most effective. This could eventually lead to injury specific treatment options.

Follow up *in vivo* studies are needed to tune the pharmacokinetics of growth-factor delivery subcutaneously for VML injuries. The ABM prediction of the regenerative effect of exogenous IL-10 in VML injuries was validated *in vivo*, although there was a difference in the temporal response (Chapter 4). In the ABM, SSCs differentiated to myotubes with exogenous IL-10 at a faster rate than was measured experimentally. An *in vivo* study measuring serum levels of IL-10 consistently over the 7 days of subcutaneous delivery would allow the ABM implementation of growth factor delivery to be tuned to capture experimental measurements.

Additionally, a dose sensitivity analysis of IL-10 *in vivo* would provide data to validate the sensitivity of IL-10 in the model and to correlate experimental dosing of IL-10 to levels of administered IL-10 in the ABM.

The administration of exogenous IL-10 in VML injuries had an encouraging effect on the regenerative response in VML injuries (Chapter 4). Although the regenerative effect of IL-10 alone was not significant enough to replace all lost fibers and alter the functional response, incorporating exogenous IL-10 with more complex therapeutics may result in significant muscle tissue regeneration and a functional improvement. ABM simulations reveal that the incorporation of cells with the decellularized ECM and IL-10 would further improve the regenerative response (Figure 5-1). A follow up experimental-modeling coupled study would provide insight into the further utility of IL-10 in complex therapeutics. The ABM can be used to predict the muscle tissue response from the therapeutics and determine the optimal design of the cell-seeded therapeutic, and the FE model can be used to predict the potential functional effect of this therapeutic and identify optimal experimental variables. Informed by the computational models, an *in vivo* study can be done to assess the regenerative effect of exogenous IL-10 in combination with cell-seeded therapeutics.

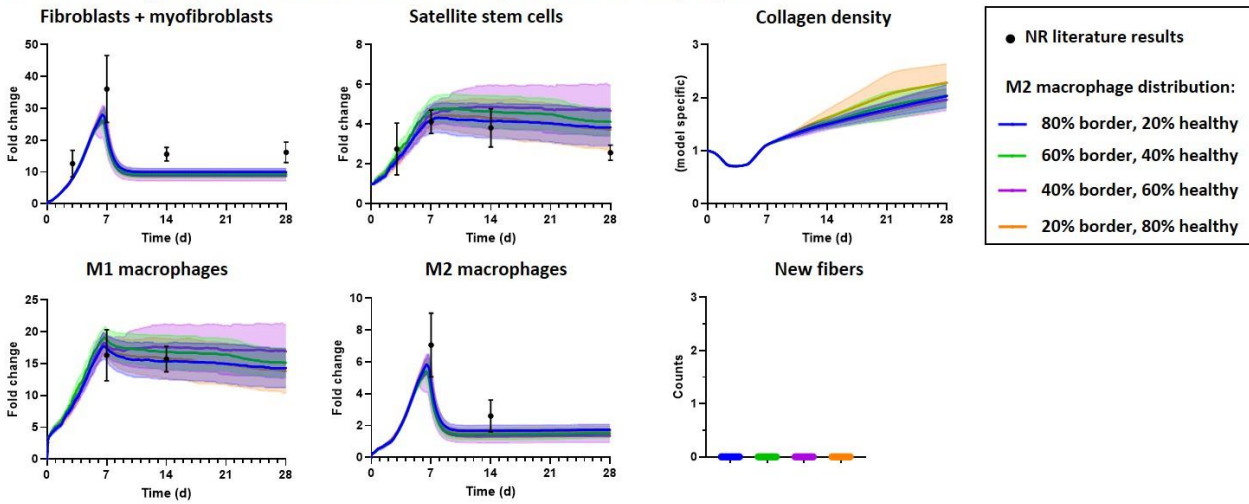
5.4 Final remarks

In VML injuries, the intrinsic regenerative process of skeletal muscle fails and results in functional impairment. These injuries are especially common in servicemembers and there are currently no clinical treatments that result in complete restoration of tissue and function. Regenerative medicine approaches are a promising alternative treatment, but their development is limited by the poor understanding of mechanical and cellular mechanisms in VML injuries. I believed this was the ideal opportunity to couple experimental and computational modeling tools to improve the design of preclinical therapeutics and aid in experimental design. In this dissertation, I have developed mechanical and physiology-based *in silico* models to unravel the complex mechanical and cellular mechanisms resulting in failed muscle regeneration in VML injuries. The insight from the ABM informed a novel therapeutic design and both of these models improved the efficiency of our *in vivo* studies. I have demonstrated the utility of an experimental-modeling coupled framework and believe that the coupling of FE models and ABMs offers a unique ability to predict the functional and tissue regeneration effects of a new regenerative therapeutic. In the future, this framework can continue to accelerate the development of more efficacious therapeutics and ensure the rapid clinical translations of regenerative therapeutics for VML injuries.

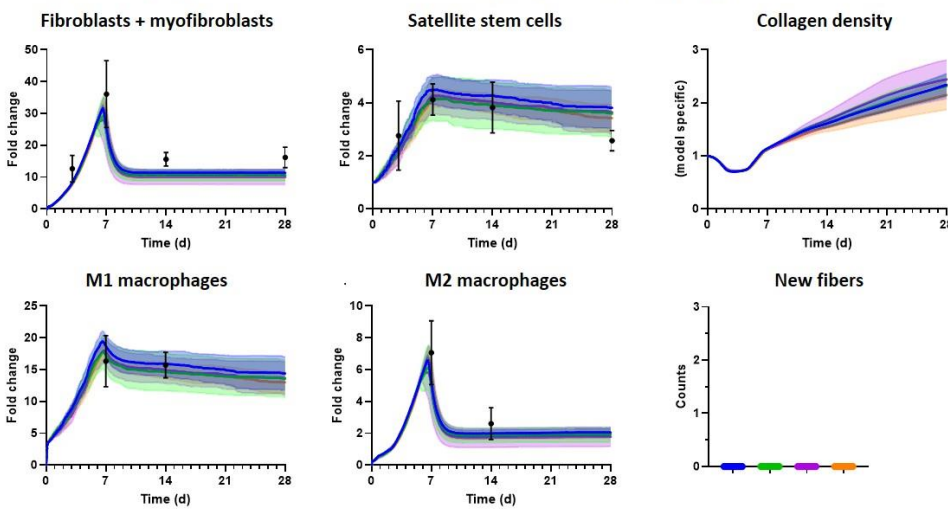
Appendix A: Perturbations of M1 and M2 macrophages regional distributions

There was limited quantified data available in the literature describing the regional distribution of M1 and M2 macrophages. The Goldman et al. 2018 experimental study quantified the spatial distribution of a pan-macrophage marker which we incorporated in the ABM as an assumption of 60% of macrophages in the border region and 40% in the healthy region [78]. We varied the distribution of M1 and M2 macrophages in each region to determine its effect on the model outputs. For each M1 macrophage distribution (80% border + 20% healthy regions vs 60% border + 40% healthy regions vs 40% border + 60% healthy region), the M2 macrophage distribution was varied (Figure A-1). There were no significant differences in fibroblast, SSC, or macrophage fold changes. These model simulations suggest that the distribution of macrophages does not alter the development of fibrotic tissue, marked by collagen density, nor the regenerative response, marked by the number of new fibers.

A M1 macrophage distribution: 80% border region, 20% healthy region



B M1 macrophage distribution: 60% border region, 40% healthy region



C M1 macrophage distribution: 40% border region, 60% healthy region

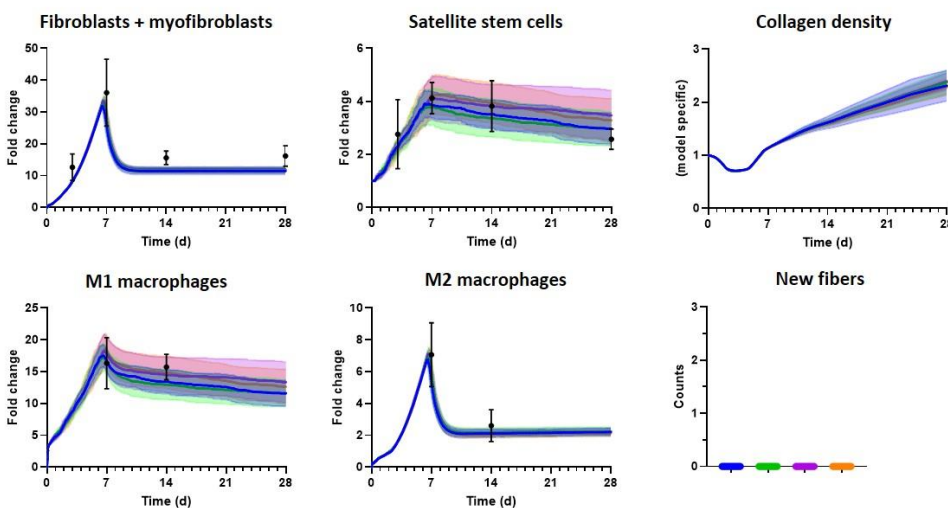


Figure A-1. Varying the distribution of M1 and M2 macrophages did not alter the fibrotic nor regenerative response of VML injuries. M1 macrophage distributions of 80% border region (20% healthy), 60% border region (40% healthy), and 40% border region (60% healthy) were tested. For each M1 distribution, M2 macrophage distributions of 80% border region (20% healthy), 60% border region (40% healthy), 40% border region (60% healthy), and 20% border region (80% healthy) were simulated. Fibroblast, SSC, and macrophage fold changes, collagen density, and counts of new, regenerated fibers were predicted. Model results reported as mean \pm 95% confidence interval.

Appendix B: Perturbations of decellularized ECM structure

Perturbations varying the structure of the decellularized ECM treatment were performed to determine if the treatment structure significantly altered the regenerative response. Five different decellularized ECM treatments were simulated – (i) ECM filling the defect, (ii) layers 60 μm thick ECM filling the defect, (iii) layers 10 μm thick ECM filling the defect, (iv) 4 layers of 60 μm thick ECM, and (v) 4 layers of 10 μm thick ECM (Figure B-1A). The decellularized ECM thickness of 60 μm and 10 μm corresponds to different sources of swine bladders used to produce the decellularized ECM in the Christ Lab. Previous experimental studies in the Christ Lab have implanted 4 layers of decellularized ECM [6–8]. Focusing specifically on the cell type which directly determines the regenerative response, the different ECM structures did not significantly affect the fold change of SSCs (Figure B-1B). It might be expected that ECM structure would affect the behavior of SSCs because the microenvironment is known to affect SSC proliferation and differentiation (Table 3-2). Looking at the location of SSCs in the border region, there were no significant differences in the number of SSCs on injured fibers nor on ECM ready to generate a new fiber. Therefore, the model simulations suggest that decellularized ECM structure does not significantly alter the regenerative response of VML injuries.

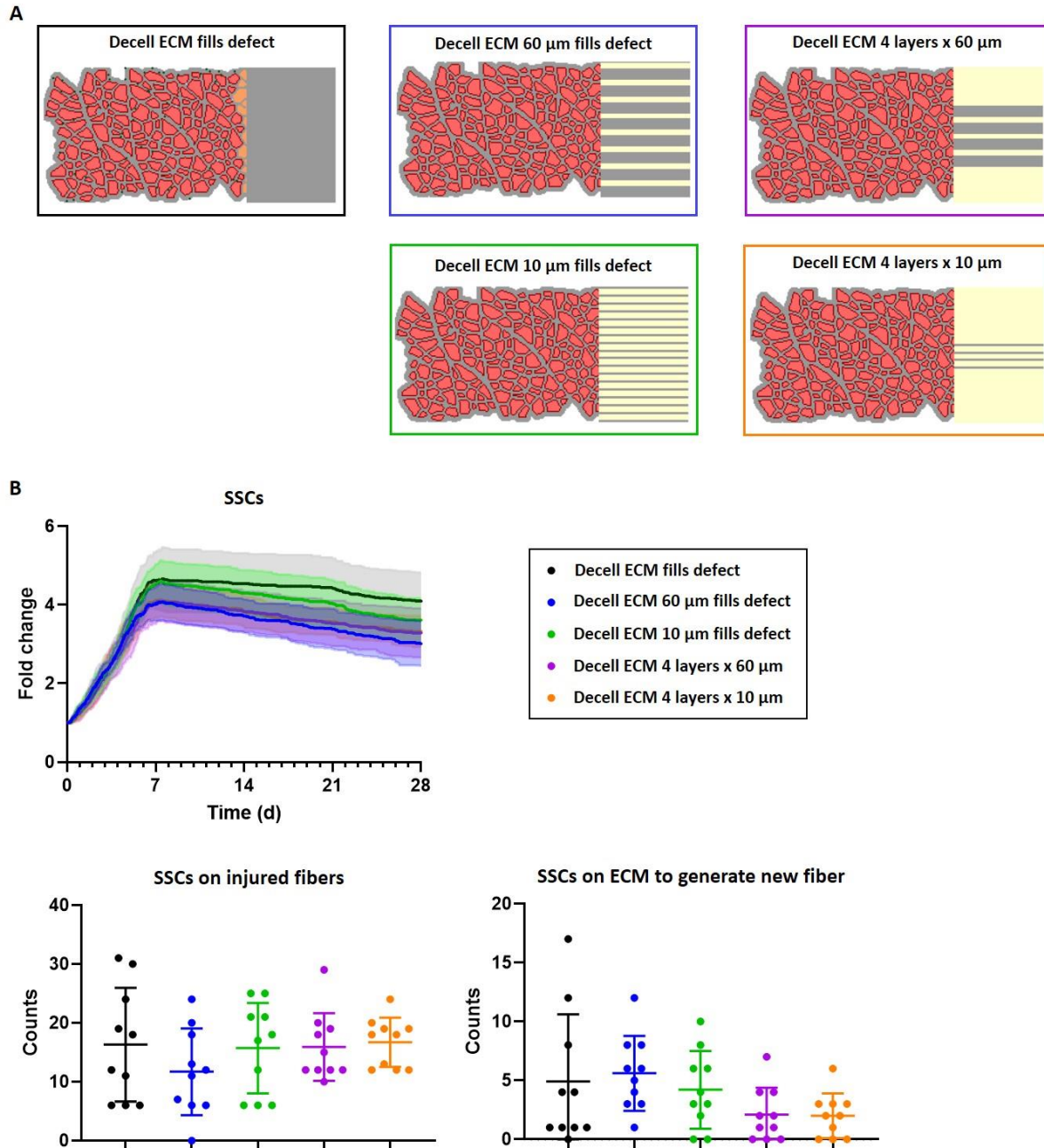


Figure B-1. Perturbations of decellularized ECM structure did not significantly alter the behaviors of SSCs. Five different structures of decellularized ECM (shown in gray) were simulated (A). The SSC fold change was not changed by ECM structure and the location of SSCs in the border region with each ECM treatment was not significantly different (B). The different ECM structures did not significantly affect the fibroblast and macrophage fold changes (plots not shown). Model results of SSC fold change reported as mean \pm 95% confidence interval. Model counts of SSC location (on injured fiber, on ECM to generate new fiber) reported as mean \pm standard deviation.

Appendix C: Parameterization of SSC differentiation max chance

The maximum probability of SSC differentiation was one of the unknown model parameters tuned in Chapter 3. When initialing building the ABM, there was no experimental data of myotube counts in unrepaired injuries available and thus, it was challenging to tune that parameter. Now in Chapter 4, we have experimental myotube counts available to help us further tune the unrepaired ABM. Varying the value of the maximum probability of SSC differentiation per hour reveals that it does not aid in capturing the few myotubes measured experimentally in unrepaired VML injuries (Figure C-1). The maximum probability of SSC differentiation per hour remained at 1/15 (0.0666).

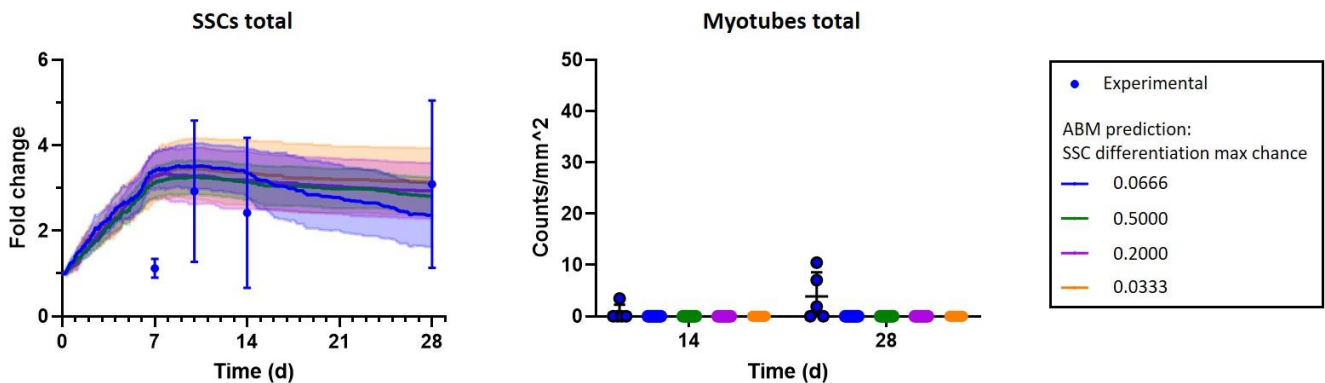


Figure C-1. Comparison of ABM predictions and *in vivo* experimental data of SSCs and myotubes for unrepaired VML injuries. In Chapter 3, the maximum probability of SSC differentiation per hour was determined to be 1/15 (blue). Varying the SSC differentiation max chance in the ABM did not significantly affect the total counts of SSCs or myotubes. Re-parameterization of this parameter was unable to recapitulate the experimental data of myotubes.

Appendix D: FE model predictions of circular injury

As described in detail in Chapter 2, a three-dimensional FE model of a rat latissimus dorsi (LD) was created and *in situ* experimental testing conditions were simulated [54]. In total, nine different injury models were created (Figure D-1B). To analyze the effect of size, unrepaired circular injuries with 14.5 mm, 12 mm, and 8 mm diameters were tested with the injury 10 mm from the cranial edge of the LD. To analyze the effect of location, 12 mm diameter circular injuries were created in the middle of the rectangular portion of the LD (Model I), at the very caudal edge (Model II), at the far side of the muscle (Model III), and near the cranial edge (Model V). To analyze the effect of a decellularized ECM treatment, the injury space was filled with a passive material assuming a vertical fiber trajectory and using previously determined material parameters [6]. The injury was 12 mm in diameter and near the cranial edge of the LD (Model V). Three different treatment models were tested representing if the treatment filled 15%, 50% or 100% of the thickness of the muscle. Muscle activation levels were set at the maximum activation for all trials to simulate maximum tetanic force. Total force of the modeled LD was measured in the y-direction on the cranial rectangular surface in the x-z plane.

With the VML injury 10 mm from the cranial edge of the LD, the force deficit from intact muscle increased with increasing circle diameter (Figure D-1A). A 14.5 mm diameter circular injury created the largest force deficit from intact, and this model isometric force prediction was 49% lower than an intact LD (Figure D-1A). However, the largest biopsy punch available for *in vivo* experiments was a 12 mm diameter and that injury size was chosen for additional FE model predictions. Then the injury location of a 12 mm circular injury was varied to determine the preferred location for the experiment. A similar trend was seen in force predictions of a

circular injury compared to a rectangular injury (Chapter 2). A caudal injury location (Model II) generated a force value closest to an intact muscle, and a cranial injury location (Model V) created the largest force deficit from intact at 36% lower (Figure D-1A). The larger force deficit from an intact LD provides a larger margin to see treatment effects on force production, and thus a cranial injury location was chosen for additional FE models. In the third set of FE model predictions, a decellularized ECM treatment in the VML injury was simulated. The thickness of the decellularized ECM was modeled at 15%, 50%, and 100% filling of the thickness of the muscle (z-direction). Increasing the thickness of the ECM treatment resulted in increased force predictions, consistent with previously published FE models (Figure D-1A) [6].

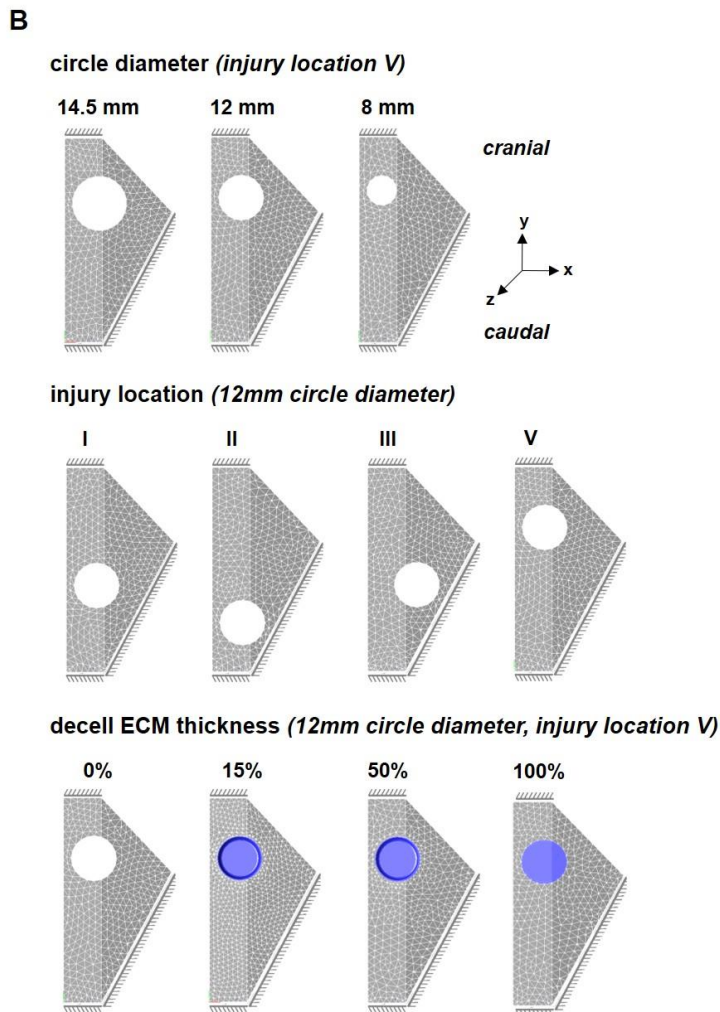
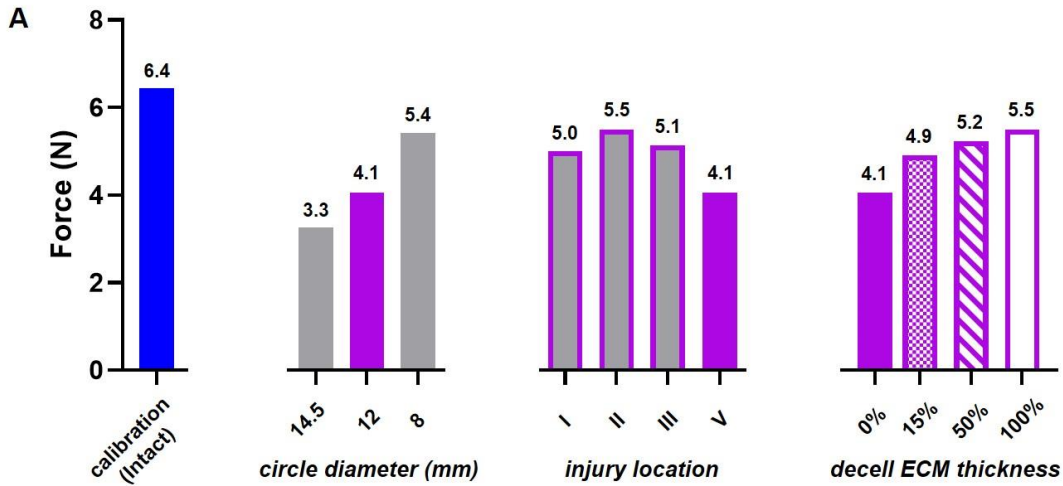


Figure D-1. FE model isometric force predictions of injury size, location, and treatment informed experimental design (A). A sensitivity analysis of circular injury diameter and injury location found that a found that a 12 mm diameter cranial injury location generated the smallest force value compared to an intact LD. With the informed 12 mm diameter and location V injury, a treatment of decellularized ECM was simulated and increasing the thickness of the treatment increased the isometric force predictions. Three-dimensional FE models of the rat LD for the analysis of injury diameter, location, and treatment were constrained as shown along the cranial rectangular edge and caudal rectangular and triangular edges with the elements (B). Decellularized (decell) ECM thickness was modeled as the percent filling of the muscle thickness in the z-direction.

References

1. Corona BT, Rivera JC, Owens JG, Wenke JC, Rathbone CR. Volumetric muscle loss leads to permanent disability following extremity trauma. *J Rehabil Res Dev* 2015; 52.
2. Grogan BF, Hsu JR. Volumetric muscle loss. *J Am Acad Orthop Surg* 2011; 19:S35–S37.
3. Garg K, Ward CL, Rathbone CR, Corona BT. Transplantation of devitalized muscle scaffolds is insufficient for appreciable de novo muscle fiber regeneration after volumetric muscle loss injury. *Cell Tissue Res* 2014; 358:857–873.
4. Aurora A, Roe JL, Corona BT, Walters TJ. An acellular biologic scaffold does not regenerate appreciable de novo muscle tissue in rat models of volumetric muscle loss injury. *Biomaterials* 2015; 67:393–407.
5. Corona BT, Wu X, Ward CL, McDaniel JS, Rathbone CR, *et al.* The promotion of a functional fibrosis in skeletal muscle with volumetric muscle loss injury following the transplantation of muscle-ECM. *Biomaterials* 2013; 34:3324–3335.
6. Passipieri JA, Hu X, Mintz E, Dienes J, Baker HB, *et al.* In Silico and In Vivo Studies Detect Functional Repair Mechanisms in a Volumetric Muscle Loss Injury. *Tissue Eng Part A* 2019; 25:1272–1288.
7. Mintz EL, Passipieri JA, Franklin IR, Toscano VM, Afferton EC, *et al.* Long-Term Evaluation of Functional Outcomes Following Rat Volumetric Muscle Loss Injury and Repair. *Tissue Eng Part A* 2019; :1–48.
8. Corona BT, Ward CL, Baker HB, Walters TJ, Christ GJ. Implantation of In Vitro Tissue Engineered Muscle Repair Constructs and Bladder Acellular Matrices Partially Restore In Vivo Skeletal Muscle Function in a Rat Model of Volumetric Muscle Loss Injury. *Tissue*

- Eng Part A* 2013; 20:705–715.
9. Corona BT, Machingal MA, Criswell T, Vadhavkar M, Dannahower AC, *et al.* Further Development of a Tissue Engineered Muscle Repair Construct *In Vitro* for Enhanced Functional Recovery Following Implantation *In Vivo* in a Murine Model of Volumetric Muscle Loss Injury. *Tissue Eng Part A* 2012; 18:1213–1228.
 10. Garg K, Corona BT, Walters TJ. Therapeutic strategies for preventing skeletal muscle fibrosis after injury. *Front Pharmacol* 2015; 6.
 11. Aguilar CA, Greising SM, Watts A, Goldman SM, Peragallo C, *et al.* Multiscale analysis of a regenerative therapy for treatment of volumetric muscle loss injury. *Cell Death Discov* 2018; 4.
 12. Corona BT, Wenke JC, Ward CL. Pathophysiology of volumetric muscle loss injury. *Cells Tissues Organs* 2016; 202:180–188.
 13. Greising SM, Rivera JC, Goldman SM, Watts A, Aguilar CA, *et al.* Unwavering Pathobiology of Volumetric Muscle Loss Injury. *Sci Rep* 2017; 7:1–14.
 14. Wu X, Corona BT, Chen X, Walters TJ. A Standardized Rat Model of Volumetric Muscle Loss Injury for the Development of Tissue Engineering Therapies. *Biores Open Access* 2012; 1:280–290.
 15. Baker HB, Passipieri JA, Siriwardane M, Ellenburg MD, Vadhavkar M, *et al.* Cell and Growth Factor-Loaded Keratin Hydrogels for Treatment of Volumetric Muscle Loss in a Mouse Model. *Tissue Eng Part A* 2017; 23:572–584.
 16. Chen XK, Walters TJ. Muscle-derived decellularised extracellular matrix improves functional recovery in a rat latissimus dorsi muscle defect model. *J Plast Reconstr*

- Aesthetic Surg* 2013; 66:1750–1758.
17. Corona BT, Rivera JC, Wenke JC, Greising SM. Tacrolimus as an adjunct to autologous minced muscle grafts for the repair of a volumetric muscle loss injury. *J Exp Orthop* 2017; 4:36.
 18. Chargé SB, Rudnicki MA. Cellular and molecular regulation of muscle regeneration. *Physiol Rev* 2004; 84:209–238.
 19. Tidball JG, Villalta SA. Regulatory interactions between muscle and the immune system during muscle regeneration. *Am J Physiol Regul Integr Comp Physiol* 2010; 298:R1173-87.
 20. Passipieri JA, Christ GJ. The potential of combination therapeutics for more complete repair of volumetric muscle loss injuries: The role of exogenous growth factors and/or progenitor cells in implantable skeletal muscle tissue engineering technologies. *Cells Tissues Organs* 2016; 202:202–213.
 21. Karalaki M, Fili S, Philippou A, Koutsilieris M. Muscle regeneration: cellular and molecular events. *In Vivo* 2009; 23:779–96.
 22. Carlson BM, Faulkner JA. The regeneration of skeletal muscle fibers following injury: a review. *Med. Sci. Sports Exerc.* 1983; 15:187–198.
 23. Garg K, Ward CL, Corona BT. Asynchronous inflammation and myogenic cell migration limit muscle tissue regeneration mediated by cellular scaffolds. *Inflamm Cell Signal* 2014; 1.
 24. Christ GJ, Saul JM, Furth ME, Andersson K-E. The Pharmacology of Regenerative Medicine. *Pharmacol Rev* 2013; 65:1091–1133.
 25. Corona BT, Greising SM. Challenges to acellular biological scaffold mediated skeletal

- muscle tissue regeneration. *Biomaterials* 2016; 104:238–246.
26. Grasman JM, Zayas MJ, Page RL, Pins GD. Biomimetic scaffolds for regeneration of volumetric muscle loss in skeletal muscle injuries. *Acta Biomater* 2015; 25:2–15.
 27. Heredia J, Mukundan L, Chen F, Mueller A, Deo R, *et al.* Type 2 Innate Signals Stimulate Fibro/Adipogenic Progenitors to Facilitate Muscle Regeneration. *Cell* 2013; 153:376–388.
 28. Zhao BL, Kollias HD, Wagner KR. Myostatin directly regulates skeletal muscle fibrosis. *J Biol Chem* 2008; 283:19371–19378.
 29. Fischer A. A Functional Study of Cell Division in Cultures of Fibroblasts. *J Cancer Res* 1925; :50–61.
 30. Serrano AL, Muñoz-Cánoves P. Regulation and dysregulation of fibrosis in skeletal muscle. *Exp Cell Res* 2010; 316:3050–3058.
 31. Aurora A, Corona BT, Walters TJ. A porcine urinary bladder matrix does not recapitulate the spatiotemporal macrophage response of muscle regeneration after volumetric muscle loss injury. *Cells Tissues Organs* 2016; 202:189–201.
 32. Ihn H, Yamane K, Kubo M, Tamaki K. Blockade of endogenous transforming growth factor b signaling prevents up-regulated collagen synthesis in scleroderma fibroblasts. *Arthritis Rheum* 2001; 44:474–480.
 33. Perrone C, Fenwick-Smith D, Vandeburgh H. Collagen and Stretch Modulate Autocrine Secretion of Insulin-Like Growth Factor-I and Insulin-Like Growth Factor Binding Proteins from Differentiated Skeletal Muscle Cells. *J Biol Chem* 1995; 270:2099–2106.
 34. Skutek M, Van Griensven M, Zeichen J, Brauer N, Bosch U. Cyclic mechanical stretching modulates secretion pattern of growth factors in human tendon fibroblasts. *Eur J Appl*

- Physiol* 2001; 86:48–52.
35. Petrov V V., Fagard RH, Lijnen PJ. Stimulation of collagen production by transforming growth factor- β 1 during differentiation of cardiac fibroblasts to myofibroblasts. *Hypertension* 2002; 39:258–263.
 36. Joe AWB, Yi L, Natarajan A, Le Grand F, So L, *et al.* Muscle injury activates resident fibro/adipogenic progenitors that facilitate myogenesis. *Nat Cell Biol* 2010; 12:153–163.
 37. Zanotti S, Gibertini S, Mora M. Altered production of extra-cellular matrix components by muscle-derived Duchenne muscular dystrophy fibroblasts before and after TGF- β 1 treatment. *Cell Tissue Res* 2010; 339:397–410.
 38. Igotz RA, Massague J. Transforming Growth Factor-Beta Stimulates the Expression of Fibronectin and Collagen and Their Incorporation into the Extracellular Matrix. *J Biol Chem* 1986; 261:4337–4345.
 39. Kühl U, Timpl R, von der Mark K. Synthesis of type IV collagen and laminin in cultures of skeletal muscle cells and their assembly on the surface of myotubes. *Dev Biol* 1982; 93:344–354.
 40. Syverud BC, VanDusen KW, Larkin LM. Growth factors for skeletal muscle tissue engineering. *Cells Tissues Organs* 2016; 202:169–179.
 41. Cooper RN, Tajbakhsh S, Mouly V, Cossu G, Buckingham M, *et al.* In vivo satellite cell activation via Myf5 and MyoD in regenerating mouse skeletal muscle. *J Cell Sci* 1999; 112:2895–2901.
 42. Tatsumi R, Anderson JE, Nevoret CJ, Halevy O, Allen RE. HGF/SF is present in normal adult skeletal muscle and is capable of activating satellite cells. *Dev Biol* 1998; 194:114–128.

43. Tatsumi R, Sheehan SM, Iwasaki H, Hattori A, Allen RE. Mechanical stretch induces activation of skeletal muscle satellite cells in vitro. *Exp Cell Res* 2001; 267:107–114.
44. Siegel AL, Atchison K, Fisher KE, Davis GE, Cornelison DDW. 3D timelapse analysis of muscle satellite cell motility. *Stem Cells* 2009; 27:2527–2538.
45. Allen RE, Boxhorn LK. Regulation of skeletal muscle satellite cell proliferation and differentiation by transforming growth factor-beta, insulin-like growth factor I, and fibroblast growth factor. *J Cell Physiol* 1989; 138:311–315.
46. Rullman E, Norrbom J, Stromberg A, Wagsater D, Rundqvist H, *et al.* Endurance exercise activates matrix metalloproteinases in human skeletal muscle. *J Appl Physiol* 2009; 106:804–812.
47. Cornelison DDW, Filla MS, Stanley HM, Rapraeger AC, Olwin BB. Syndecan-3 and syndecan-4 specifically mark skeletal muscle satellite cells and are implicated in satellite cell maintenance and muscle regeneration. *Dev Biol* 2001; 239:79–94.
48. Pavlath GK, Dominov JA, Kegley KM, Millert JB. Regeneration of transgenic skeletal muscles with altered timing of expression of the basic helix-loop-helix muscle regulatory factor MRF4. *Am J Pathol* 2003; 162:1685–1691.
49. Megeney LA, Rudnicki MA, Kablar B, Garrett K, Anderson JE, *et al.* MyoD is required for myogenic stem cell function in adult skeletal muscle. *Genes Dev* 1996; 10:1173–83.
50. Cornelison DDW, Olwin BB, Rudnicki MA, Wold BJ. MyoD(-/-) satellite cells in single-fiber culture are differentiation defective and MRF4 deficient. *Dev Biol* 2000; 224:122–137.
51. Yoshida N, Yoshida S, Koishi K, Masuda K, Nabeshima Y. Cell heterogeneity upon myogenic differentiation: down-regulation of MyoD and Myf-5 generates “reserve cells.”

- J Cell Sci* 1998; 111:769–779.
52. Gayraud-Morel B, Chretien F, Jory A, Sambasivan R, Negroni E, *et al.* Myf5 haploinsufficiency reveals distinct cell fate potentials for adult skeletal muscle stem cells. *J Cell Sci* 2012; 125:1738–1749.
 53. Kuang S, Kuroda K, Le Grand F, Rudnicki MA. Asymmetric Self-Renewal and Commitment of Satellite Stem Cells in Muscle. *Cell* 2007; 129:999–1010.
 54. Blemker SS, Pinsky PM, Delp SL. A 3D model of muscle reveals the causes of nonuniform strains in the biceps brachii. *J Biomech* 2005; 38:657–665.
 55. Martins JAC, Pato MPM, Pires EB, Jorge RMN, Parente M, *et al.* Finite Element Studies of the Deformation of the Pelvic Floor. *Ann N Y Acad Sci* 2007; 1101:316–334.
 56. Rehorn MR, Blemker SS. The effects of aponeurosis geometry on strain injury susceptibility explored with a 3D muscle model. *J Biomech* 2010; 43:2574–2581.
 57. Inouye JM, Pelland K, Lin KY, Borowitz KC, Blemker SS. A Computational Model of Velopharyngeal Closure for Simulating Cleft Palate Repair. *J Craniofac Surg* 2015; 26:658–662.
 58. Sharafi B, Blemker SS. A mathematical model of force transmission from intrafascicularly terminating muscle fibers. *J Biomech* 2011; 44:2031–2039.
 59. Virgilio KM, Martin KS, Peirce SM, Blemker SS. Multiscale models of skeletal muscle reveal the complex effects of muscular dystrophy on tissue mechanics and damage susceptibility. *Interface Focus* 2015; 5:20140080.
 60. Martin KS, Blemker SS, Peirce SM. Agent-based computational model investigates muscle-specific responses to disuse-induced atrophy. *J Appl Physiol* 2015; 118:1299–

1309.

61. Martin KS, Kegelman CD, Virgilio KM, Passipieri JA, Christ GJ, *et al.* In Silico and In Vivo Experiments Reveal M-CSF Injections Accelerate Regeneration Following Muscle Laceration. *Ann Biomed Eng* 2016; 45:747–760.
62. Virgilio KM, Martin KS, Peirce SM, Blemker SS. Agent-based model illustrates the role of the microenvironment in regeneration in healthy and mdx skeletal muscle. *J Appl Physiol* 2018; 125:1424–1439.
63. Quarta M, Cromie M, Chacon R, Blonigan J, Garcia V, *et al.* Bioengineered constructs combined with exercise enhance stem cell-mediated treatment of volumetric muscle loss. *Nat Commun* 2017; 8. doi:10.1038/ncomms15613
64. Passipieri JA, Baker HB, Siriwardane M, Ellenburg MD, Vadhavkar M, *et al.* Keratin Hydrogel Enhances *In Vivo* Skeletal Muscle Function in a Rat Model of Volumetric Muscle Loss. *Tissue Eng Part A* 2017; 23:556–571.
65. Christ GJ, Siriwardane M, De Coppi P. Engineering muscle tissue for the fetus: Getting ready for a strong life. *Front Pharmacol* 2015; 6:1–11.
66. Zajac FE. Muscle and tendon: properties, models, scaling, and application to biomechanics and motor control. *Crit. Rev. Biomed. Eng.* 1989; 17:359–411.
67. Street SF. Lateral transmission of tension in frog myofibers: A myofibrillar network and transverse cytoskeletal connections are possible transmitters. *J Cell Physiol* 1983; 114:346–364.
68. Huijing PA, Baan GC, Rebel GT. Non-myotendinous force transmission in rat extensor digitorum longus muscle. *J Exp Biol* 1998; 201:683–691.

69. Jaspers RT, Brunner R, Pel JJM, Huijing PA. Acute effects of intramuscular aponeurotomy on rat gastrocnemius medialis: Force transmission, muscle force and sarcomere length. *J Biomech* 1999; 32:71–79.
70. Yucesoy CA, Koopman BHFJM, Huijing PA, Grootenboer HJ. Three-dimensional finite element modeling of skeletal muscle using a two-domain approach: Linked fiber-matrix mesh model. *J Biomech* 2002; 35:1253–1262.
71. Yucesoy CA, Koopman BHFJM, Baan GC, Grootenboer HJ, Huijing PA. Effects of inter- and extramuscular myofascial force transmission on adjacent synergistic muscles: Assessment by experiments and finite-element modeling. *J Biomech* 2003; 36:1797–1811.
72. Inouye J, Handsfield G, Blemker S. Fiber Tractography for Finite-Element Modeling of Transversely Isotropic Biological Tissues of Arbitrary Shape Using Computational Fluid Dynamics. *Simul Ser* 2015; 47:184–189.
73. Handsfield GG, Bolsterlee B, Inouye JM, Herbert RD, Besier TF, *et al.* Determining skeletal muscle architecture with Laplacian simulations: a comparison with diffusion tensor imaging. *Biomech Model Mechanobiol* 2017; 16:1845–1855.
74. Moo EK, Fortuna R, Sibole SC, Abusara Z, Herzog W. In vivo sarcomere lengths and sarcomere elongations are not uniform across an intact muscle. *Front Physiol* 2016; 7:1–9.
75. Willems MET, Huijing PA. Heterogeneity of mean sarcomere length in different fibres: effects on length range of active force production in rat muscle. *Eur J Appl Physiol Occup Physiol* 1994; 68:489–496.

76. Dziki J, Badylak S, Yabroudi M, Sicari B, Ambrosio F, *et al.* An acellular biologic scaffold treatment for volumetric muscle loss: results of a 13-patient cohort study. *npj Regen Med* 2016; 1:16008.
77. Sicari BM, Rubin JP, Dearth CL, Wolf MT, Ambrosio F, *et al.* An Acellular Biologic Scaffold Promotes Skeletal Muscle Formation in Mice and Humans with Volumetric Muscle Loss. *Sci Transl Med* 2014; 6. doi:10.1126/scitranslmed.3008085.
78. Goldman SM, Henderson BEP, Walters TJ, Corona BT. Co-delivery of a laminin-111 supplemented hyaluronic acid based hydrogel with minced muscle graft in the treatment of volumetric muscle loss injury. *PLoS One* 2018; 13:1–15.
79. Grasman JM, Do DM, Page RL, Pins GD. Rapid release of growth factors regenerates force output in volumetric muscle loss injuries. *Biomaterials* 2015; 72:49–60.
80. Sadtler K, Powell JD, Wolf MT, Elisseeff JH, Estrellas K, *et al.* Developing a pro-regenerative biomaterial scaffold microenvironment requires T helper 2 cells. *Science (80-)* 2016; 352:366–370.
81. Palumbo-Zerr K, Zerr P, Distler A, Fliehr J, Mancuso R, *et al.* Orphan nuclear receptor NR4A1 regulates transforming growth factor- β 2 signaling and fibrosis. *Nat Med* 2015; 21:150–158.
82. Garg K, Corona BT, Walters TJ. Losartan administration reduces fibrosis but hinders functional recovery after volumetric muscle loss injury. *J Appl Physiol* 2014; 117:1120–1131.
83. Hussey GS, Dziki JL, Lee YC, Bartolacci JG, Behun M, *et al.* Matrix bound nanovesicle-associated IL-33 activates a pro-remodeling macrophage phenotype via a non-canonical,

- ST2-independent pathway. *J Immunol Regen Med* 2019; 3:26–35.
84. Dziki JL, Sicari BM, Wolf MT, Cramer MC, Badylak SF. Immunomodulation and Mobilization of Progenitor Cells by Extracellular Matrix Bioscaffolds for Volumetric Muscle Loss Treatment. *Tissue Eng - Part A* 2016; 22:1129–1139.
 85. Walpole J, Mac Gabhann F, Peirce SM, Chappell JC. Agent-based computational model of retinal angiogenesis simulates microvascular network morphology as a function of pericyte coverage. *Microcirculation* 2017; 24:1–14.
 86. Thorne BC, Bailey AM, Peirce SM. Combining experiments with multi-cell agent-based modeling to study biological tissue patterning. *Brief Bioinform* 2007; 8:245–257.
 87. Renardy M, Wessler T, Blemker S, Linderman J, Peirce S, *et al.* Data-Driven Model Validation Across Dimensions. *Bull Math Biol* 2019; 81:1853–1866.
 88. Corona BT, Henderson BEP, Ward CL, Greising SM. Contribution of minced muscle graft progenitor cells to muscle fiber formation after volumetric muscle loss injury in wild-type and immune deficient mice. *Physiol Rep* 2017; 5:1–11.
 89. Ward CL, Ji L, Corona BT. An Autologous Muscle Tissue Expansion Approach for the Treatment of Volumetric Muscle Loss. *Biores Open Access* 2015; 4:198–208.
 90. Murphy MM, Lawson JA, Mathew SJ, Hutcheson DA, Kardon G. Satellite cells, connective tissue fibroblasts and their interactions are crucial for muscle regeneration. *Development* 2011; 138:3625–3637.
 91. Mathew SJ, Hansen JM, Merrell AJ, Murphy MM, Lawson JA, *et al.* Connective tissue fibroblasts and Tcf4 regulate myogenesis. *Development* 2011; 138:371–384.
 92. Chapman MA, Meza R, Lieber RL. Skeletal muscle fibroblasts in health and disease.

- Differentiation* 2016; 92:108–115.
93. Cornwell KG, Downing BR, Pins GD. Characterizing fibroblast migration on discrete collagen threads for applications in tissue regeneration. *J Biomed Mater Res - Part A* 2004; 71:55–62.
 94. Lemos DR, Babaeijandaghi F, Low M, Chang CK, Lee ST, *et al.* Nilotinib reduces muscle fibrosis in chronic muscle injury by promoting TNF-mediated apoptosis of fibro/adipogenic progenitors. *Nat Med* 2015; 21:786–794.
 95. Agley CC, Rowleron AM, Velloso CP, Lazarus NR, Harridge SDR. Human skeletal muscle fibroblasts, but not myogenic cells, readily undergo adipogenic differentiation. *J Cell Sci* 2013; 126:5610–5625.
 96. Balestrini JL, Billiar KL. Magnitude and Duration of Stretch Modulate Fibroblast Remodeling. *J Biomech Eng* 2009; 131:051005.
 97. McKay TB, Hjortdal J, Priyadarsini S, Karamichos D. Acute hypoxia influences collagen and matrix metalloproteinase expression by human keratoconus cells in vitro. *PLoS One* 2017; 12:1–13.
 98. Steinbrech DS, Longaker MT, Mehrara BJ, Saadeh PB, Chin GS, *et al.* Fibroblast response to hypoxia: The relationship between angiogenesis and matrix regulation. *J Surg Res* 1999; 84:127–133.
 99. Modarressi A, Pietramaggiori G, Godbout C, Vigato E, Pittet B, *et al.* Hypoxia impairs skin myofibroblast differentiation and function. *J Invest Dermatol* 2010; 130:2818–2827.
 100. Corona BT, Rivera JC, Greising SM. Inflammatory and Physiological Consequences of Debridement of Fibrous Tissue after Volumetric Muscle Loss Injury. *Clin Transl Sci* 2018;

- 11:208–217.
101. Liu W, Wei-LaPierre L, Klose A, Dirksen RT, Chakkalakal J V. Inducible depletion of adult skeletal muscle stem cells impairs the regeneration of neuromuscular junctions. *Elife* 2015; 4:1–20.
 102. Urciuolo A, Urbani L, Perin S, Maghsoudlou P, Scottoni F, *et al.* Decellularised skeletal muscles allow functional muscle regeneration by promoting host cell migration. *Sci Rep* 2018; 8:1–20.
 103. Schultz E, Jaryszak DL, Valliere CR. Response of satellite cells to focal skeletal muscle injury. *Muscle Nerve* 1985; 8:217–222.
 104. Grzelkowska-Kowalczyk K. The Importance of Extracellular Matrix in Skeletal Muscle Development and Function. *InTechOpen* 2016.
 105. Gilbert PM, Havenstrite KL, Magnusson KEG, Sacco A, Leonardi † N A, *et al.* Substrate Elasticity Regulates Skeletal Muscle Stem Cell Self-Renewal in Culture. *Science (80-)* 2005; 139:1078–1081.
 106. Boonen KJM, Rosaria-Chak KY, Baaijens FPT, van der Schaft DWJ, Post MJ. Essential environmental cues from the satellite cell niche: optimizing proliferation and differentiation. *Am J Physiol Physiol* 2009; 296:C1338–C1345.
 107. Stern MM, Myers RL, Hammam N, Stern KA, Eberli D, *et al.* The influence of extracellular matrix derived from skeletal muscle tissue on the proliferation and differentiation of myogenic progenitor cells ex vivo. *Biomaterials* 2009; 30:2393–2399.
 108. Engler AJ, Griffin MA, Sen S, Bönnemann CG, Sweeney HL, *et al.* Myotubes differentiate optimally on substrates with tissue-like stiffness: Pathological implications for soft or stiff

- microenvironments. *J Cell Biol* 2004; 166:877–887.
109. Menetrey J, Kasemkijwattana C, Day CS, Bosch P, Vogt M, *et al.* Growth factors improve muscle healing in vivo. *J Bone Jt Surg* 2000; 82:131–137.
 110. Villalta SA, Rinaldi C, Deng B, Liu G, Fedor B, *et al.* Interleukin-10 reduces the pathology of mdx muscular dystrophy by deactivating M1 macrophages and modulating macrophage phenotype. *Hum Mol Genet* 2011; 20:790–805.
 111. Fu X, Xiao J, Wei Y, Li S, Liu Y, *et al.* Combination of inflammation-related cytokines promotes long-term muscle stem cell expansion. *Cell Res* 2015; 25:655–673.
 112. Arnold L, Adeline H, Poron F, Baba-Amer Y, Rooijen N van, *et al.* Inflammatory monocytes recruited after skeletal muscle injury switch into antiinflammatory macrophages to support myogenesis. *J Exp Med* 2007; 204:1057–1069.
 113. Deng B, Wehling-Henricks M, Villalta SA, Wang Y, Tidball JG. IL-10 Triggers Changes in Macrophage Phenotype That Promote Muscle Growth and Regeneration. *J Immunol* 2012; 189:3669–3680.
 114. Flamini V, Ghadiali RS, Antczak P, Rothwell A, Turnbull JE, *et al.* The Satellite Cell Niche Regulates the Balance between Myoblast Differentiation and Self-Renewal via p53. *Stem Cell Reports* 2018; 10:970–983.
 115. Bentzinger CF, Wang YX, Rudnicki MA, Bentzinger CF, Wang YX, *et al.* Building Muscle : Molecular Regulation of Myogenesis. *Cold Spring Harb Perspect Biol* 2012; :1–16.
 116. Cencetti F, Bernacchioni C, Tonelli F, Roberts E, Donati C, *et al.* TGF β 1 evokes myoblast apoptotic response via a novel signaling pathway involving S1P4 transactivation upstream of Rho-kinase-2 activation. *FASEB J* 2013; 27:4532–4546.

117. Rossi M, Bernasconi P, Baggi F, Waal Malefyt R, Mantegazza R. Cytokines and chemokine are both expressed by human myoblasts: possible relevance for the immune pathogenesis of muscle inflammation. *Int Immunol* 2000; 12:1329–1335.
118. Lewis M, Tippet H, Sinanan A, Morgan M, Hunt N. Gelatinase-B (Matrix Metalloproteinase-9; MMP-9) secretion is involved in the migratory phase of human and murine muscle cell cultures. *J Muscle Res Cell Motil* 2000; 21:223–2333.
119. Zapf J, Hauri C, Waldvogel M, Froesch ER. Acute metabolic effects and half-lives of intravenously administered insulinlike growth factors I and II in normal and hypophysectomized rats. *J Clin Invest* 1986; 77:1768–1775.
120. He Y, Li Y, Wei Z, Zhang X, Gao J, *et al.* Pharmacokinetics, tissue distribution, and excretion of FGF-21 following subcutaneous administration in rats. *Drug Test Anal* 2018; 10:1061–1069.
121. Zioncheck TF, Richardson L, Deguzman GG, Modi NB, Hansen SE, *et al.* The pharmacokinetics, tissue localization, and metabolic processing of recombinant human hepatocyte growth factor after intravenous administration in rats. *Endocrinology* 1994; 134:1879–1887.
122. Rachmawati H, Beljaars L, Reker-Smit C, Van Loenen-Weemaes AMM, Hagens WI, *et al.* Pharmacokinetic and biodistribution profile of recombinant human interleukin-10 following intravenous administration in rats with extensive liver fibrosis. *Pharm Res* 2004; 21:2072–2078.
123. Guo Q, Minnier J, Burchard J, Chiotti K, Spellman P, *et al.* Physiologically activated mammary fibroblasts promote postpartum mammary cancer. *JCI Insight* 2017; 2.

124. Singh VP, Mathison M, Patel V, Sanagasetti D, Gibson BW, *et al.* MiR-590 Promotes Transdifferentiation of Porcine and Human Fibroblasts Toward a Cardiomyocyte-Like Fate by Directly Repressing Specificity Protein 1. *J Am Heart Assoc* 2016; 5.
125. Miskulin M, Dagleish R, Kluge-Beckerman B, Rennard SI, Tolstoshev P, *et al.* Human type III collagen gene expression is coordinately modulated with the type I collagen genes during fibroblast growth. *Biochemistry* 1986; 25:1408–1413.
126. Chamberlain JS. ACE inhibitor bulks up muscle. *Nat Med* 2007; 13:125–126.
127. Saucerman JJ, Brunton LL, Michailova AP, McCulloch AD. Modeling β -Adrenergic Control of Cardiac Myocyte Contractility in Silico. *J Biol Chem* 2003; 278:47997–48003.
128. Rikard S, Athey T, Nelson A, Christiansen S, Lee J, *et al.* Multiscale Coupling of an Agent-based Model of Tissue Fibrosis and a Logic-based Model of Intracellular Signaling. *Front Physiol* 2019; 17.
129. Westman AM, Dyer SE, Remer JD, Hu X, Christ GJ, *et al.* A coupled framework of in situ and in silico analysis reveals the role of lateral force transmission in force production in volumetric muscle loss injuries. *J Biomech* 2019; 85.
130. Lee JJ, Talman L, Peirce SM, Holmes JW. Spatial scaling in multiscale models: methods for coupling agent-based and finite-element models of wound healing. *Biomech Model Mechanobiol* 2019; 18:1297–1309.
131. Badylak SF, Dziki JL, Sicari BM, Ambrosio F, Boninger ML. Mechanisms by which acellular biologic scaffolds promote functional skeletal muscle restoration. *Biomaterials* 2016; 103:128–136.
132. Walker D, Sun T, MacNeil S, Smallwood R. Modeling the effect of exogenous calcium on

- keratinocyte and HaCat cell proliferation and differentiation using an agent-based computational paradigm. *Tissue Eng* 2006; 12:2301–2309.
133. Peirce SM, Van Gieson EJ, Skalak TC. Multicellular simulation predicts microvascular patterning and in silico tissue assembly. *FASEB J* 2004; 18:731–733.
 134. Kudo S, Mizuno K, Hirai Y, Shimizu T. Clearance and Tissue Distribution of Recombinant Human Interleukin I β in Rats. *Cancer Res* 1990; 50:5751–5755.
 135. Le Grand F, Rudnicki MA. Skeletal muscle satellite cells and adult myogenesis. *Curr Opin Cell Biol* 2007; 19:628–633.
 136. Schultz E, Jaryszak DL, Gibson MC, Albright DJ. Absence of exogenous satellite cell contribution to regeneration of frozen skeletal muscle. *J Muscle Res Cell Motil* 1986; 7:361–367.
 137. Machingal MA, Corona BT, Walters TJ, Kesireddy V, Koval CN, *et al.* A Tissue-Engineered Muscle Repair Construct for Functional Restoration of an Irrecoverable Muscle Injury in a Murine Model. *Tissue Eng Part A* 2011; 17:2291–2303.
 138. Serafín A, Roselló-Catafau J, Prats N, Gelpí E, Rodés J, *et al.* Ischemic preconditioning affects interleukin release in fatty livers of rats undergoing ischemia/reperfusion. *Hepatology* 2004; 39:688–698.
 139. Furukawa Y, Becker G, Stinn JL, Shimizu K, Libby P, *et al.* Interleukin-10 (IL-10) augments allograft arterial disease: Paradoxical effects of IL-10 in vivo. *Am J Pathol* 1999; 155:1929–1939.
 140. Contreras O, Rebolledo DL, Oyarzún JE, Olguín HC, Brandan E. Connective tissue cells expressing fibro/adipogenic progenitor markers increase under chronic damage:

- relevance in fibroblast-myofibroblast differentiation and skeletal muscle fibrosis. *Cell Tissue Res* 2016; 364:647–660.
141. Uezumi A, Ito T, Morikawa D, Shimizu N, Yoneda T, *et al.* Fibrosis and adipogenesis originate from a common mesenchymal progenitor in skeletal muscle. *J Cell Sci* 2011; 124:3654–3664.
142. Yin J, Huang Y, Gao G, Nong L, Xu N, *et al.* Changes and significance of inflammatory cytokines in a rat model of cervical spondylosis. *Exp Ther Med* 2018; 15:400–406.
143. Engles RE, Huber TS, Zander DS, Hess PJ, Welborn MB, *et al.* Exogenous Human Recombinant Interleukin-10 Attenuates Hindlimb Ischemia–Reperfusion Injury. *J Surg Res* 2002; 69:425–428.
144. Plunkett JA, Yu CG, Easton JM, Bethea JR, Yeziarski RP. Effects of interleukin-10 (IL-10) on pain behavior and gene expression following excitotoxic spinal cord injury in the rat. *Exp Neurol* 2001; 168:144–154.
145. Köken T, Serteser M, Kahraman A, Akbulut G, Nuri Dilek O. Which is more effective in the prevention of renal ischemia-reperfusion- induced oxidative injury in the early period in mice: Interleukin (IL)-10 or anti-IL-12? *Clin Biochem* 2004; 37:50–55.
146. Dinant S, Veteläinen RL, Florquin S, van Vliet AK, van Gulik TM. IL-10 Attenuates Hepatic I/R Injury and Promotes Hepatocyte Proliferation. *J Surg Res* 2007; 141:176–182.
147. Spera PA, Ellison JA, Feuerstein GZ, Barone FC. IL-10 reduces rat brain injury following focal stroke. *Neurosci Lett* 1998; 251:189–192.
148. Van Deventer SJH, Elson CO, Fedorak RN. Multiple doses of intravenous interleukin 10 in steroid-refractory Crohn’s disease. *Gastroenterology* 1997; 113:383–389.

149. Corona BT, Rivera JC, Dalske KA, Wenke JC, Greising SM. Pharmacological Mitigation of Fibrosis in a Porcine Model of Volumetric Muscle Loss Injury. *Tissue Eng Part A* 2020; 00:1–11.